

**A Comparative Turbomachinery Flow Study with the
Conservative and Nonconservative Forms of the
Space–Time Variational Multiscale Method in the
Inertial and Non-inertial Reference Frames**

by

Levent AYDINBAKAR

Doctor of Engineering

Waseda University

March 2021

**A Comparative Turbomachinery Flow Study with the
Conservative and Nonconservative Forms of the
Space–Time Variational Multiscale Method in the
Inertial and Non-inertial Reference Frames**

by

Levent AYDINBAKAR

Doctor of Engineering

Waseda University

Graduate School of Creative Science and Engineering

Department of Modern Mechanical Engineering

Research on Applied Mechanics of Fluid–Structure Interaction

APPROVED, THESIS COMMITTEE:

Kenji Takizawa, Chair
Professor of Modern Mechanical Engineering

Jin Kusaka
Professor of Modern Mechanical Engineering

Yu Matsuda
Associate Professor of Modern Mechanical
Engineering

March 2021

Acknowledgments

I would like to acknowledge my indebtedness and thanks to Professor Kenji Takizawa for giving me advice and support. I always feel lucky studying on my research under the supervision of Professor Takizawa. I have learned from him many things, most importantly not giving up on anything. I respect his professional attitude to research.

I would like to thank my committee members, Professor Jin Kusaka and Associate Professor Yu Matsuda, and Professor Takashi Maekawa for their exceptionally helpful comments.

I am deeply grateful to Professor Tayfun E. Tezduyar for giving me advice on my research. This dissertation and two papers would not have been possible without Professor Takizawa and Professor Tezduyar's guidance and persistent help. The things I learned from them on how to do a research will always light my way in the professional life.

I would like to express my sincere gratitude all members of the Takizawa Laboratory and T★AFSM, especially, Dr. Yuto Otoguro, Dr. Takuya Terahara, Dr. Takashi Kuraishi, Dr. Takafumi Sasaki, Dr. Taro Kanai, Mr. Reha Avsar, Mr. Yang Liu, Mr. Daisaku Matsuda and Mr. Zhaojing Xu.

This work was supported in part by the YLSY scholarship program funded by the Republic of Turkey. I would like to give a special thanks to my father and uncles. They supported me to get this scholarship. I am grateful for their patience and reliance.

I really appreciate my parents, sisters and brother for their patience and spending plenty of time on taking care of my son during my research. They all and my close friends, with their warm attitude, have enabled me to continue studying hard anytime I feel alone when I was doing my research in Japan.

I especially want to thank my dearest wife, Dr. Aysenur Aydinbakar for supporting me patiently without any hesitation. I dedicate this dissertation to my little son, Ozgur Aydinbakar, whom I have missed too much.


Contents

List of Illustrations	iv
List of Tables	xiii
1 Introduction	1
1.1 Background	1
1.2 CFD for turbomachinery flows	2
1.3 ST methods	3
1.3.1 ST-IGA	3
1.3.2 ST-SI method	5
1.3.3 ST-VMS method	6
1.4 Rotation representation	9
1.5 Motivation	9
1.6 Dissertation overview	10
2 Governing Equations	13
2.1 Navier–Stokes equations	13
2.2 IRF and NRF	14
2.2.1 Velocity calculation in the NRF	14
2.2.2 Multiple reference frames	15
2.3 Navier–Stokes equations in the NRF	16
3 ST Formulations	18
3.1 ST variational formulations	18
3.2 ST-VMS formulation	19
3.3 ST-SI formulation	23
3.4 Exact representation of geometry and prescribed-velocity	26
3.4.1 Geometry representation	26

3.4.2	Rotation-generated prescribed velocity	28
4	ST Formulations in the NRF	29
4.1	ST variational formulations in the NRF	29
4.2	ST-VMS formulation in the NRF	30
4.3	Global conservation of mass and momentum	34
4.3.1	Global conservation of mass	36
4.3.2	Global conservation of linear momentum	37
4.3.3	Global conservation of angular momentum	41
5	U-duct Turbulent-Flow Analysis	46
5.1	Definitions for the data analysis	46
5.1.1	Scale separation	46
5.1.2	Nondimensionalization	47
5.1.3	Wall-related scaling	48
5.2	Straight duct with periodicity condition	48
5.2.1	Problem setup	48
5.2.2	Mesh	48
5.2.3	Boundary conditions	50
5.2.4	Computational conditions	50
5.2.5	Results	50
5.3	U-duct	52
5.3.1	Problem setup	52
5.3.2	Boundary conditions	52
5.3.3	Mesh	52
5.3.4	Computational conditions	56
5.3.5	Results	56
6	Taylor–Couette Flow Analysis	66
6.1	Problem setup	67
6.2	Meshes	69
6.3	Boundary conditions and mesh motions	71

6.4	Computational conditions	71
6.5	Results	72
6.5.1	Flow development: Case 1	73
6.5.2	Flow development: Case 4	74
6.5.3	Rotational periodicity: Case 1	74
6.5.4	Mesh refinement: Case 1	80
6.5.5	Flow patterns: Cases 2 and 3	80
6.5.6	Methods: Case 1	87
7	Computations in an Engineering Application	94
7.1	Problem setup	95
7.2	Mesh generation	96
7.3	Computational conditions	97
7.4	Flow development	97
7.5	Pump performance	99
7.6	Flow around impeller in the NRF	104
7.7	Results	105
8	Concluding Remarks	108
A	Stabilization Parameters and Element Lengths	111
A.1	Stabilization parameters	111
A.2	Element lengths	113
B	Path Representation	114
B.1	A circular-arc path	114
B.2	Prescribed velocity in the ST domain	117
	Bibliography	119

Illustrations

1.1	Exact representation of a cylinder. From <i>left</i> to <i>right</i> , the CAD geometry, the control mesh, and the physical mesh of four elements constructed by NURBS. The <i>red</i> points are the control points	4
1.2	An example mesh refinement. NURBS (<i>left</i>) and FE (<i>right</i>)	5
1.3	An SI (the <i>black</i> line) between two rotating (<i>red</i> and <i>blue</i>) flow domains	6
1.4	An infinite channel (<i>top</i>) and a cylindrical computational domain (<i>bottom</i>) represented by a translational-periodicity and a rotational-periodicity. The <i>red</i> lines represent the boundaries where the periodicity is enforced by the ST-SI. The <i>blue</i> arrows denote the translation of the SIs	6
2.1	Velocity conversion between the IRF and NRF. Arrows represent the vectorial quantities. The <i>red</i> point is the location where a measurement is made. The symbol  , represents the position where the reference frame is located	14
3.1	Diagram of an ST slab (figure is from [9])	18
3.2	A circular-arc represented exactly by a quadratic NURBS element. This figure was also shown in [2]	27
3.3	A circular arc with $q = \frac{\pi}{2}$ represented exactly by two quadratic NURBS elements. This figure was also shown in [2]	28

5.1	Straight duct geometry. The <i>red</i> planes show the boundaries where the periodicity condition is enforced. \mathbf{e}_s , \mathbf{e}_1 and \mathbf{e}_2 are the coordinate basis vectors in the streamwise and wall-normal directions. This figure was also shown in [1]	49
5.2	The control mesh (<i>left</i>) and the corresponding mesh (<i>middle</i>) with a close view of it (<i>right</i>). The control points are shown by the <i>yellow</i> points. This figure was also shown in [1]	49
5.3	\overline{u}_s and $\ u'_s\ _{2,Q}$ at $\text{Re} = 10^5$. Velocity profiles are calculated in the straight duct with $Q = \left\{ \mathbf{x} = (0, x_2, x_s) \mid x_s \in (0, 5D), t \in (8.5T, 20T) \right\}$. The reference study is [82]. This figure was also shown in [1]	51
5.4	\overline{u}^+ at $\text{Re} = 4 \times 10^4$ and $\text{Re} = 10^5$. Velocity profiles are calculated in the straight duct with $Q = \left\{ \mathbf{x} = (0, x_2, x_s) \mid x_s \in (0, 5D), t \in (8.5T, 20T) \right\}$. The reference study is [84] at $\text{Re} = 4 \times 10^4$. This figure was also shown in [1]	52
5.5	U-duct geometry. The <i>red</i> and <i>blue</i> planes show the inlet and outlet. \mathbf{e}_s , \mathbf{e}_1 and \mathbf{e}_2 are the coordinate basis vectors in the streamwise and wall-normal directions. This figure was also shown in [1]	53
5.6	The locations where the flow characteristics are reported. The <i>red</i> plane is the near-wall ($x_1/D = 0.375$) and the <i>blue</i> plane is the center ($x_1 = 0$) planes. The flow field is generated and investigated along the model on the <i>red</i> and <i>blue</i> lines. This figure was also shown in [1]	53
5.7	Exact arc representation by NURBS. The weight values of $\cos(\pi/4)$ and 1 are set on the <i>blue</i> and the <i>red</i> points. This figure was also shown in [1]	54
5.8	Mesh A, B, C, D and E on the U-duct. This figure was also shown in [1]	55

5.9	Flow development with the velocity magnitude ($\ \bar{\mathbf{u}}\ $) and pressure (\bar{p}) distributions along the U-duct on the center plane. The time-average is taken over $\mathcal{T} = (0, 10T)$, $(10T, 20T)$, $(20T, 30T)$, and $(30T, 40T)$ from <i>top</i> to <i>bottom</i> . This figure was also shown in [1] . . .	57
5.10	Effect of the flow development by Fourier transform of u_2 at the point shown in <i>blue</i> on the center plane. The time intervals that the transformation is performed are given in the legend. This figure was also shown in [1]	58
5.11	Effect of the averaging range by Fourier transform of u_2 at the point shown in <i>blue</i> on the center plane. The time intervals that the transformation is performed are given in the legend. The lowest frequency of local maximum is emphasized by the <i>cyan</i> line at $0.67T$. This figure was also shown in [1]	58
5.12	Effect of the mesh refinement by Fourier transform of u_2 at the point shown in <i>blue</i> on the center plane. The time range is $\mathcal{T} = (33T, 36T)$. This figure was also shown in [1]	59
5.13	Effect of the mesh refinement on the streamwise velocity along the U-duct. \bar{u}_s is calculated on the center plane. Time-average is taken over $\mathcal{T} = (33T, 36T)$. The reference results are adapted from [82]. Numerical results are adapted from [1]	60
5.14	Effect of the Courant number by the isosurfaces corresponding to a positive value of the second invariant of $\nabla\bar{\mathbf{u}}$. Isosurfaces are colored by velocity magnitude ($\ \bar{\mathbf{u}}\ $). Time-average is taken over $\mathcal{T} = (33T, 36T)$. Results obtained using Mesh D and E are given on the <i>left</i> and <i>right</i> . $C_{\Delta t} = 10, 5$ and 2.5 from <i>top</i> to <i>bottom</i> . The intersection between the isosurfaces and the center plane is represented by the lines in <i>yellow</i> . This figure was also shown in [1] .	61

5.15	Effect of the Courant number on the streamwise velocity along the U-duct. Results are obtained using Mesh D and E. \bar{u}_s is calculated on the center plane. Time-average is taken over $\mathcal{T} = (33T, 36T)$. The reference results are adapted from [82]. Numerical results are adapted from [1]	62
5.16	Effect of the Courant number on the streamwise velocity along the U-duct. Results are obtained using Mesh D and E. \bar{u}_s is calculated on the near-wall plane. Time-average is taken over $\mathcal{T} = (33T, 36T)$. The reference results are adapted from [82]. Numerical results are adapted from [1]	63
5.17	Effect of the Courant number on the root-mean-square fluctuating velocity along the U-duct. Results are obtained using Mesh D and E. $\ u'_s\ _{2,\mathcal{T}}$ is calculated on the center plane. Time-average is taken over $\mathcal{T} = (33T, 36T)$. The reference results are adapted from [82]. Numerical results are adapted from [1]	64
5.18	Effect of the Courant number on the root-mean-square fluctuating velocity along the U-duct. Results are obtained using Mesh D and E. $\ u'_s\ _{2,\mathcal{T}}$ is calculated on the near-wall plane. Time-average is taken over $\mathcal{T} = (33T, 36T)$. The reference results are adapted from [82]. Numerical results are adapted from [1]	65
6.1	Computational domain. The local orthonormal basis set \mathbf{e}_r , \mathbf{e}_θ and \mathbf{e}_z is used in the cylindrical coordinate system	67
6.2	Taylor–Couette flow patterns. The Couette, Taylor vortex and wavy vortex flow are shown in <i>blue</i> , <i>red</i> and <i>gray</i> regions. The cases calculated in this study are marked by the <i>red</i> points. The inner cylinder rotation is given in the counter-clockwise direction and the negative Reynolds number means that the outer cylinder rotation in the clockwise direction. The figure has been adapted from [86] and also shown in [2]	68

6.3	The circular geometry representation with quadratic NURBS patches that have quarter, one-third and half-domain sizes (<i>left to right</i>). This figure was also shown in [2]	69
6.4	The coarse control meshes for the quarter, one-third, half-domain sizes and the full domain (<i>left to right, top to bottom</i>). The control points are shown by <i>red</i> circles	70
6.5	The medium and fine control meshes for the patch that has half-domain size. The control points are shown by <i>red</i> circles. This figure was also shown in [2]	71
6.6	Flow visualization configurations in a volume (<i>left</i>) and section (<i>right</i>). $\frac{1}{4}$ of the flow field is subtracted in a volume visualization and the results are shown in the remaining <i>gray</i> part. The <i>red</i> and <i>green</i> sections are placed at the center along the radial and axial directions for a section visualization. This figure was also shown in [2]	73
6.7	Flow development in Case 1. Isosurfaces of $u_z / (U_i - \eta U_o)$ in the IRF (<i>left</i>) and NRF (<i>right</i>), with the full-domain representation of the flow field using the coarse mesh, at $t = 10T, 30T, 50T$ and $70T$ (from <i>top</i> to <i>bottom</i>). 16 isosurfaces are used in $-0.15 \leq u_z / (U_i - \eta U_o) \leq 0.15$. This figure was also shown in [2]	75
6.8	Flow development in Case 1 by the f -based Fourier decomposition of $u_\theta / (U_i - \eta U_o)$ at $r = \frac{r_o + r_i}{2}$, $\theta = 0$. The different time ranges, all spanning $10T$, are given in the legend. The amplitude of the Fourier coefficients is averaged in space along the axial direction at 56 equally-spaced points. This figure was also shown in [2]	76
6.9	$\ \mathbf{u}\ / (U_i - \eta U_o)$ at $t = 9T$ for Case 4. This figure was also shown in [2]	77
6.10	Flow development by $(\omega_i - \bar{\omega}) / (\omega_i - \omega_o)$ in Case 4. Velocity is averaged in space in both axial and circumferential directions. This figure was also shown in [2]	77

6.11	Isosurfaces of $u_z / (U_i - \eta U_o)$ in Case 1 in the IRF (<i>left</i>) and NRF (<i>right</i>), with the quarter, one-third, half-domain and full-domain representations of the flow field (from <i>top</i> to <i>bottom</i>), after the solutions become periodic. 16 isosurfaces are used in $-0.15 \leq u_z / (U_i - \eta U_o) \leq 0.15$. This figure was also shown in [2]	78
6.12	λ -based Fourier decomposition of $u_\theta / (U_i - \eta U_o)$ at $t = 80T$, $r = \frac{r_o + r_i}{2}$ in Case 1, with the quarter, one-third, half-domain and full-domain representations of the flow field The amplitude of the Fourier coefficients is averaged in space along the axial direction at 56 equally-spaced points. This figure was also shown in [2]	79
6.13	Mesh refinement in Case 1. Isosurfaces of $u_z / (U_i - \eta U_o)$ in the IRF (<i>left</i>) and NRF (<i>right</i>), with the half-domain representation of the flow field, using the coarse, medium and fine meshes (from <i>top</i> to <i>bottom</i>). 16 isosurfaces are used in $-0.15 \leq u_z / (U_i - \eta U_o) \leq 0.15$. This figure was also shown in [2]	81
6.14	Mesh refinement in Case 1. $\ \mathbf{u}\ / (U_i - \eta U_o)$ in the IRF (<i>left</i>) and NRF (<i>right</i>), with the half-domain representation of the flow field, using the coarse, medium and fine meshes (from <i>top</i> to <i>bottom</i>). This figure was also shown in [2]	82
6.15	The ST-averaged angular velocity, $(\omega_i - \bar{\omega}) / (\omega_i - \omega_o)$ in Case 1 over the range $\mathcal{T} = (97T, 100T)$. The velocity is averaged in space along both axial and circumferential directions This figure was also shown in [2]	83
6.16	Flow development in Case 2. Isosurfaces of $u_z / (U_i - \eta U_o)$ in the IRF (<i>left</i>) and NRF (<i>right</i>), with the half-domain representation of the flow field, using the medium mesh, at $t = 5T, 10T, 15T$ and $20T$ (from <i>top</i> to <i>bottom</i>). 16 isosurfaces are used in $-0.15 \leq u_z / (U_i - \eta U_o) \leq 0.15$. This figure was also shown in [2]	84

6.17	Flow development in Case 2. $\ \mathbf{u}\ / (U_i - \eta U_o)$ in the IRF (<i>left</i>) and NRF (<i>right</i>), with the half-domain representation of the flow field, using the medium mesh, at $t = 5T, 10T, 15T$ and $20T$ (from <i>top</i> to <i>bottom</i>). This figure was also shown in [2]	85
6.18	The ST-averaged angular velocity, $(\omega_i - \bar{\omega}) / (\omega_i - \omega_o)$ in Case 2 over the range $\mathcal{T} = (15T, 20T)$. The velocity is averaged in space along both axial and circumferential directions This figure was also shown in [2]	86
6.19	Case 3. Isosurfaces of $u_z / (U_i - \eta U_o)$ in the IRF (<i>left</i>) and NRF (<i>right</i>), with the half-domain representation of the flow field, using the medium mesh, at $t = 15T$. 16 isosurfaces are used in $-0.15 \leq u_z / (U_i - \eta U_o) \leq 0.15$. This figure was also shown in [2] . . .	86
6.20	The ST-averaged angular velocity, $(\omega_i - \bar{\omega}) / (\omega_i - \omega_o)$ in Case 3 over the range $\mathcal{T} = (10T, 15T)$. The velocity is averaged in space along both axial and circumferential directions This figure was also shown in [2]	87
6.21	The ST-averaged angular velocity, $(\omega_i - \bar{\omega}) / (\omega_i - \omega_o)$ in Case 1 over the range $\mathcal{T} = (105T, 110T)$. The velocity is averaged in space along both axial and circumferential directions. The solution computed using the fine mesh is also shown as a reference, using the strong enforcement of the prescribed velocities, with the conservative version of the ST-VMS, in the IRF. This figure was also shown in [2]	88
6.22	Global angular momentum balance in Case 1, in the IRF. The <i>blue</i> circles show a closer view for each case. Figure is adapted from [2] . .	91
6.23	Global angular momentum balance in Case 1, in the NRF. The <i>blue</i> circles show a closer view for each case. Figure is adapted from [2] . .	92
6.24	Global angular momentum balance in Case 1, in the IRF and NRF for the solution achieved using the fine mesh. The prescribed velocities are enforced strongly and conservative version of the ST-VMS is used. The <i>blue</i> circles show a closer view for each case. Figure is adapted from [2]	93

7.1	Boundary conditions. SIs are represented by <i>blue</i> and <i>red</i> , inlet is <i>green</i> , outlet is <i>gray</i> . Impeller parts are shown by <i>yellow</i> . The <i>grass green</i> and <i>black</i> are the surfaces, where pump efficiency is measured between	95
7.2	Parts of the mesh. The patching strategy. Please note that a part of the suction casing is not given because it is a confidential information. The mesh and parametrization in that part is also similar to the other parts which are given clearly	96
7.3	The point location used for <i>f</i> -based Fourier decomposition	97
7.4	Flow development. <i>f</i> -based Fourier decomposition of $p/(\rho U^2)$	98
7.5	Pump efficiency (<i>blue</i>) and hydraulic head (<i>red</i>), scaled with the experimental values, with seven different volumetric flow rates. Time average is taken in $\mathcal{T} = (8T, 9T)$	100
7.6	Shaft power, scaled with the experimental value, at $Q = Q_0$, by various volumetric flow rates in $(8T, 9T)$	101
7.7	Time-averaged absolute pressure, $\bar{p}/(\rho U^2)$, on the symmetry plane. Computations with different discharge values of $Q = 0.4 Q, 0.6 Q, 0.8 Q, 1.0 Q, 1.2 Q$ and $1.4 Q$ are displayed from <i>left</i> to <i>right</i> and <i>top</i> to <i>bottom</i> . Results are averaged in $\mathcal{T} = (8T, 9T)$	102
7.8	Time-averaged flow field around impeller by streamlines colored by velocity magnitude, $\ \bar{\mathbf{u}}_R\ /U$. Streamlines and velocity magnitude are calculated relative to the impeller. Computations with different discharge values of $Q = 0.4 Q, 0.6 Q, 0.8 Q, 1.0 Q, 1.2 Q$ and $1.4 Q$ are displayed from <i>left</i> to <i>right</i> and <i>top</i> to <i>bottom</i> . Results are averaged in $\mathcal{T} = (8T, 9T)$	103
7.9	Computational domain	104
7.10	Boundary conditions. The <i>blue</i> , <i>red</i> , <i>green</i> , <i>cyan</i> shows the inflow, no-slip, periodic and slip boundaries	105
7.11	The coarse mesh around blade <i>left</i> and the mesh refinement <i>right</i> , the coarse, medium and fine meshes from <i>top</i> to <i>bottom</i>	106

7.12	Time-averaged flow field around impeller by streamlines colored by velocity magnitude, $\ \bar{\mathbf{u}}_R\ /U$. Streamlines and velocity magnitude are calculated relative to the impeller. Results are obtained using the coarse, medium and fine meshes (from <i>left</i> to <i>right</i>) and averaged in $\mathcal{T} = (14T, 15T)$	107
B.1	A circular-arc path represented exactly by a quadratic NURBS element in time. This figure was also shown in [2]	114

Tables

5.1	The mesh details. nc , ne and ne_b are the number of control points, quadratic NURBS elements in the whole model and along the bend. The $h_{s,inlet}$ and $h_{s,min}$ are the first and minimum element lengths in the streamwise direction which are located at the inlet and in the curvature	54
6.1	The Reynolds number combinations used in the computations	68
6.2	Number of elements (ne) and control points (nc) in the radial, circumferential and axial directions	70
6.3	Angular momentum (\bar{L}/\bar{L}_{FINE}) and torque $\bar{\Upsilon}_{IB}T/\bar{L}_{FINE}$ of the eight cases with respect to angular momentum from fine mesh	90
7.1	Number of control points (nc) and elements (ne) in three different parts of the flow domain	96
7.2	Number of control points (nc) and elements (ne) in the coarse, medium and fine meshes	105
7.3	Shaft power (P_S), scaled with the experimental value ($P_{S_{exp}}$), at $Q = Q_0$. The values are averaged in $\mathcal{T} = (14T, 15T)$	106

Chapter 1

Introduction

1.1 Background

The rapid development of computer technology has made the numerical approaches more practical, applicable and useful in the past decades. This has made computational modeling more preferable in the field that investigates the flow behavior of a fluid. Computational Fluid Dynamics (CFD) is a branch of fluid mechanics developed to solve fluid flow problems in engineering applications. There are numerous open-source and commercial CFD software developed by engineers and mathematicians in this field. Most of these tools are able to predict a flow accurately comparing to the real behavior of a fluid by solving relevant formulations by different mathematical approaches. Nevertheless, these approaches have been attracting engineers' and mathematicians' attention in order to make them more efficient, such as decreasing the cost of a computation while maintaining high accuracy.

Formulations of fluid dynamics usually contain linear and nonlinear differential equations which can only be solved by evaluating them in a system of algebraic equations. One of the main methods used for this purpose is the Finite Element Method (FEM). For the solution of a system of differential equations, the FEM is set over two main components. The first is the weak (variational) form of the problem and the second is the approximation of the equations in the weak form to the solution. The variational form of the Navier–Stokes equations is given in the following chapters in this dissertation. Even though there is a common belief that FEM has some disadvantages for solving fluid problems, stabilized and multiscale FE techniques address these shortcomings [1–4]. Deeper information about these

techniques is given in Section 1.3.

One of the steps of CFD is the representation of a flow domain. It can be represented by dividing the whole domain into a finite number of elements. In the FEM, these elements are usually constructed by lines. However, a circular-shape computational domain cannot be represented exactly by using straight lines. To approach the actual geometry as much as possible, a large number of the straight lines should be used. Isogeometric Analysis (IGA) was introduced in [5]. With the IGA, the difference between Computer-Aided Design (CAD) of a model and the computational domain in CFD analysis is aimed to be removed. Non-Uniform Rational B-Spline (NURBS) (see [6]) is one of the most common mathematical model used in CAD as well as in CFD analysis with IGA. Usage of the NURBS in CFD analyzes with high-order basis functions makes exact geometry and motion representation possible, and accordingly, it improves the efficiency.

1.2 CFD for turbomachinery flows

Turbomachinery usually has a complicated geometry with high curvatures. Typically, it contains circular shapes and high-speed rotating parts. The flow is multi-scale, including a thin boundary layer, flow separation, recirculation and turbulence behavior. In order to address these difficulties, precise representation of the geometry and motion is essential.

The flow pattern around some critical parts, the pressure change along turbomachinery or a power generated can be calculated in CFD during its design process. This enables engineers to make optimizations in turbomachinery geometry or adjustments in working conditions. Use of turbomachinery at its best efficiency point can also increase its life span. Flow separation or recirculation around an impeller, for example, could decrease the performance or cause some other physical problems reducing its life. The usage of CFD plays an important role to minimize these kinds

problems detecting them in their design process.

The Space–Time (ST) framework, which have been generally developed for flow computations with moving domains, has some efficient and accurate methods for numerical analysis of turbomachinery flows.

1.3 ST methods

The ST methods, introduced in [7], have been developed and used in a large number of practical engineering problems in the recent decades [8]. In the ST framework, formulations of the ST methods written on the ST slabs [9] will be given in the following chapters.

CFD analysis of turbomachinery flows are classified into two categories in this dissertation. One is the turbulent flow and the other is the flow around rotating components. In both of these classes of flow problems, the stability and accuracy of the computations significantly depend on the geometry, motion and boundary condition representations as well as the formulations used to resolve the multiscale flow. The latest versions of the ST methods, with the IGA feature named as “ST-IGA” in [10], the ST Slip Interface (ST-SI), introduced in [11, 12] and the ST Variational Multiscale (ST-VMS), proposed in [10, 13], respond to these difficulties successfully.

1.3.1 ST-IGA

The ST-IGA is a powerful tool to represent a flow domain and its motion accurately using NURBS basis functions. In the ST framework, this higher-order basis functions are employed in both spatial and temporal dimensions. An accurate representation of geometry and motion increases accuracy of the solution making the computations more stable. Moreover, using NURBS basis functions, geometry and motion can be represented exactly, only by a few numbers of degrees of freedom (see Figure 1.1). Representation of a domain by the smaller number of degrees of freedom enables

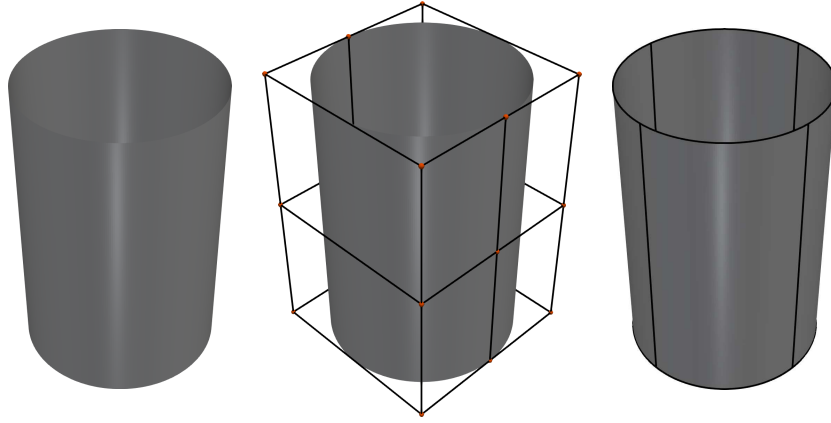


Figure 1.1: Exact representation of a cylinder. From *left to right*, the CAD geometry, the control mesh, and the physical mesh of four elements constructed by NURBS. The *red* points are the control points

the use of the larger time-step sizes, keeping the Courant number at reasonable levels [14]. This feature significantly improves the efficiency of the computations reducing the computational costs.

In CFD, a flow is mostly investigated after it reaches to a time-periodic regime [1]. The developing flow part of the computations, which are sometimes not useful, might be time-consuming. In this situation, a common way to reduce the costs is the utilization of a small number of elements in that part of the computations. Later, a mesh refinement can be made to obtain a more accurate solution in the time-periodic part. Because the ST-IGA also enables us to make the mesh refinement without changing the flow domain, both the initial computations with a coarse mesh and the time-periodic part with finer meshes are solved in the same computational domain, and it increases the accuracy. This cannot be done with traditional methods in complex geometries (see Figure 1.2).

The rotation at a constant angular velocity and the arc path of the rotating parts of turbomachinery can be represented exactly in time. The ST/NURBS Mesh Update Method (STNMUM) was introduced in [15–17] for exact representation of rotation using higher-order basis functions in time. In the traditional methods, the

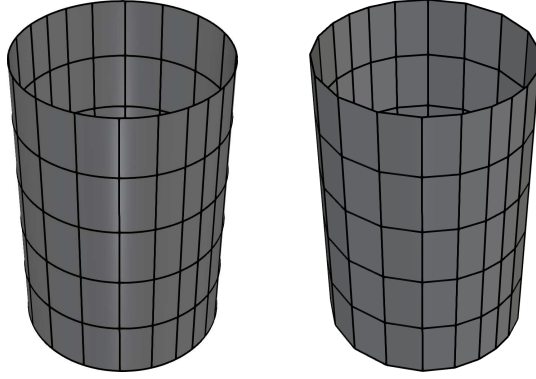


Figure 1.2: An example mesh refinement. NURBS (*left*) and FE (*right*)

stability of the computations of a flow around rotating parts significantly depends on the rotational angle per time step. Use of the STNMUM increases the stability of the computations decreasing this dependency [18].

1.3.2 ST-SI method

Rotation can be represented in several methods as it is explained in Section 1.4. In one of those methods, we compute by moving the mesh surrounding the rotating parts of a computational domain. In this case, the ST-SI method is used to connect the rotating part of a domain to remaining neighbor parts. An interface, which can be an arc and represented exactly by NURBS, is placed between multiple rotating and stationary domains (see Figure 1.3). The ST-SI can also be used between multiple fluid domains with non-matching mesh structures. This enables us to decrease computation costs using coarser meshes in some domains where we have larger scale flow dynamics or with less complex geometries (for example, see [19]).

With the ST-SI, the interface can also be placed between solid and fluid parts of a computational domain. The Dirichlet boundary conditions can be enforced weakly, as introduced in [20] and used in the ST framework in [11,12]. The details are given in the following parts of this dissertation. The weak enforcement is a powerful tool to obtain the boundary layer effect without actually resolving the flow [20]. A trans-

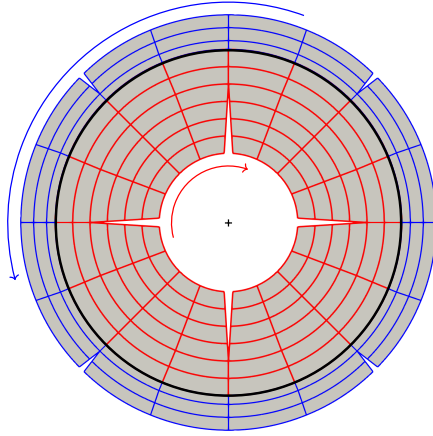


Figure 1.3: An SI (the *black* line) between two rotating (*red* and *blue*) flow domains

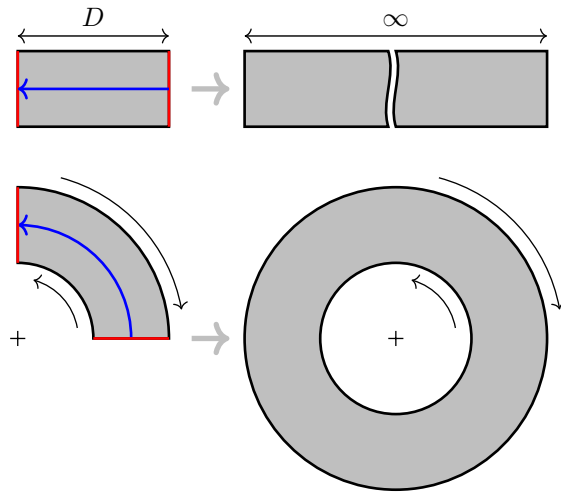


Figure 1.4: An infinite channel (*top*) and a cylindrical computational domain (*bottom*) represented by a translational-periodicity and a rotational-periodicity. The *red* lines represent the boundaries where the periodicity is enforced by the ST-SI. The *blue* arrows denote the translation of the SIs

lational or a rotational-periodicity of a computational domain can be represented by the ST-SI. This, for example, enables calculating a flow independently of the computational domain length [1] or its angle [2] (see Figure 1.4).

1.3.3 ST-VMS method

In turbomachinery flow analysis, the stability of the turbulent flow computations plays an important role on the accuracy and efficiency. The well known stabi-

lization formulations, Streamline-Upwind/Petrov-Galerkin (SUPG) [21], Pressure-Stabilizing/Petrov-Galerkin (PSPG) [22,23] and more accurate VMS [24] are widely used with this purpose. In the ST framework, the SUPG and PSPG stabilizations are used together. This method is named as “ST-SUPS” in [10]. The main tool used in this dissertation to deal with the turbulent flow occurring in turbomachinery flows is the ST-VMS. The ST-VMS with isogeometric discretization is a stabilized formulation and serves as a reliable turbulence model. It contains some additional terms compared to the ST-SUPS and these terms make the ST-VMS more accurate especially in solving the small scale flow dynamics. The VMS with the Arbitrary Lagrangian–Eulerian (ALE) (see [25]) FEM, which is called “ALE-VMS” [26–29], is similar in many aspects to the ST-VMS [30,31].

One of the studies performed to test a turbulent flow computation by the ST-VMS method is [32]. In this study, high Reynolds number ($\text{Re} = 3 \times 10^6$ and 6×10^6) turbulent flows were calculated around airfoils, with variable angle of attack values. The flow domain was represented by different mesh types, and both the conservative and the nonconservative versions of the ST-VMS formulation were used. The numerical results for the lift and drag coefficients were compared with an experiment and a good agreement was observed. In another study [33], a flow of $\text{Re} = 12 \times 10^6$ around wind turbine rotor was calculated using an older version of the ST-VMS, which was proposed in [7, 22, 34–36] and named as Deforming-Spatial-Domain/Stabilized ST (DSD/SST). The torque applied on the wind turbine blades were calculated using various stabilized formulations and compared with a reference study [37] performed using the VMS ALE method. This study, [33], is one of the earliest studies among [38–40] in which a computational domain was represented using a rotational-periodicity with the ST methods. A more recent computation of a turbulent flow around a turbine rotor was performed in [41]. In this study $\text{Re} = 1.1 \times 10^5$ was utilized by the ST-VMS. The geometry was represented by NURBS. The performance

of the turbine was calculated.

Flows around a wind turbine rotor and its tower were computed in [18, 31, 42]. In [18], the effect of mesh and time-step size on the numerical torque values were analyzed. The STNMUM method was also introduced to represent the rotation exactly. In [42], the results from the ST-VMS were compared with the results from the ALE-VMS. In [43–45], flow in a turbocharger turbine and exhaust manifold was analyzed. Here the computational domains were also represented accurately using NURBS with a general purpose NURBS mesh generation method introduced in [43]. The ST-SI method was used to connect the rotating turbine impeller to the rest of the computational domain. Rotation of the impeller was represented exactly by STNMUM moving the surrounding mesh. In the other recent studies, where the rotation was represented exactly, geometry was represented accurately by NURBS and the ST-VMS was used as a core method, a flow in a vertical axis wind turbine [11, 46], in a fan [47], and in a pump with FSI analysis of a string [48–51] were computed.

In [52], a flow around a vehicle and its tires, and in [53] around a disc break, including a thermo-fluid analysis were studied. In [12], the ST-SI Topology Change (ST-SI-TC) method was introduced, and in [12, 19, 54], tire aerodynamics with actual tire geometry and road contact were computed. This method improves the resolution in a boundary layer and can be used in computations with topology changes such as contact between solid surfaces.

In [55–57], heart valve flow computations were computed. The ST-SI-TC method was also used in [58, 59] in more recent heart valve flow computations representing a contact between the valves more accurately. The ST framework was used in some other moving-mesh computations of real-world flow problems. In the flow computations around flapping wings of a locust [15, 60, 61], an accurate geometry and motion representation by NURBS were described from an experiment. Aerodynam-

ics analysis of some space-craft, drogue and ram air parachutes [9, 60, 62–69] was also performed using the ST methods.

1.4 Rotation representation

Motion of the rotating components of turbomachinery can be represented in several ways in the CFD. In two mainly used methods, the reference frame, in which the measurements are made, can be attached outside or inside of the rotating parts. If the reference frame is not attached on a domain, but the domain moves, it is the inertial reference frame (IRF). There are two essential representations, i) the rotational motion and ii) the boundary condition on that. Both representations may not be easily represented exactly. If the reference frame is attached on a domain and rotates with that domain, it is a non-inertial reference frame (NRF). It is useful because the domain does not move on that frame, and rotational motion is represented exactly. However, NRF requires fictitious force in the governing equation, which includes the coupling with the solution. In addition, if there are stationary components, the problem cannot be represented in only the NRF.

1.5 Motivation

This dissertation aims to evaluate the stability and accuracy of the combinations of the ST methods in turbomachinery flow analysis. The conservative and nonconservative forms of the ST-VMS method are evaluated both in the IRF, and also in the NRF for the first time in this dissertation. This research is done considering the preciseness of the geometry representation, rotation representation, boundary condition representations, and conservation properties. A turbulent flow and a flow around rotating parts, which are dominant in turbomachinery flows, are investigated.

First, we started with a challenging turbulent flow analysis [1]. The ST-VMS method was evaluated previously for turbulent-flow analysis in the studies [32,33,41],

however, [41] was a milder test problem, and the others were performed without isogeometric discretization. In this dissertation we computed a turbulent-flow in a U-duct model with a high curvature. The ST-VMS method is used to deal with the multiscale flow, which includes a thin boundary layer, flow separation, recirculation and turbulence behavior. A circular-arc geometry is represented exactly by NURBS using the ST-IGA. A fully-developed flow field is calculated by enforcing a translational-periodicity by the ST-SI method. The numerical output is compared with an experiment.

Next, we focused on rotational geometries [2]. The conservative and nonconservative forms of the ST-VMS method is used in the IRF, as well as in the NRF introduced in the ST framework in this dissertation. A circular-arc geometry is represented exactly by NURBS in space using the ST-IGA. An exact representation of rotation is also utilized by the STNMUM. The problem geometry is represented using the translational-periodicity and rotational-periodicity enforced by the ST-SI. Two different representations of the boundary conditions are also tested. Results are evaluated in terms of flow patterns comparing them with an experiment.

Finally, we employ most of these methods evaluated above in a real-world flow problem. The ST-VMS method is used to solve a high Reynolds number turbomachinery flow in both reference frames with a relatively coarse mesh representing the circular geometries accurately using the ST-IGA. The output of this study is also evaluated with an experiment.

1.6 Dissertation overview

In Chapter 2, the governing equations of the incompressible flow in the IRF will be provided. Then the transformation of the governing equations from the IRF to NRF will be explained. Finally, the governing equations in the NRF will be given.

In Chapter 3, the ST-VMS formulation in the IRF will be derived step by step

from the weak form of the Navier–Stokes equations. Both the conservative and nonconservative forms of the ST-VMS will be achieved. Following, the ST-SI formulation will be provided for the SIs between both two fluid domains and also fluid and solid domains. The rotational-periodicity enforcement with the ST-SI will be shown mathematically. In the last section of this chapter, general information about exact representation of geometry, rotation and prescribed velocity will be given with weight definitions and NURBS basis functions in space and time.

In Chapter 4, the ST formulation in the NRF will be derived step by step in the NRF. Both the conservative and nonconservative forms of the ST-VMS formulation will be achieved. In the last section, the global conservation of mass, linear momentum and angular momentum will be provided on the ST-VMS formulation in both reference frames. The test functions used to obtain the balance equations in global space will be provided in detail.

In Chapter 5, a U-duct turbulent flow analysis will be presented. After providing some definitions used for data analysis during this study, the computation results in the periodic straight duct performed to obtain a fully-developed flow profile will be shown. Here the results will be compared with some reference studies. Later, information about problem setup, mesh generation, boundary conditions and computational conditions for the U-duct will be given. Finally, the numerical results, after providing flow development in the U-duct, for the averaging range, mesh refinement and Courant number effects on the solution will be given and compared to experimental data.

In Chapter 6, the well known Taylor–Couette flow analysis will be presented. First, this well known problem and the setup for four different cases will be described. Next, some information about geometry and rotation representation employed specifically for this problem will be provided. Following, the results will be investigated case by case. In the last section, a detailed analysis of global conserva-

tion of angular momentum will be presented.

In Chapter 7, flow analysis in a double-suction centrifugal pump will be shown. First, a short general information about this pump and description of the cases, initial conditions, mesh and computational conditions will be given. Then, the results for a flow development study will be provided. Later, the pump performance will be defined and the output will be compared with an experiment. Some qualitative analyzes will also be provided later, comparing the results at several discharge values. Next, a computational domain with rotational-periodicity around a single blade will be introduced and some numerical results obtained using this reduced domain will be compared to the experiment.

In Chapter 8, the concluding remarks will be presented. All three studies with their settings and results will be summarized in this last chapter.

Chapter 2

Governing Equations

2.1 Navier–Stokes equations

The conservation of momentum and mass balance equations of incompressible flows are written, adapting from [13], in the conservative form on Ω_t as:

$$\rho \left(\frac{\partial \mathbf{u}}{\partial t} + \nabla \cdot (\mathbf{u}\mathbf{u}) - \mathbf{f} \right) - \nabla \cdot \boldsymbol{\sigma} = \mathbf{0}, \quad (2.1)$$

$$\nabla \cdot \mathbf{u} = 0, \quad (2.2)$$

where $\Omega_t \subset \mathbb{R}^{n_{\text{sd}}}$ is the spatial domain with the boundary, Γ_t , at an instant, t . Here n_{sd} is the number of spatial dimensions, ρ , \mathbf{u} and \mathbf{f} are fluid density, velocity and external force. The stress tensor, $\boldsymbol{\sigma}$, is defined by the velocity, dynamic viscosity, μ , identity tensor, \mathbf{I} , and pressure, p , as follows:

$$\boldsymbol{\sigma} = -p\mathbf{I} + 2\mu\boldsymbol{\varepsilon}(\mathbf{u}). \quad (2.3)$$

Here, $\boldsymbol{\varepsilon}(\mathbf{u}) = \frac{1}{2} \left(\nabla \mathbf{u} + (\nabla \mathbf{u})^\top \right)$ is the strain-rate tensor. The boundary Γ_t is split into its complementary subsets as $(\Gamma_t)_g$ and $(\Gamma_t)_h$, which are defined as the essential and natural boundaries. The boundary conditions are represented as $\mathbf{u} = \mathbf{g}$ and $\mathbf{n} \cdot \boldsymbol{\sigma} = \mathbf{h}$. Here, \mathbf{g} and \mathbf{h} are the given functions, and \mathbf{n} is the outward unit normal vector.

2.2 IRF and NRF

A frame of reference is a point of view from which measurements of a vectorial quantity are made. In our field of study, a reference frame can be attached outside of a rotating domain and the vectorial measurements are made considering the effect of rotation. This kind of reference frames is known as IRF. Otherwise, a reference frame can be attached on a rotating domain. This kind of reference frames is known as NRF. As mentioned earlier, we can represent rotation in the IRF with a moving mesh method, or in the NRF implementing the angular velocity into the governing equations. In the NRF, the mesh can be stationary.

2.2.1 Velocity calculation in the NRF

Let us consider that a rectangular flow domain rotates with an angular velocity, ω , as shown in Figure 2.1. If we observe the fluid flow from outside of the domain, in the IRF, we also see the rotation of the domain. On the other hand, we can

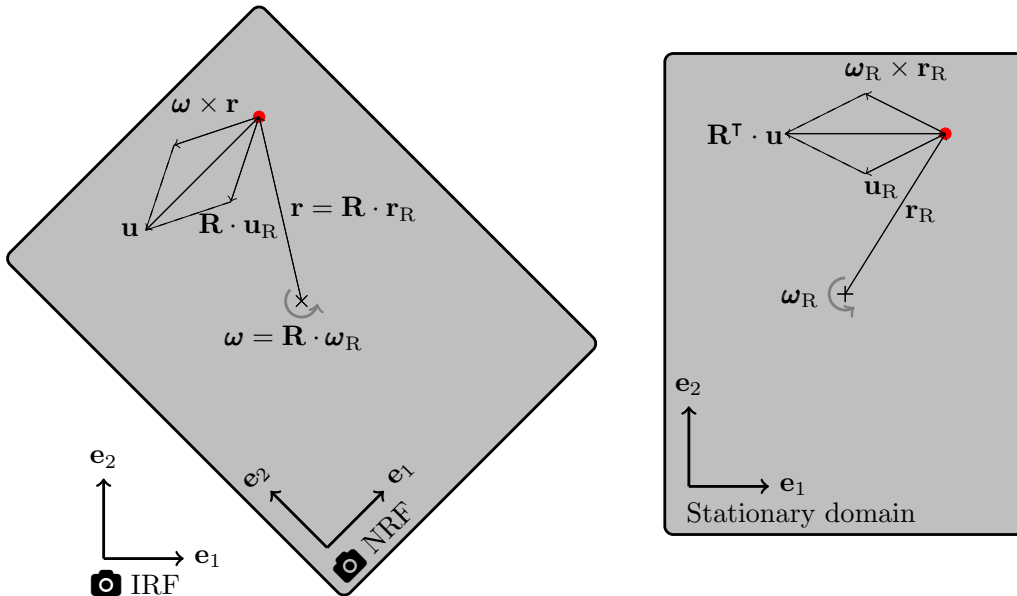



Figure 2.1: Velocity conversion between the IRF and NRF. Arrows represent the vectorial quantities. The *red* point is the location where a measurement is made. The symbol , represents the position where the reference frame is located

attach a camera on the rotating domain to observe the fluid flow in the NRF. We denote the velocity of the fluid on the *red* point in the IRF with \mathbf{u} , and, in the NRF on a stationary domain with \mathbf{u}_R . Here, “R” represents the relative quantities with respect to the stationary domain. The term $\mathbf{r} = \mathbf{x} - \mathbf{x}_0$ is the position vector from the rotation center, \mathbf{x}_0 . The tensor $\mathbf{R} = \hat{\mathbf{e}}_i \mathbf{e}_i$ is defined for transformation between the rotating and stationary domains, where $\frac{d\hat{\mathbf{e}}_i}{dt} = \boldsymbol{\omega} \times \hat{\mathbf{e}}_i$. For conversion from \mathbf{u}_R to \mathbf{u} , we use:

$$\begin{aligned}\mathbf{u} &= \mathbf{R} \cdot \mathbf{u}_R + (\mathbf{R} \cdot \boldsymbol{\omega}_R) \times (\mathbf{R} \cdot \mathbf{r}_R) \\ &= \mathbf{R} \cdot \mathbf{u}_R + \boldsymbol{\omega} \times \mathbf{r}.\end{aligned}\tag{2.4}$$

In this dissertation, we perform our computations in the IRF with a moving mesh, and in the NRF with a stationary mesh. Hence, we derive ST formulations in a stationary mesh in the NRF. Taking time derivative of both sides of Eq. (2.4), we can write:

$$\begin{aligned}\frac{d\mathbf{u}}{dt} &= \mathbf{R} \cdot \frac{d\mathbf{u}_R}{dt} + \frac{d\mathbf{R}}{dt} \cdot \mathbf{u}_R + \dot{\boldsymbol{\omega}} \times \mathbf{r} + \boldsymbol{\omega} \times \mathbf{u} \\ &= \mathbf{R} \cdot \frac{d\mathbf{u}_R}{dt} + \frac{d\hat{\mathbf{e}}_i}{dt} \mathbf{e}_i \cdot \mathbf{u}_R + \dot{\boldsymbol{\omega}} \times \mathbf{r} + \boldsymbol{\omega} \times \mathbf{u} \\ &= \mathbf{R} \cdot \frac{d\mathbf{u}_R}{dt} + \boldsymbol{\omega} \times \hat{\mathbf{e}}_i (u_R)_i + \dot{\boldsymbol{\omega}} \times \mathbf{r} + \boldsymbol{\omega} \times (\mathbf{R} \cdot \mathbf{u}_R + \boldsymbol{\omega} \times \mathbf{r}) \\ &= \mathbf{R} \cdot \frac{d\mathbf{u}_R}{dt} + \boldsymbol{\omega} \times (\mathbf{R} \cdot \mathbf{u}_R) + \dot{\boldsymbol{\omega}} \times \mathbf{r} + \boldsymbol{\omega} \times (\mathbf{R} \cdot \mathbf{u}_R) + \boldsymbol{\omega} \times (\boldsymbol{\omega} \times \mathbf{r}) \\ &= \mathbf{R} \cdot \frac{d\mathbf{u}_R}{dt} + 2\boldsymbol{\omega} \times (\mathbf{R} \cdot \mathbf{u}_R) + \dot{\boldsymbol{\omega}} \times \mathbf{r} + \boldsymbol{\omega} \times (\boldsymbol{\omega} \times \mathbf{r}),\end{aligned}\tag{2.5}$$

where $\dot{\boldsymbol{\omega}} = \frac{d\boldsymbol{\omega}}{dt}$.

2.2.2 Multiple reference frames

In some engineering applications, the IRF and NRF should be used together when there are both rotating and stationary parts. In this situation, the reference frames

are named as multiple reference frames (MRF) or sometimes “frozen rotor” method [70, 71]. In this method, flows in the rotating parts are computed in the NRF, while the rest is computed in the IRF. These computations in the MRF should be continuously transformed into each other during these computations. Using an interface between these domains and solving some transformation equations, this continuous conversion between multiple frames is performed.

2.3 Navier–Stokes equations in the NRF

Equation (2.1) can be written using Eq. (2.5) in the NRF as:

$$\begin{aligned} \rho \mathbf{R} \cdot \left(\frac{\partial \mathbf{u}_R}{\partial t} + \nabla \cdot (\mathbf{u}_R \mathbf{u}_R) + 2 (\mathbf{R}^\top \cdot \boldsymbol{\omega}) \times \left((\mathbf{R}^\top \cdot \mathbf{R}) \cdot \mathbf{u}_R \right) + (\mathbf{R}^\top \cdot \dot{\boldsymbol{\omega}}) \times (\mathbf{R}^\top \cdot \mathbf{r}) \right. \\ \left. + (\mathbf{R}^\top \cdot \boldsymbol{\omega}) \times \left((\mathbf{R}^\top \cdot \boldsymbol{\omega}) \times (\mathbf{R}^\top \cdot \mathbf{r}) \right) - \mathbf{R}^\top \cdot \mathbf{f} \right) - \mathbf{R} \cdot (\nabla \cdot \boldsymbol{\sigma}_R) = \mathbf{0}, \end{aligned} \quad (2.6)$$

where we introduce $\mathbf{f}_R = \mathbf{R}^\top \cdot \mathbf{f}$. From that we can write:

$$\begin{aligned} \rho \mathbf{R} \cdot \left(\frac{\partial \mathbf{u}_R}{\partial t} + \nabla \cdot (\mathbf{u}_R \mathbf{u}_R) + 2 \boldsymbol{\omega}_R \times \mathbf{u}_R + \dot{\boldsymbol{\omega}}_R \times \mathbf{r}_R + \boldsymbol{\omega}_R \times (\boldsymbol{\omega}_R \times \mathbf{r}_R) - \mathbf{f}_R \right) \\ - \mathbf{R} \cdot (\nabla \cdot \boldsymbol{\sigma}_R) = \mathbf{0}, \end{aligned} \quad (2.7)$$

the stress tensor is expressed as:

$$\boldsymbol{\sigma}_R = -p \mathbf{I} + 2\mu \boldsymbol{\varepsilon}(\mathbf{u}_R). \quad (2.8)$$

We note that the angular velocity does not appear in the strain rate tensor, which is given by $\boldsymbol{\varepsilon}(\mathbf{u}_R) = \frac{1}{2} \left(\nabla(\mathbf{u}_R) + (\nabla \mathbf{u}_R)^\top \right)$, because of the fact that $\nabla \cdot (\boldsymbol{\omega} \times \mathbf{r}) = 0$.

Equation (2.2) can also be written applying Eq. (2.4) as follows:

$$\nabla \cdot (\mathbf{R} \cdot \mathbf{u}_R) + \nabla \cdot (\boldsymbol{\omega} \times \mathbf{r}) = 0, \quad (2.9)$$

$$\mathbf{R} \cdot \nabla \cdot \mathbf{u}_R = 0. \quad (2.10)$$

Chapter 3

ST Formulations

Most of the information given in this chapter is adapted from [1, 2, 9–13].

3.1 ST variational formulations

The sets of infinite-dimensional trial functions (\mathcal{S}_u and \mathcal{S}_p) and the corresponding test functions (\mathcal{V}_u and \mathcal{V}_p) are used for velocity and pressure. Here, Eqs. (2.2) and (2.1) are multiplied by the appropriate test functions \mathbf{w} and q associated with velocity and pressure, added, after that integrated over the spatial domain Ω_t as: find $\forall \mathbf{u} \in \mathcal{S}_u$ and $p \in \mathcal{S}_p$, such that $\forall \mathbf{w} \in \mathcal{V}_u$ and $q \in \mathcal{V}_p$:

$$\int_{\Omega_t} \mathbf{w} \cdot \rho \left(\frac{\partial \mathbf{u}}{\partial t} + \nabla \cdot (\mathbf{u}\mathbf{u}) - \mathbf{f} \right) d\Omega - \int_{\Omega_t} \mathbf{w} \cdot (\nabla \cdot \boldsymbol{\sigma}) d\Omega + \int_{\Omega_t} q \nabla \cdot \mathbf{u} d\Omega = 0. \quad (3.1)$$

ST methods are explained in Section 1.3. An ST slab, represented by Q_n , is the slice of the ST domain between t_n and t_{n+1} as shown in Figure 3.1. The \mathbf{u}_n^+ and \mathbf{u}_n^- are the velocity and the \mathbf{w}_n^+ and \mathbf{w}_n^- are the test function values at t_n as approached

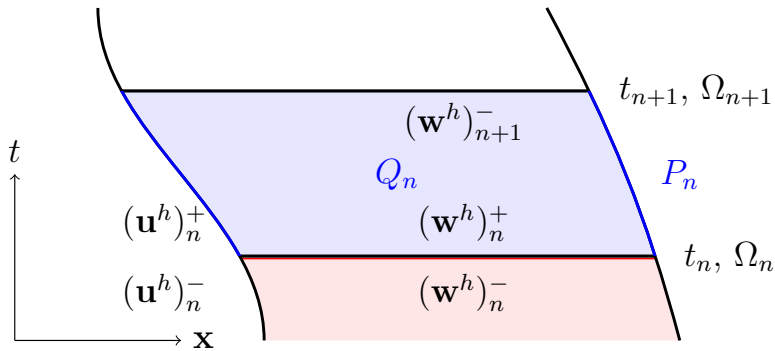


Figure 3.1: Diagram of an ST slab (figure is from [9])

from above and below. P_n is the lateral boundary [9].

We can arrange Eq. (3.1) on Q_n , and write the variational form from [10] as:

$$\int_{Q_n} \mathbf{w} \cdot \rho \left(\frac{\partial \mathbf{u}}{\partial t} + \nabla \cdot (\mathbf{u}\mathbf{u}) - \mathbf{f} \right) dQ - \int_{Q_n} \mathbf{w} \cdot (\nabla \cdot \boldsymbol{\sigma}) dQ + \int_{Q_n} q \nabla \cdot \mathbf{u} dQ = 0. \quad (3.2)$$

Integrating by parts all the terms of Eq. (3.2) except for the term with \mathbf{f} , and enforcing the boundary conditions, we write from [10]:

$$\begin{aligned} & \int_{\Omega_{n+1}} \mathbf{w}_{n+1}^- \cdot \rho \mathbf{u}_{n+1}^- d\Omega - \int_{\Omega_n} \mathbf{w}_n^+ \cdot \rho \mathbf{u}_n^- d\Omega - \int_{Q_n} \frac{\partial \mathbf{w}}{\partial t} \cdot \rho \mathbf{u} dQ \\ & - \int_{(P_n)_h} (\mathbf{w} \cdot \rho \mathbf{u}) (\mathbf{n} \cdot \mathbf{v}) dP + \int_{(P_n)_h} (\mathbf{w} \cdot \rho \mathbf{u}) (\mathbf{n} \cdot \mathbf{u}) dP - \int_{Q_n} \nabla \mathbf{w} : \rho \mathbf{u} \mathbf{u} dQ \\ & - \int_{Q_n} \mathbf{w} \cdot \rho \mathbf{f} dQ - \int_{(P_n)_h} \mathbf{w} \cdot \mathbf{h} dP + \int_{Q_n} \boldsymbol{\varepsilon}(\mathbf{w}) : \boldsymbol{\sigma} dQ \\ & + \int_{P_n} q \mathbf{n} \cdot \mathbf{u} dP - \int_{Q_n} \nabla q \cdot \mathbf{u} dQ = 0, \end{aligned} \quad (3.3)$$

where \mathbf{v} denotes the velocity of the spatial-domain boundary.

3.2 ST-VMS formulation

In the VMS techniques the scale separation of “coarse-scale” and “fine-scale” is made (see [10, 14]) as:

$$\mathbf{u} = \bar{\mathbf{u}} + \mathbf{u}', \quad (3.4)$$

$$\mathbf{w} = \bar{\mathbf{w}} + \mathbf{w}', \quad (3.5)$$

$$p = \bar{p} + p', \quad (3.6)$$

$$q = \bar{q} + q', \quad (3.7)$$

where the overbar and prime shows the coarse-scale and fine-scales, such as $\bar{\mathbf{u}}$ and \mathbf{u}' . Here, we can combine Eq. (3.3) with Eqs. (3.4)–(3.7), temporarily introduce

$\boldsymbol{\sigma}' \equiv \boldsymbol{\sigma} - \bar{\boldsymbol{\sigma}}$, assume that $\boldsymbol{\varepsilon}(\bar{\mathbf{w}}) : 2\mu\nabla\mathbf{u}' = 0$ (see [72, 73]), and write from [13] as:

$$\begin{aligned}
& \int_{\Omega_{n+1}} \bar{\mathbf{w}}_{n+1}^- \cdot \rho \bar{\mathbf{u}}_{n+1}^- d\Omega - \int_{\Omega_n} \bar{\mathbf{w}}_n^+ \cdot \rho \bar{\mathbf{u}}_n^- d\Omega - \int_{Q_n} \frac{\partial \bar{\mathbf{w}}}{\partial t} \cdot \rho (\bar{\mathbf{u}} + \mathbf{u}') dQ \\
& + \int_{(P_n)_h} (\bar{\mathbf{w}} \cdot \rho \bar{\mathbf{u}}) (\mathbf{n} \cdot (\bar{\mathbf{u}} - \mathbf{v})) dP - \int_{Q_n} \nabla \bar{\mathbf{w}} : \rho (\bar{\mathbf{u}} + \mathbf{u}') (\bar{\mathbf{u}} + \mathbf{u}') dQ \\
& - \int_{Q_n} \bar{\mathbf{w}} \cdot \rho \mathbf{f} dQ - \int_{(P_n)_h} \bar{\mathbf{w}} \cdot \mathbf{h} dP + \int_{Q_n} \boldsymbol{\varepsilon}(\bar{\mathbf{w}}) : (\bar{\boldsymbol{\sigma}} - p' \mathbf{I}) dQ \\
& + \int_{P_n} \bar{q} \mathbf{n} \cdot \bar{\mathbf{u}} dP - \int_{Q_n} \nabla \bar{q} \cdot (\bar{\mathbf{u}} + \mathbf{u}') dQ = 0, \tag{3.8}
\end{aligned}$$

where fine-scale solution is set to zero at the ST boundaries. After this step, the fine-scale terms are collected in one place and written adapting from [13] as follows:

$$\begin{aligned}
& \int_{\Omega_{n+1}} \bar{\mathbf{w}}_{n+1}^- \cdot \rho \bar{\mathbf{u}}_{n+1}^- d\Omega - \int_{\Omega_n} \bar{\mathbf{w}}_n^+ \cdot \rho \bar{\mathbf{u}}_n^- d\Omega - \int_{Q_n} \frac{\partial \bar{\mathbf{w}}}{\partial t} \cdot \rho \bar{\mathbf{u}} dQ \\
& + \int_{(P_n)_h} (\bar{\mathbf{w}} \cdot \rho \bar{\mathbf{u}}) (\mathbf{n} \cdot (\bar{\mathbf{u}} - \mathbf{v})) dP - \int_{Q_n} \nabla \bar{\mathbf{w}} : \rho \bar{\mathbf{u}} \bar{\mathbf{u}} dQ - \int_{Q_n} \bar{\mathbf{w}} \cdot \rho \mathbf{f} dQ \\
& - \int_{(P_n)_h} \bar{\mathbf{w}} \cdot \mathbf{h} dP + \int_{Q_n} \boldsymbol{\varepsilon}(\bar{\mathbf{w}}) : \bar{\boldsymbol{\sigma}} dQ + \int_{P_n} \bar{q} \mathbf{n} \cdot \bar{\mathbf{u}} dP - \int_{Q_n} \nabla \bar{q} \cdot \bar{\mathbf{u}} dQ \\
& - \int_{Q_n} \left(\left(\rho \frac{\partial \bar{\mathbf{w}}}{\partial t} + \nabla \bar{q} \right) \cdot \mathbf{u}' + \nabla \bar{\mathbf{w}} : \left(\rho (\mathbf{u}' \bar{\mathbf{u}} + \bar{\mathbf{u}} \mathbf{u}' + \mathbf{u}' \mathbf{u}') + p' \mathbf{I} \right) \right) dQ = 0. \tag{3.9}
\end{aligned}$$

Equation (3.9) can be written in spatially discretized version to obtain the ST-VMS formulation in the conservative form (see [2, 10, 13]) as follows: find $\forall \mathbf{u}^h \in (\mathcal{S}_{\mathbf{u}}^h)_n$

and $p^h \in (\mathcal{S}_p^h)_n$, such that $\forall \mathbf{w}^h \in (\mathcal{V}_u^h)_n$ and $q^h \in (\mathcal{V}_p^h)_n$:

$$\begin{aligned}
& \int_{Q_n} \mathbf{w}^h \cdot \rho \left(\frac{\partial \mathbf{u}^h}{\partial t} + \nabla \cdot (\mathbf{u}^h \mathbf{u}^h) - \mathbf{f}^h \right) dQ \\
& + \int_{Q_n} \boldsymbol{\varepsilon}(\mathbf{w}^h) : \boldsymbol{\sigma}^h dQ - \int_{(P_n)_h} \mathbf{w}^h \cdot \mathbf{h}^h dP \\
& + \int_{Q_n} q^h \nabla \cdot \mathbf{u}^h dQ + \int_{\Omega_n} (\mathbf{w}^h)_n^+ \cdot \rho \left((\mathbf{u}^h)_n^+ - (\mathbf{u}^h)_n^- \right) d\Omega \\
& + \sum_{e=1}^{(n_{el})_n} \int_{Q_n^e} \frac{\tau_{\text{SUPS}}}{\rho} \left(\rho \left(\frac{\partial \mathbf{w}^h}{\partial t} + \mathbf{u}^h \cdot \nabla \mathbf{w}^h \right) + \nabla q^h \right) \cdot \mathbf{r}_M^h dQ \\
& + \sum_{e=1}^{(n_{el})_n} \int_{Q_n^e} \nu_{\text{LSIC}} \nabla \cdot \mathbf{w}^h \rho r_C^h dQ \\
& + \sum_{e=1}^{(n_{el})_n} \int_{Q_n^e} \tau_{\text{SUPS}} \mathbf{r}_M^h \cdot (\nabla \mathbf{w}^h) \cdot \mathbf{u}^h dQ \\
& - \sum_{e=1}^{(n_{el})_n} \int_{Q_n^e} \frac{\tau_{\text{SUPS}}^2}{\rho} \mathbf{r}_M^h \cdot (\nabla \mathbf{w}^h) \cdot \mathbf{r}_M^h dQ = 0. \tag{3.10}
\end{aligned}$$

Here, the superscript “ h ” indicates the functions in a finite-dimensional space. The number and the counter of the ST elements are denoted by n_{el} and e . The fine-scale solutions are represented with τ_{SUPS} and ν_{LSIC} as follows:

$$\mathbf{u}' = -\frac{\tau_{\text{SUPS}}}{\rho} \mathbf{r}_M^h, \tag{3.11}$$

$$p' = -\rho \nu_{\text{LSIC}} r_C^h, \tag{3.12}$$

where \mathbf{r}_M^h and r_C^h are the residuals given by:

$$\mathbf{r}_M^h = \rho \left(\frac{\partial \mathbf{u}^h}{\partial t} + \mathbf{u}^h \cdot \nabla \mathbf{u}^h - \mathbf{f}^h \right) - \nabla \cdot \boldsymbol{\sigma}^h, \tag{3.13}$$

$$r_C^h = \nabla \cdot \mathbf{u}^h. \tag{3.14}$$

The stabilization parameters are given in Appendix A. For more details, see [74, 75].

There is a shortcut derivation, introduced in [13], to obtain the nonconservative form of the ST-VMS from the conservative form given in Eq. (3.10). Integrating by parts two pieces of the fifth expression in Eq. (3.9), following are written from [13]:

$$\begin{aligned}
-\int_{Q_n} \nabla \bar{\mathbf{w}} : \rho \bar{\mathbf{u}} \bar{\mathbf{u}} dQ &= -\int_{(P_n)_h} (\bar{\mathbf{w}} \cdot \rho \bar{\mathbf{u}}) (\mathbf{n} \cdot \bar{\mathbf{u}}) dP + \int_{Q_n} \bar{\mathbf{w}} \cdot \rho (\bar{\mathbf{u}} \cdot \nabla \bar{\mathbf{u}}) dQ \\
&\quad + \int_{Q_n} (\bar{\mathbf{w}} \cdot \rho \bar{\mathbf{u}}) \nabla \cdot \bar{\mathbf{u}} dQ \tag{3.15}
\end{aligned}$$

$$\begin{aligned}
-\int_{Q_n} \nabla \bar{\mathbf{w}} : \rho \mathbf{u}' \bar{\mathbf{u}} dQ &= -\int_{(P_n)_h} (\bar{\mathbf{w}} \cdot \rho \bar{\mathbf{u}}) (\mathbf{n} \cdot \mathbf{u}') dP + \int_{Q_n} \bar{\mathbf{w}} \cdot \rho (\mathbf{u}' \cdot \nabla \bar{\mathbf{u}}) dQ \\
&\quad + \int_{Q_n} (\bar{\mathbf{w}} \cdot \rho \bar{\mathbf{u}}) \nabla \cdot \mathbf{u}' dQ. \tag{3.16}
\end{aligned}$$

Here, $\mathbf{u}' = \mathbf{0}$ on the lateral boundary and addition of the last terms is zero because of Eqs. (2.2) and (3.4). The discrete form of the second term in Eq. (3.15), which is in nonconservative form, replaces the advective term in Eq. (3.10) which is in conservative form. Addition of the last term of Eq. (3.16) to the third piece of the last term in Eq. (3.9) is also zero. From those, we can write the ST-VMS formulation in the nonconservative form in the spatially discretized version as given in [2, 10, 13]

by:

$$\begin{aligned}
& \int_{Q_n} \mathbf{w}^h \cdot \rho \left(\frac{\partial \mathbf{u}^h}{\partial t} + \mathbf{u}^h \cdot \nabla \mathbf{u}^h - \mathbf{f}^h \right) dQ \\
& + \int_{Q_n} \boldsymbol{\varepsilon}(\mathbf{w}^h) : \boldsymbol{\sigma}^h dQ - \int_{(P_n)_h} \mathbf{w}^h \cdot \mathbf{h}^h dP \\
& + \int_{Q_n} q^h \nabla \cdot \mathbf{u}^h dQ + \int_{\Omega_n} (\mathbf{w}^h)_n^+ \cdot \rho \left((\mathbf{u}^h)_n^+ - (\mathbf{u}^h)_n^- \right) d\Omega \\
& + \sum_{e=1}^{(n_{el})_n} \int_{Q_n^e} \frac{\tau_{\text{SUPS}}}{\rho} \left(\rho \left(\frac{\partial \mathbf{w}^h}{\partial t} + \mathbf{u}^h \cdot \nabla \mathbf{w}^h \right) + \nabla q^h \right) \cdot \mathbf{r}_M^h dQ \\
& + \sum_{e=1}^{(n_{el})_n} \int_{Q_n^e} \nu_{\text{LSIC}} \nabla \cdot \mathbf{w}^h \rho r_C dQ \\
& - \sum_{e=1}^{(n_{el})_n} \int_{Q_n^e} \tau_{\text{SUPS}} \mathbf{w}^h \cdot (\mathbf{r}_M^h \cdot \nabla \mathbf{u}^h) dQ \\
& - \sum_{e=1}^{(n_{el})_n} \int_{Q_n^e} \frac{\tau_{\text{SUPS}}^2}{\rho} \mathbf{r}_M^h \cdot (\nabla \mathbf{w}^h) \cdot \mathbf{r}_M^h dQ = 0. \tag{3.17}
\end{aligned}$$

3.3 ST-SI formulation

Most of the information in this section is written from [11, 12], where the ST-SI is proposed. The origin of the ST-SI method is the “sliding interface” method introduced in [76] and used with the ALE-VMS (see, for example, [77]). Two sides of the interface are named as “Side A” and “Side B”. The test functions of velocity and pressure are defined for the Sides A, as \mathbf{w}_A^h and q_A^h , and B, as \mathbf{w}_B^h and q_B^h , and

the ST-SI formulation is written from [1] as follows:

$$\begin{aligned}
& - \int_{(P_n)_{\text{SI}}} \left(q_{\text{B}}^h \mathbf{n}_{\text{B}} - q_{\text{A}}^h \mathbf{n}_{\text{A}} \right) \cdot \frac{1}{2} \left(\mathbf{u}_{\text{B}}^h - \mathbf{u}_{\text{A}}^h \right) dP \\
& - \int_{(P_n)_{\text{SI}}} \rho \mathbf{w}_{\text{B}}^h \cdot \frac{1}{2} \left(\left(\mathcal{F}_{\text{B}}^h - \left| \mathcal{F}_{\text{B}}^h \right| \right) \mathbf{u}_{\text{B}}^h - \left(\mathcal{F}_{\text{B}}^h - \left| \mathcal{F}_{\text{B}}^h \right| \right) \mathbf{u}_{\text{A}}^h \right) dP \\
& - \int_{(P_n)_{\text{SI}}} \rho \mathbf{w}_{\text{A}}^h \cdot \frac{1}{2} \left(\left(\mathcal{F}_{\text{A}}^h - \left| \mathcal{F}_{\text{A}}^h \right| \right) \mathbf{u}_{\text{A}}^h - \left(\mathcal{F}_{\text{A}}^h - \left| \mathcal{F}_{\text{A}}^h \right| \right) \mathbf{u}_{\text{B}}^h \right) dP \\
& + \int_{(P_n)_{\text{SI}}} \left(\mathbf{n}_{\text{B}} \cdot \mathbf{w}_{\text{B}}^h + \mathbf{n}_{\text{A}} \cdot \mathbf{w}_{\text{A}}^h \right) \frac{1}{2} \left(p_{\text{B}}^h + p_{\text{A}}^h \right) dP \\
& - \int_{(P_n)_{\text{SI}}} \left(\mathbf{n}_{\text{B}} \cdot \mathbf{w}_{\text{B}}^h - \mathbf{n}_{\text{A}} \cdot \mathbf{w}_{\text{A}}^h \right) \frac{1}{2} \Delta p dP \\
& - \int_{(P_n)_{\text{SI}}} \left(\mathbf{w}_{\text{B}}^h - \mathbf{w}_{\text{A}}^h \right) \cdot \left(\hat{\mathbf{n}}_{\text{B}} \cdot \mu \left(\boldsymbol{\varepsilon}(\mathbf{u}_{\text{B}}^h) + \boldsymbol{\varepsilon}(\mathbf{u}_{\text{A}}^h) \right) \right) dP \\
& - \gamma \int_{(P_n)_{\text{SI}}} \hat{\mathbf{n}}_{\text{B}} \cdot \mu \left(\boldsymbol{\varepsilon}(\mathbf{w}_{\text{B}}^h) + \boldsymbol{\varepsilon}(\mathbf{w}_{\text{A}}^h) \right) \cdot \left(\mathbf{u}_{\text{B}}^h - \mathbf{u}_{\text{A}}^h \right) dP \\
& + \int_{(P_n)_{\text{SI}}} \frac{\mu C}{h} \left(\mathbf{w}_{\text{B}}^h - \mathbf{w}_{\text{A}}^h \right) \cdot \left(\mathbf{u}_{\text{B}}^h - \mathbf{u}_{\text{A}}^h \right) dP, \tag{3.18}
\end{aligned}$$

where

$$\mathcal{F}_{\text{B}}^h = \mathbf{n}_{\text{B}} \cdot \left(\mathbf{u}_{\text{B}}^h - \mathbf{v}_{\text{B}}^h \right), \tag{3.19}$$

$$\mathcal{F}_{\text{A}}^h = \mathbf{n}_{\text{A}} \cdot \left(\mathbf{u}_{\text{A}}^h - \mathbf{v}_{\text{A}}^h \right), \tag{3.20}$$

$$\hat{\mathbf{n}}_{\text{B}} = \frac{\mathbf{n}_{\text{B}} - \mathbf{n}_{\text{A}}}{\| \mathbf{n}_{\text{B}} - \mathbf{n}_{\text{A}} \|}, \tag{3.21}$$

and, $(P_n)_{\text{SI}}$ is the interface between the periodic boundaries in the ST domain. The outward unit normal vectors are denoted by \mathbf{n}_{A} and \mathbf{n}_{B} , $\gamma = 1$, and C is a dimensionless constant. As it is stated in Remark 3 of [12] and studied in [1], a translational-periodicity can be enforced in the ST-VMS computations. In such cases, an SI is placed where the periodicity is enforced and the computations are carried out while including the corresponding ST-SI term. The term, Δp in Eq. (3.18), represents the pressure change between the SIs. As given in the notation in [11, 68, 69, 78], a

positive Δp value shows higher pressure on Side A. The element length h is shown in Appendix A.

When the SI is used between fluid and solid domains, replacing the Side A velocity with the velocity \mathbf{g}^h , the weakly-enforced Dirichlet conditions (see [20]) are obtained as follows:

$$\begin{aligned}
& - \int_{(P_n)_{\text{SI}}} q_{\text{B}}^h \mathbf{n}_{\text{B}} \cdot \mathbf{u}_{\text{B}}^h dP - \int_{(P_n)_{\text{SI}}} \rho \mathbf{w}_{\text{B}}^h \cdot \mathcal{F}_{\text{B}}^h \mathbf{u}_{\text{B}}^h dP + \int_{(P_n)_{\text{SI}}} q_{\text{B}}^h \mathbf{n}_{\text{B}} \cdot \mathbf{g}^h dP \\
& + \int_{(P_n)_{\text{SI}}} \rho \mathbf{w}_{\text{B}}^h \cdot \frac{1}{2} \left(\left(\mathcal{F}_{\text{B}}^h + |\mathcal{F}_{\text{B}}^h| \right) \mathbf{u}_{\text{B}}^h + \left(\mathcal{F}_{\text{B}}^h - |\mathcal{F}_{\text{B}}^h| \right) \mathbf{g}^h \right) dP \\
& - \int_{(P_n)_{\text{SI}}} \mathbf{w}_{\text{B}}^h \cdot \left(\mathbf{n}_{\text{B}} \cdot \boldsymbol{\sigma}_{\text{B}}^h \right) dP - \gamma \int_{(P_n)_{\text{SI}}} \mathbf{n}_{\text{B}} \cdot 2\mu \boldsymbol{\varepsilon} \left(\mathbf{w}_{\text{B}}^h \right) \cdot \left(\mathbf{u}_{\text{B}}^h - \mathbf{g}^h \right) dP \\
& + \int_{(P_n)_{\text{SI}}} \frac{\mu C}{h_{\text{B}}} \mathbf{w}_{\text{B}}^h \cdot \left(\mathbf{u}_{\text{B}}^h - \mathbf{g}^h \right) dP. \tag{3.22}
\end{aligned}$$

The periodic boundary conditions can be enforced with the ST-SI. In that case, the \mathbf{n}_{A} and \mathbf{n}_{B} become the normal vectors associated with the periodicity surfaces. Then, we define \mathbf{t}_{A} and \mathbf{t}_{B} as unit vectors tangent to those surfaces, and \mathbf{R}_{SI} as the tensor transforming the basis set $(\mathbf{n}_{\text{A}}, \mathbf{t}_{\text{A}}, \mathbf{n}_{\text{A}} \times \mathbf{t}_{\text{A}})$ to $(-\mathbf{n}_{\text{B}}, \mathbf{t}_{\text{B}}, -\mathbf{n}_{\text{B}} \times \mathbf{t}_{\text{B}})$. Then, the ST-SI is described with $\mathbf{R}_{\text{SI}} = -\mathbf{n}_{\text{B}} \mathbf{n}_{\text{A}} + \mathbf{t}_{\text{B}} \mathbf{t}_{\text{A}} - (\mathbf{n}_{\text{B}} \times \mathbf{t}_{\text{B}}) (\mathbf{n}_{\text{A}} \times \mathbf{t}_{\text{A}})$ from [2] as

follows:

$$\begin{aligned}
& - \int_{(P_n)_{\text{SI}}} \left(q_{\text{B}}^h \mathbf{n}_{\text{B}} - \mathbf{R}_{\text{SI}} \cdot q_{\text{A}}^h \mathbf{n}_{\text{A}} \right) \cdot \frac{1}{2} \left(\mathbf{u}_{\text{B}}^h - \mathbf{R}_{\text{SI}} \cdot \mathbf{u}_{\text{A}}^h \right) dP \\
& - \int_{(P_n)_{\text{SI}}} \rho \mathbf{w}_{\text{B}}^h \cdot \frac{1}{2} \left(\left(\mathcal{F}_{\text{B}}^h - |\mathcal{F}_{\text{B}}^h| \right) \mathbf{u}_{\text{B}}^h - \left(\mathcal{F}_{\text{B}}^h - |\mathcal{F}_{\text{B}}^h| \right) \mathbf{R}_{\text{SI}} \cdot \mathbf{u}_{\text{A}}^h \right) dP \\
& - \int_{(P_n)_{\text{SI}}} \rho \left(\mathbf{R}_{\text{SI}} \cdot \mathbf{w}_{\text{A}}^h \right) \cdot \frac{1}{2} \left(\left(\mathcal{F}_{\text{A}}^h - |\mathcal{F}_{\text{A}}^h| \right) \mathbf{R}_{\text{SI}} \cdot \mathbf{u}_{\text{A}}^h - \left(\mathcal{F}_{\text{A}}^h - |\mathcal{F}_{\text{A}}^h| \right) \mathbf{u}_{\text{B}}^h \right) dP \\
& + \int_{(P_n)_{\text{SI}}} \left(\mathbf{n}_{\text{B}} \cdot \mathbf{w}_{\text{B}}^h + \mathbf{n}_{\text{A}} \cdot \mathbf{w}_{\text{A}}^h \right) \frac{1}{2} \left(p_{\text{B}}^h + p_{\text{A}}^h \right) dP \\
& - \int_{(P_n)_{\text{SI}}} \left(\mathbf{n}_{\text{B}} \cdot \mathbf{w}_{\text{B}}^h - \mathbf{n}_{\text{A}} \cdot \mathbf{w}_{\text{A}}^h \right) \frac{1}{2} \Delta p dP \\
& - \int_{(P_n)_{\text{SI}}} \left(\mathbf{w}_{\text{B}}^h - \mathbf{R}_{\text{SI}} \cdot \mathbf{w}_{\text{A}}^h \right) \cdot \left(\hat{\mathbf{n}}_{\text{B}} \cdot \mu \left(\boldsymbol{\varepsilon}(\mathbf{u}_{\text{B}}^h) + \mathbf{R}_{\text{SI}} \cdot \boldsymbol{\varepsilon}(\mathbf{u}_{\text{A}}^h) \cdot \mathbf{R}_{\text{SI}}^{\text{T}} \right) \right) dP \\
& - \gamma \int_{(P_n)_{\text{SI}}} \hat{\mathbf{n}}_{\text{B}} \cdot \mu \left(\boldsymbol{\varepsilon} \left(\mathbf{w}_{\text{B}}^h \right) + \mathbf{R}_{\text{SI}} \cdot \boldsymbol{\varepsilon} \left(\mathbf{w}_{\text{A}}^h \right) \cdot \mathbf{R}_{\text{SI}}^{\text{T}} \right) \cdot \left(\mathbf{u}_{\text{B}}^h - \mathbf{R}_{\text{SI}} \cdot \mathbf{u}_{\text{A}}^h \right) dP \\
& + \int_{(P_n)_{\text{SI}}} \frac{\mu C}{h} \left(\mathbf{w}_{\text{B}}^h - \mathbf{R}_{\text{SI}} \cdot \mathbf{w}_{\text{A}}^h \right) \cdot \left(\mathbf{u}_{\text{B}}^h - \mathbf{R}_{\text{SI}} \cdot \mathbf{u}_{\text{A}}^h \right) dP, \tag{3.23}
\end{aligned}$$

where

$$\hat{\mathbf{n}}_{\text{B}} = \frac{\mathbf{n}_{\text{B}} - \mathbf{R}_{\text{SI}} \cdot \mathbf{n}_{\text{A}}}{\|\mathbf{n}_{\text{B}} - \mathbf{R}_{\text{SI}} \cdot \mathbf{n}_{\text{A}}\|}. \tag{3.24}$$

3.4 Exact representation of geometry and prescribed-velocity

3.4.1 Geometry representation

Exact representation of a computational domain using NURBS is introduced in [5]. Most of the information in this section is written from [2, 3]. An arc can be represented exactly placing the control points as given in Figure 3.2 by a quadratic NURBS element if its angle is less than π . The NURBS weights defined on the

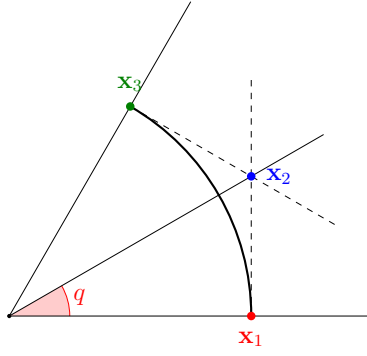


Figure 3.2: A circular-arc represented exactly by a quadratic NURBS element. This figure was also shown in [2]

consisting control points are $w_1 = w_3 = 1$, and $w_2 = \cos q$, and

$$\cos 2q = \frac{\mathbf{x}_1 \cdot \mathbf{x}_3}{r^2}, \quad r = \|\mathbf{x}_1\| = \|\mathbf{x}_3\|, \quad (3.25)$$

and

$$\|\mathbf{x}_2\| = \frac{r}{\cos q}. \quad (3.26)$$

With that, the circular arc can be represented with NURBS basis functions N_a :

$$\mathbf{x}(\xi) = \sum_{a=1}^3 N_a(\xi) \mathbf{x}_a. \quad (3.27)$$

If the arc angle is $q = \frac{\pi}{2}$, for the exact representation we can use two elements, with a uniform knot space, the weight values of $w_1 = w_4 = 1$, and $w_2 = w_3 = \frac{1}{2}$ and placing the control points as illustrated in Figure 3.3. Here, the control points satisfy the conditions

$$\|\mathbf{x}_1\| = \|\mathbf{x}_4\| = r, \quad (3.28)$$

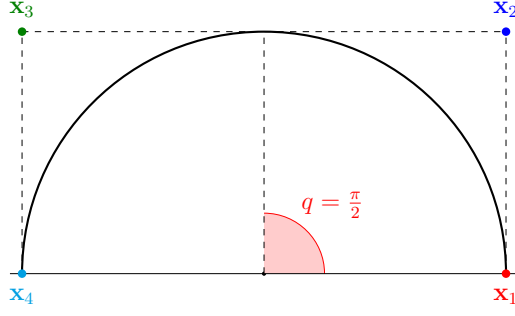


Figure 3.3: A circular arc with $q = \frac{\pi}{2}$ represented exactly by two quadratic NURBS elements. This figure was also shown in [2]

and

$$\|\mathbf{x}_2\| = \|\mathbf{x}_3\| = \frac{\sqrt{2}}{2}r. \quad (3.29)$$

3.4.2 Rotation-generated prescribed velocity

The rotation-generated velocity \mathbf{g}^h can be represented exactly along an arc. For both the cases $q < \pi$ and $q = \pi$, the prescribed velocity is represented exactly as follows.

$$\mathbf{g}^h(\xi) = \boldsymbol{\omega} \times \mathbf{x}^h(\xi) \quad (3.30)$$

$$= \boldsymbol{\omega} \times \sum_{a=1}^3 N_a(\xi) (\mathbf{x}_a) \quad (3.31)$$

$$= \sum_{a=1}^3 N_a(\xi) (\boldsymbol{\omega} \times \mathbf{x}_a). \quad (3.32)$$

and can also be written as $\mathbf{g}^h(\xi) = \sum_{a=1}^3 N_a(\xi) \mathbf{g}_a$, where $\mathbf{g}_a = \boldsymbol{\omega} \times \mathbf{x}_a$.

A circular-arc path and a rotation-generated prescribed velocity along the circular-arc path can also be represented exactly. These are given in Appendix B in detail.

Chapter 4

ST Formulations in the NRF

4.1 ST variational formulations in the NRF

ST variational formulation in a stationary ST domain, $(Q_R)_n$ is written using Eqs. (2.7) and (2.10) in the NRF as follows:

$$\begin{aligned}
& \int_{(Q_R)_n} \mathbf{w}_R \cdot \rho \left(\frac{\partial \mathbf{u}_R}{\partial t} + \nabla \cdot (\mathbf{u}_R \mathbf{u}_R) - \mathbf{f}_R \right) dQ \\
& + \int_{(Q_R)_n} \mathbf{w}_R \cdot \rho (2\boldsymbol{\omega}_R \times \mathbf{u}_R + \dot{\boldsymbol{\omega}}_R \times \mathbf{r}_R + \boldsymbol{\omega}_R \times (\boldsymbol{\omega}_R \times \mathbf{r}_R)) dQ \\
& - \int_{(Q_R)_n} \mathbf{w}_R \cdot (\nabla \cdot \boldsymbol{\sigma}_R) dQ + \int_{(Q_R)_n} q \nabla \cdot \mathbf{u}_R dQ = 0. \tag{4.1}
\end{aligned}$$

Integrating Eq. (4.1) by parts all the terms except for the terms containing Coriolis, centrifugal and external forces, and enforcing the essential and natural boundary conditions,

$$\begin{aligned}
& \int_{(\Omega_R)_{n+1}} (\mathbf{w}_R)_{n+1}^- \cdot \rho (\mathbf{u}_R)_{n+1}^- d\Omega - \int_{(\Omega_R)_n} (\mathbf{w}_R)_n^+ \cdot \rho (\mathbf{u}_R)_n^- d\Omega - \int_{(Q_R)_n} \frac{\partial \mathbf{w}_R}{\partial t} \cdot \rho \mathbf{u}_R dQ \\
& - \int_{((P_R)_n)_h} (\mathbf{w}_R \cdot \rho \mathbf{u}_R) (\mathbf{n} \cdot \mathbf{v}_R) dP + \int_{((P_R)_n)_h} (\mathbf{w}_R \cdot \rho \mathbf{u}_R) (\mathbf{n} \cdot \mathbf{u}_R) dP \\
& - \int_{(Q_R)_n} \nabla \mathbf{w}_R : \rho \mathbf{u}_R \mathbf{u}_R dQ - \int_{(Q_R)_n} \mathbf{w}_R \cdot \rho \mathbf{f}_R dQ \\
& + \int_{(Q_R)_n} \mathbf{w}_R \cdot \rho (2\boldsymbol{\omega}_R \times \mathbf{u}_R + \dot{\boldsymbol{\omega}}_R \times \mathbf{r}_R + \boldsymbol{\omega}_R \times (\boldsymbol{\omega}_R \times \mathbf{r}_R)) dQ \\
& - \int_{((P_R)_n)_h} \mathbf{w}_R \cdot \mathbf{h}_R dP + \int_{(Q_R)_n} \boldsymbol{\varepsilon}(\mathbf{w}_R) : \boldsymbol{\sigma}_R dQ \\
& + \int_{(P_R)_n} q \mathbf{n} \cdot \mathbf{u}_R dP - \int_{(Q_R)_n} \nabla q \cdot \mathbf{u}_R dQ = 0, \tag{4.2}
\end{aligned}$$

is obtained. Here, Ω_R is the stationary spatial-domain and \mathbf{v}_R is the velocity of the spatial-domain boundary, $(P_R)_n$. It is zero because the boundary does not move.

4.2 ST-VMS formulation in the NRF

Similar to Eq. (3.4), coarse-scale and fine-scale separation can be made for the relative velocity vector and the corresponding test function in the stationary domain as follows:

$$\mathbf{u}_R = \bar{\mathbf{u}}_R + \mathbf{u}'_R, \quad (4.3)$$

$$\mathbf{w}_R = \bar{\mathbf{w}}_R + \mathbf{w}'_R. \quad (4.4)$$

Scale separation for pressure and the corresponding test function q are the same in the NRF as given in Eqs. (3.6) and (3.7) in the IRF. Therefore, temporarily introducing $\boldsymbol{\sigma}'_R \equiv \boldsymbol{\sigma}_R - \bar{\boldsymbol{\sigma}}_R$, and assuming $\boldsymbol{\varepsilon}(\bar{\mathbf{w}}_R) : 2\mu\nabla\mathbf{u}'_R = 0$ (see [72, 73]), the scale separation is made in Eq. (4.2) as follows:

$$\begin{aligned} & \int_{(\Omega_R)_{n+1}} (\bar{\mathbf{w}}_R)_{n+1}^- \cdot \rho (\bar{\mathbf{u}}_R)_{n+1}^- d\Omega - \int_{(\Omega_R)_n} (\bar{\mathbf{w}}_R)_n^+ \cdot \rho (\bar{\mathbf{u}}_R)_n^- d\Omega \\ & - \int_{(Q_R)_n} \frac{\partial \bar{\mathbf{w}}_R}{\partial t} \cdot \rho (\bar{\mathbf{u}}_R + \mathbf{u}'_R) dQ + \int_{((P_R)_n)_h} (\bar{\mathbf{w}}_R \cdot \rho \bar{\mathbf{u}}_R) (\mathbf{n} \cdot (\bar{\mathbf{u}}_R - \mathbf{v}_R)) dP \\ & - \int_{(Q_R)_n} \nabla \bar{\mathbf{w}}_R : \rho (\bar{\mathbf{u}}_R + \mathbf{u}'_R) (\bar{\mathbf{u}}_R + \mathbf{u}'_R) dQ - \int_{(Q_R)_n} \bar{\mathbf{w}}_R \cdot \rho \mathbf{f}_R dQ \\ & + \int_{(Q_R)_n} \bar{\mathbf{w}}_R \cdot \rho \left(2\boldsymbol{\omega}_R \times (\bar{\mathbf{u}}_R + \mathbf{u}'_R) + \dot{\boldsymbol{\omega}}_R \times \mathbf{r}_R + \boldsymbol{\omega}_R \times (\boldsymbol{\omega}_R \times \mathbf{r}_R) \right) dQ \\ & - \int_{((P_R)_n)_h} \bar{\mathbf{w}}_R \cdot \mathbf{h}_R dP + \int_{(Q_R)_n} \boldsymbol{\varepsilon}(\bar{\mathbf{w}}_R) : (\bar{\boldsymbol{\sigma}}_R - p'\mathbf{I}) dQ \\ & + \int_{(P_R)_n} \bar{q} \mathbf{n} \cdot \bar{\mathbf{u}}_R dP - \int_{(Q_R)_n} \nabla \bar{q} \cdot (\bar{\mathbf{u}}_R + \mathbf{u}'_R) dQ = 0, \end{aligned} \quad (4.5)$$

where fine-scale solution is set to zero at the spatial and temporal boundaries. After this step, the fine-scale terms are collected in one place, and the formulation is

written as follows:

$$\begin{aligned}
& \int_{(\Omega_R)_{n+1}} (\bar{\mathbf{w}}_R)_{n+1}^- \cdot \rho (\bar{\mathbf{u}}_R)_{n+1}^- \, d\Omega - \int_{(\Omega_R)_n} (\bar{\mathbf{w}}_R)_n^+ \cdot \rho (\bar{\mathbf{u}}_R)_n^- \, d\Omega \\
& - \int_{(Q_R)_n} \frac{\partial \bar{\mathbf{w}}_R}{\partial t} \cdot \rho \bar{\mathbf{u}}_R \, dQ + \int_{((P_R)_n)_h} (\bar{\mathbf{w}}_R \cdot \rho \bar{\mathbf{u}}_R) (\mathbf{n} \cdot (\bar{\mathbf{u}}_R - \mathbf{v}_R)) \, dP \\
& - \int_{(Q_R)_n} \nabla \bar{\mathbf{w}}_R : \rho \bar{\mathbf{u}}_R \bar{\mathbf{u}}_R \, dQ - \int_{(Q_R)_n} \bar{\mathbf{w}}_R \cdot \rho \mathbf{f}_R \, dQ \\
& + \int_{(Q_R)_n} \bar{\mathbf{w}}_R \cdot \rho (2\boldsymbol{\omega}_R \times \bar{\mathbf{u}}_R + \dot{\boldsymbol{\omega}}_R \times \mathbf{r}_R + \boldsymbol{\omega}_R \times (\boldsymbol{\omega}_R \times \mathbf{r}_R)) \, dQ \\
& - \int_{((P_R)_n)_h} \bar{\mathbf{w}}_R \cdot \mathbf{h}_R \, dP + \int_{(Q_R)_n} \boldsymbol{\varepsilon}(\bar{\mathbf{w}}_R) : \bar{\boldsymbol{\sigma}}_R \, dQ \\
& + \int_{(P_R)_n} \bar{q} \mathbf{n} \cdot \bar{\mathbf{u}}_R \, dP - \int_{(Q_R)_n} \nabla \bar{q} \cdot \bar{\mathbf{u}}_R \, dQ \\
& - \int_{(Q_R)_n} \left(\left(\rho \frac{\partial \bar{\mathbf{w}}_R}{\partial t} + \nabla \bar{q} \right) \cdot \mathbf{u}'_R \right. \\
& \quad \left. + \nabla \bar{\mathbf{w}}_R : \left(\rho (\mathbf{u}'_R \bar{\mathbf{u}}_R + \bar{\mathbf{u}}_R \mathbf{u}'_R + \mathbf{u}'_R \mathbf{u}'_R) + p' \mathbf{I} \right) \right) \, dQ = 0. \quad (4.6)
\end{aligned}$$

Equation (4.6) can be written in spatially discretized version to obtain the ST-VMS equation in conservative form as follows (see [2, 10, 13]): find $\forall \mathbf{u}_R^h \in (\mathcal{S}_u^h)_n$ and

$p^h \in (\mathcal{S}_p^h)_n$, such that $\forall \mathbf{w}_R^h \in (\mathcal{V}_u^h)_n$ and $q^h \in (\mathcal{V}_p^h)_n$:

$$\begin{aligned}
& \int_{(Q_R)_n} \mathbf{w}_R^h \cdot \rho \left(\frac{\partial \mathbf{u}_R^h}{\partial t} + \nabla \cdot (\mathbf{u}_R^h \mathbf{u}_R^h) - \mathbf{f}_R^h \right) dQ \\
& + \int_{(Q_R)_n} \mathbf{w}_R^h \cdot \rho \left(2\boldsymbol{\omega}_R \times \mathbf{u}_R^h + \dot{\boldsymbol{\omega}}_R \times \mathbf{r}_R^h + \boldsymbol{\omega}_R \times (\boldsymbol{\omega}_R \times \mathbf{r}_R^h) \right) dQ \\
& + \int_{(Q_R)_n} \boldsymbol{\varepsilon}(\mathbf{w}_R^h) : \boldsymbol{\sigma}_R^h dQ - \int_{((P_R)_n)_h} \mathbf{w}_R^h \cdot \mathbf{h}_R^h dP \\
& + \int_{(Q_R)_n} q^h \nabla \cdot \mathbf{u}_R^h dQ + \int_{(\Omega_R)_n} (\mathbf{w}_R^h)_n^+ \cdot \rho \left((\mathbf{u}_R^h)_n^+ - (\mathbf{u}_R^h)_n^- \right) d\Omega \\
& + \sum_{e=1}^{(n_{el})_n} \int_{(Q_R)_n^e} \frac{\tau_{\text{SUPS}}}{\rho} \left(\rho \left(\frac{\partial \mathbf{w}_R^h}{\partial t} + \mathbf{u}_R^h \cdot \nabla \mathbf{w}_R^h \right) + \nabla q^h \right) \cdot (\mathbf{r}_M^h)_R dQ \\
& + \sum_{e=1}^{(n_{el})_n} \int_{(Q_R)_n^e} \nu_{\text{LSIC}} \nabla \cdot \mathbf{w}_R^h \rho (r_C^h)_R dQ \\
& + \sum_{e=1}^{(n_{el})_n} \int_{(Q_R)_n^e} \tau_{\text{SUPS}} (\mathbf{r}_M^h)_R \cdot (\nabla \mathbf{w}_R^h) \cdot \mathbf{u}_R^h dQ \\
& - \sum_{e=1}^{(n_{el})_n} \int_{(Q_R)_n^e} \frac{\tau_{\text{SUPS}}^2}{\rho} (\mathbf{r}_M^h)_R \cdot (\nabla \mathbf{w}_R^h) \cdot (\mathbf{r}_M^h)_R dQ = 0. \tag{4.7}
\end{aligned}$$

Here, the fine-scale solutions are represented in the NRF as follows:

$$\mathbf{u}'_R = -\frac{\tau_{\text{SUPS}}}{\rho} (\mathbf{r}_M^h)_R, \tag{4.8}$$

$$p' = -\rho \nu_{\text{LSIC}} (r_C^h)_R, \tag{4.9}$$

where the residuals are given by:

$$\begin{aligned}
(\mathbf{r}_M^h)_R &= \rho \left(\frac{\partial \mathbf{u}_R^h}{\partial t} + \mathbf{u}_R^h \cdot \nabla \mathbf{u}_R^h + 2\boldsymbol{\omega}_R \times \mathbf{u}_R^h + \dot{\boldsymbol{\omega}}_R \times \mathbf{r}_R^h + \boldsymbol{\omega}_R \times (\boldsymbol{\omega}_R \times \mathbf{r}_R^h) - \mathbf{f}_R^h \right) \\
&\quad - \nabla \cdot \boldsymbol{\sigma}_R^h, \tag{4.10}
\end{aligned}$$

and

$$\left(r_C^h\right)_R = \nabla \cdot \mathbf{u}_R^h. \quad (4.11)$$

The shortcut derivation to obtain the nonconservative form in the NRF is made, in a similar way as given in Eqs. (3.15) and (3.16), using the fifth term in Eq. (4.6) as follows:

$$\begin{aligned} - \int_{(Q_R)_n} \nabla \bar{\mathbf{w}}_R : \rho \bar{\mathbf{u}}_R \bar{\mathbf{u}}_R dQ &= - \int_{((P_R)_n)_h} (\bar{\mathbf{w}}_R \cdot \rho \bar{\mathbf{u}}_R) (\mathbf{n} \cdot \bar{\mathbf{u}}_R) dP \\ &\quad + \int_{(Q_R)_n} \bar{\mathbf{w}}_R \cdot \rho (\bar{\mathbf{u}}_R \cdot \nabla \bar{\mathbf{u}}_R) dQ \\ &\quad + \int_{(Q_R)_n} (\bar{\mathbf{w}}_R \cdot \rho \bar{\mathbf{u}}_R) \nabla \cdot \bar{\mathbf{u}}_R dQ, \end{aligned} \quad (4.12)$$

$$\begin{aligned} - \int_{(Q_R)_n} \nabla \bar{\mathbf{w}}_R : \rho \mathbf{u}'_R \bar{\mathbf{u}}_R dQ &= - \int_{((P_R)_n)_h} (\bar{\mathbf{w}}_R \cdot \rho \bar{\mathbf{u}}_R) (\mathbf{n} \cdot \mathbf{u}'_R) dP \\ &\quad + \int_{(Q_R)_n} \bar{\mathbf{w}}_R \cdot \rho (\mathbf{u}'_R \cdot \nabla \bar{\mathbf{u}}_R) dQ \\ &\quad + \int_{(Q_R)_n} (\bar{\mathbf{w}}_R \cdot \rho \bar{\mathbf{u}}_R) \nabla \cdot \mathbf{u}'_R dQ, \end{aligned} \quad (4.13)$$

where $\mathbf{u}'_R = \mathbf{0}$ on the lateral boundary and addition of the last terms is zero because of Eqs. (2.10) and (4.3). The discrete form of the second term in Eq. (4.12), which is in nonconservative form, replaces the advective term in Eq. (4.7) which is in conservative form. Addition of the last term of Eq. (4.13) to the third piece of the last term in Eq. (4.6) is also zero. From those, we can write the spatially discretized

version of the ST-VMS formulation in the nonconservative form in the NRF by:

$$\begin{aligned}
& \int_{(Q_R)_n} \mathbf{w}_R^h \cdot \rho \left(\frac{\partial \mathbf{u}_R^h}{\partial t} + \mathbf{u}_R^h \cdot \nabla \mathbf{u}_R^h - \mathbf{f}_R^h \right) dQ \\
& + \int_{(Q_R)_n} \mathbf{w}_R^h \cdot \rho \left(2\boldsymbol{\omega}_R \times \mathbf{u}_R^h + \dot{\boldsymbol{\omega}}_R \times \mathbf{r}_R^h + \boldsymbol{\omega}_R \times (\boldsymbol{\omega}_R \times \mathbf{r}_R^h) \right) dQ \\
& + \int_{(Q_R)_n} \boldsymbol{\varepsilon} \left(\mathbf{w}_R^h \right) : \boldsymbol{\sigma}_R^h dQ - \int_{((P_R)_n)_h} \mathbf{w}_R^h \cdot \mathbf{h}_R^h dP \\
& + \int_{(Q_R)_n} q^h \nabla \cdot \mathbf{u}_R^h dQ + \int_{(\Omega_R)_n} \left(\mathbf{w}_R^h \right)_n^+ \cdot \rho \left(\left(\mathbf{u}_R^h \right)_n^+ - \left(\mathbf{u}_R^h \right)_n^- \right) d\Omega \\
& + \sum_{e=1}^{(n_{el})_n} \int_{(Q_R)_n^e} \frac{\tau_{\text{SUPS}}}{\rho} \left(\rho \left(\frac{\partial \mathbf{w}_R^h}{\partial t} + \mathbf{u}_R^h \cdot \nabla \mathbf{w}_R^h \right) + \nabla q^h \right) \cdot \left(\mathbf{r}_M^h \right)_R dQ \\
& + \sum_{e=1}^{(n_{el})_n} \int_{(Q_R)_n^e} \nu_{\text{LSIC}} \nabla \cdot \mathbf{w}_R^h \rho \left(r_C^h \right)_R dQ \\
& - \sum_{e=1}^{(n_{el})_n} \int_{(Q_R)_n^e} \tau_{\text{SUPS}} \mathbf{w}_R^h \cdot \left(\left(\mathbf{r}_M^h \right)_R \cdot \nabla \mathbf{u}_R^h \right) dQ \\
& - \sum_{e=1}^{(n_{el})_n} \int_{(Q_R)_n^e} \frac{\tau_{\text{SUPS}}^2}{\rho} \left(\mathbf{r}_M^h \right)_R \cdot \left(\nabla \mathbf{w}_R^h \right) \cdot \left(\mathbf{r}_M^h \right)_R dQ = 0. \tag{4.14}
\end{aligned}$$

4.3 Global conservation of mass and momentum

For global conservation of mass and momentum, we first transform the ST-VMS formulation from the stationary domain to the same domain as in the IRF, then convert from the NRF to IRF. With this purpose, we write from Section 2.2.1 as follows:

$$\mathbf{R} \cdot \mathbf{u}_R^h = \mathbf{u}^h - \boldsymbol{\omega} \times \mathbf{r}^h. \tag{4.15}$$

Equation (2.5) is arranged in the discrete space as:

$$\begin{aligned} & \mathbf{R} \cdot \left(\frac{\partial \mathbf{u}_R^h}{\partial t} + \nabla \cdot \left(\mathbf{u}_R^h \mathbf{u}_R^h \right) + 2\boldsymbol{\omega}_R \times \mathbf{u}_R^h + \dot{\boldsymbol{\omega}}_R \times \mathbf{r}_R^h + \boldsymbol{\omega}_R \times \left(\boldsymbol{\omega}_R \times \mathbf{r}_R^h \right) \right) \\ &= \frac{\partial \mathbf{u}^h}{\partial t} + \nabla \cdot \left(\mathbf{u}^h \mathbf{u}^h \right). \end{aligned} \quad (4.16)$$

Starting from Eq. (4.16) and using $\nabla \cdot \mathbf{u}_R^h = \nabla \cdot \mathbf{u}^h$, we can write:

$$\begin{aligned} & \mathbf{R} \cdot \left(\frac{\partial \mathbf{u}_R^h}{\partial t} + \mathbf{u}_R^h \cdot \nabla \mathbf{u}_R^h + 2\boldsymbol{\omega}_R \times \mathbf{u}_R^h + \dot{\boldsymbol{\omega}}_R \times \mathbf{r}_R^h + \boldsymbol{\omega}_R \times \left(\boldsymbol{\omega}_R \times \mathbf{r}_R^h \right) \right) \\ &= \frac{\partial \mathbf{u}^h}{\partial t} + \nabla \cdot \left(\mathbf{u}^h \mathbf{u}^h \right). \end{aligned} \quad (4.17)$$

The conservative form of the ST-VMS formulation given in Eq. (4.7), can be converted into the IRF with Eqs. (4.15) and (4.16) as follows:

$$\begin{aligned} & \int_{Q_n} \mathbf{w}^h \cdot \rho \left(\frac{\partial \mathbf{u}^h}{\partial t} + \nabla \cdot \left(\mathbf{u}^h \mathbf{u}^h \right) - \mathbf{f}^h \right) dQ \\ &+ \int_{Q_n} \boldsymbol{\varepsilon} \left(\mathbf{w}^h \right) : \boldsymbol{\sigma}^h dQ - \int_{(P_n)_h} \mathbf{w}^h \cdot \mathbf{h}^h dP \\ &+ \int_{Q_n} q^h \nabla \cdot \mathbf{u}^h dQ + \int_{\Omega_n} \left(\mathbf{w}^h \right)_n^+ \cdot \rho \left(\left(\mathbf{u}^h \right)_n^+ - \left(\mathbf{u}^h \right)_n^- \right) d\Omega \\ &+ \int_{Q_n} \frac{\tau_{\text{SUPS}}}{\rho} \left(\rho \left(\frac{\partial \mathbf{w}^h}{\partial t} + \left(\mathbf{u}^h - \boldsymbol{\omega} \times \mathbf{r}^h \right) \cdot \nabla \mathbf{w}^h \right) + \nabla q^h \right) \cdot \mathbf{r}_M^h dQ \\ &+ \int_{Q_n} \nu_{\text{LSIC}} \nabla \cdot \mathbf{w}^h \rho r_C^h dQ \\ &+ \int_{Q_n} \tau_{\text{SUPS}} \mathbf{r}_M^h \cdot \left(\nabla \mathbf{w}^h \right) \cdot \left(\mathbf{u}^h - \boldsymbol{\omega} \times \mathbf{r}^h \right) dQ \\ &- \int_{Q_n} \frac{\tau_{\text{SUPS}}^2}{\rho} \mathbf{r}_M^h \cdot \left(\nabla \mathbf{w}^h \right) \cdot \mathbf{r}_M^h dQ = 0. \end{aligned} \quad (4.18)$$

Here, we remind that $\nabla \cdot (\boldsymbol{\omega} \times \mathbf{r}^h) = 0$. We also note that the $(\mathbf{r}_M^h)_R$ is converted by using Eq. (4.17) in Eq. (4.10), we obtain \mathbf{r}_M^h as given in Eq. (3.13).

The nonconservative form of the ST-VMS formulation given in Eq. (4.14), can

be converted into the IRF with Eqs. (4.15) and (4.17) as follows:

$$\begin{aligned}
& \int_{Q_n} \mathbf{w}^h \cdot \rho \left(\frac{\partial \mathbf{u}^h}{\partial t} + \mathbf{u}^h \cdot \nabla \mathbf{u}^h - \mathbf{f}^h \right) dQ \\
& + \int_{Q_n} \boldsymbol{\varepsilon}(\mathbf{w}^h) : \boldsymbol{\sigma}^h dQ - \int_{(P_n)_h} \mathbf{w}^h \cdot \mathbf{h}^h dP \\
& + \int_{Q_n} q^h \nabla \cdot \mathbf{u}^h dQ + \int_{\Omega_n} (\mathbf{w}^h)_n^+ \cdot \rho \left((\mathbf{u}^h)_n^+ - (\mathbf{u}^h)_n^- \right) d\Omega \\
& + \int_{Q_n} \frac{\tau_{\text{SUPS}}}{\rho} \left(\rho \left(\frac{\partial \mathbf{w}^h}{\partial t} + (\mathbf{u}^h - \boldsymbol{\omega} \times \mathbf{r}^h) \cdot \nabla \mathbf{w}^h \right) + \nabla q^h \right) \cdot \mathbf{r}_M^h dQ \\
& + \int_{Q_n} \nu_{\text{LSIC}} \nabla \cdot \mathbf{w}^h \rho r_C^h dQ \\
& - \int_{Q_n} \tau_{\text{SUPS}} \mathbf{w}^h \cdot \left(\mathbf{r}_M^h \cdot \nabla (\mathbf{u}^h - \boldsymbol{\omega} \times \mathbf{r}^h) \right) dQ \\
& - \int_{Q_n} \frac{\tau_{\text{SUPS}}^2}{\rho} \mathbf{r}_M^h \cdot (\nabla \mathbf{w}^h) \cdot \mathbf{r}_M^h dQ = 0. \tag{4.19}
\end{aligned}$$

4.3.1 Global conservation of mass

The weighting functions are \mathbf{w}^h and q^h we used in the discrete geometry. For global conservation of mass, these functions can be set in the ST-VMS equations as $\mathbf{w}^h \leftarrow \mathbf{0}$ and $q^h \leftarrow 1$. For similar studies, please see [26, 79–81]. Hence, the following can be obtained with a simple calculation:

$$\int_{P_n} \mathbf{n} \cdot \mathbf{u}^h dP = 0. \tag{4.20}$$

This is true for both in the conservative and nonconservative forms of the ST-VMS formulation in the both reference frames. Eq. (4.20) shows that both versions of the ST-VMS formulations in both frames are globally mass conservative.

4.3.2 Global conservation of linear momentum

Conservative version

We can set the weighting function used for mass balance equation to zero ($q^h \leftarrow 0$) to find the global momentum conservation formulation. Because \mathbf{w}^h is a vector function, i th Cartesian basis vector \mathbf{e}_i is used (see [26,80,81]) to test the conservation properties using the ST-VMS formulations.

In Eq. (4.18), replacing the test functions we obtain:

$$\begin{aligned}
& \int_{Q_n} \mathbf{e}_i \cdot \rho \left(\frac{\partial \mathbf{u}^h}{\partial t} + \nabla \cdot (\mathbf{u}^h \mathbf{u}^h) - \mathbf{f}^h \right) dQ \\
& + \int_{Q_n} \varepsilon(\mathbf{e}_i) : \boldsymbol{\sigma}^h dQ - \int_{(P_n)_h} \mathbf{e}_i \cdot \mathbf{h}^h dP \\
& + \int_{\Omega_n} \mathbf{e}_i \cdot \rho \left((\mathbf{u}^h)_n^+ - (\mathbf{u}^h)_n^- \right) d\Omega \\
& + \int_{Q_n} \frac{\tau_{\text{SUPS}}}{\rho} \left(\rho \left(\frac{\partial \mathbf{e}_i}{\partial t} + (\mathbf{u}^h - \boldsymbol{\omega} \times \mathbf{r}^h) \cdot \nabla \mathbf{e}_i \right) \right) \cdot \mathbf{r}_M^h dQ \\
& + \int_{Q_n} \nu_{\text{LSIC}} \nabla \cdot \mathbf{e}_i \rho r_C^h dQ \\
& + \int_{Q_n} \tau_{\text{SUPS}} \mathbf{r}_M^h \cdot (\nabla \mathbf{e}_i) \cdot (\mathbf{u}^h - \boldsymbol{\omega} \times \mathbf{r}^h) dQ \\
& - \int_{Q_n} \frac{\tau_{\text{SUPS}}^2}{\rho} \mathbf{r}_M^h \cdot (\nabla \mathbf{e}_i) \cdot \mathbf{r}_M^h dQ = 0. \tag{4.21}
\end{aligned}$$

Here, applying $\frac{\partial \mathbf{e}_i}{\partial t} = 0$, $\nabla \mathbf{e}_i = \mathbf{0}$ and $\varepsilon(\mathbf{e}_i) = \mathbf{0}$, we can write:

$$\begin{aligned}
& \int_{Q_n} \mathbf{e}_i \cdot \rho \left(\frac{\partial \mathbf{u}^h}{\partial t} + \nabla \cdot (\mathbf{u}^h \mathbf{u}^h) - \mathbf{f}^h \right) dQ \\
& + \int_{\Omega_n} \mathbf{e}_i \cdot \rho \left((\mathbf{u}^h)_n^+ - (\mathbf{u}^h)_n^- \right) d\Omega - \int_{(P_n)_h} \mathbf{e}_i \cdot \mathbf{h}^h dP = 0. \tag{4.22}
\end{aligned}$$

We remind that

$$\begin{aligned} \int_{Q_n} \mathbf{e}_i \cdot \rho \nabla \cdot (\mathbf{u}^h \mathbf{u}^h) \, dQ &= \int_{(P_n)_h} (\mathbf{e}_i \cdot \rho \mathbf{u}^h) \left(\mathbf{n} \cdot (\mathbf{u}^h - \mathbf{v}^h) \right) \, dP \\ &\quad - \int_{Q_n} \nabla \mathbf{e}_i : \rho (\mathbf{u}^h \mathbf{u}^h) \, dQ. \end{aligned} \quad (4.23)$$

Thus, we achieve:

$$\begin{aligned} &\int_{Q_n} \mathbf{e}_i \cdot \rho \left(\frac{\partial \mathbf{u}^h}{\partial t} - \mathbf{f}^h \right) \, dQ + \int_{(P_n)_h} (\mathbf{e}_i \cdot \rho \mathbf{u}^h) \left(\mathbf{n} \cdot (\mathbf{u}^h - \mathbf{v}^h) \right) \, dP \\ &+ \int_{\Omega_n} \mathbf{e}_i \cdot \rho \left((\mathbf{u}^h)_n^+ - (\mathbf{u}^h)_n^- \right) \, d\Omega - \int_{(P_n)_h} \mathbf{e}_i \cdot \mathbf{h}^h \, dP = 0. \end{aligned} \quad (4.24)$$

Remark 1

Equation (4.24) shows that the conservative form of the ST-VMS formulation in the NRF globally conserves the linear momentum.

Remark 2

Equation (4.24) can also be obtained, in the IRF, using the weighting functions $q^h \leftarrow 0$ and $\mathbf{w}^h \leftarrow \mathbf{e}_i$ in Eq. (3.10). This means that the conservative form of the ST-VMS formulation in the IRF globally conserves the linear momentum.

Nonconservative version

In the nonconservative form of the ST-VMS formulation, we obtain two additional terms when we use $q^h \leftarrow 0$. Considering this, we replace the test functions with $q^h \leftarrow \rho \mathbf{u}^h \cdot \mathbf{e}_i$ instead of zero (see also [26]) and $\mathbf{w}^h \leftarrow \mathbf{e}_i$ in Eq. (4.19), and write as

follows:

$$\begin{aligned}
& \int_{Q_n} \mathbf{e}_i \cdot \rho \left(\frac{\partial \mathbf{u}^h}{\partial t} + \mathbf{u}^h \cdot \nabla \mathbf{u}^h - \mathbf{f}^h \right) dQ \\
& + \int_{Q_n} \boldsymbol{\varepsilon}(\mathbf{e}_i) : \boldsymbol{\sigma}^h dQ - \int_{(P_n)_h} \mathbf{e}_i \cdot \mathbf{h}^h dP \\
& + \int_{Q_n} (\rho \mathbf{u}^h \cdot \mathbf{e}_i) \nabla \cdot \mathbf{u}^h dQ + \int_{\Omega_n} \mathbf{e}_i \cdot \rho \left((\mathbf{u}^h)_n^+ - (\mathbf{u}^h)_n^- \right) d\Omega \\
& + \int_{Q_n} \frac{\tau_{\text{SUPS}}}{\rho} \left(\rho \left(\frac{\partial \mathbf{e}_i}{\partial t} + (\mathbf{u}^h - \boldsymbol{\omega} \times \mathbf{r}^h) \cdot \nabla \mathbf{e}_i \right) + \nabla (\rho \mathbf{u}^h \cdot \mathbf{e}_i) \right) \cdot \mathbf{r}_M^h dQ \\
& + \int_{Q_n} \nu_{\text{LSIC}} \nabla \cdot \mathbf{e}_i \rho r_C^h dQ \\
& - \int_{Q_n} \tau_{\text{SUPS}} \mathbf{e}_i \cdot \left(\mathbf{r}_M^h \cdot \nabla (\mathbf{u}^h - \boldsymbol{\omega} \times \mathbf{r}^h) \right) dQ \\
& - \int_{Q_n} \frac{\tau_{\text{SUPS}}^2}{\rho} \mathbf{r}_M^h \cdot (\nabla \mathbf{e}_i) \cdot \mathbf{r}_M^h dQ = 0. \tag{4.25}
\end{aligned}$$

This formulation can be arranged with $\frac{\partial \mathbf{e}_i}{\partial t} = 0$, $\nabla \mathbf{e}_i = \mathbf{0}$ and $\boldsymbol{\varepsilon}(\mathbf{e}_i) = \mathbf{0}$, as follows:

$$\begin{aligned}
& \int_{Q_n} \mathbf{e}_i \cdot \rho \left(\frac{\partial \mathbf{u}^h}{\partial t} + \mathbf{u}^h \cdot \nabla \mathbf{u}^h - \mathbf{f}^h \right) dQ - \int_{(P_n)_h} \mathbf{e}_i \cdot \mathbf{h}^h dP \\
& + \int_{Q_n} (\rho \mathbf{u}^h \cdot \mathbf{e}_i) \nabla \cdot \mathbf{u}^h dQ + \int_{\Omega_n} \mathbf{e}_i \cdot \rho \left((\mathbf{u}^h)_n^+ - (\mathbf{u}^h)_n^- \right) d\Omega \\
& + \int_{Q_n} \frac{\tau_{\text{SUPS}}}{\rho} \left(\nabla (\rho \mathbf{u}^h \cdot \mathbf{e}_i) \right) \cdot \mathbf{r}_M^h dQ \\
& - \int_{Q_n} \tau_{\text{SUPS}} \mathbf{e}_i \cdot \left(\mathbf{r}_M^h \cdot \nabla \mathbf{u}^h \right) dQ + \int_{Q_n} \tau_{\text{SUPS}} \mathbf{e}_i \cdot \left(\mathbf{r}_M^h \cdot \nabla (\boldsymbol{\omega} \times \mathbf{r}^h) \right) dQ = 0. \tag{4.26}
\end{aligned}$$

We can arrange the mass balance part of Eq. (4.26) as:

$$\begin{aligned}
& \int_{Q_n} \frac{\tau_{\text{SUPS}}}{\rho} \nabla (\rho \mathbf{u}^h \cdot \mathbf{e}_i) \cdot \mathbf{r}_M^h dQ + \int_{Q_n} (\rho \mathbf{u}^h \cdot \mathbf{e}_i) \nabla \cdot \mathbf{u}^h dQ \\
& = \int_{Q_n} \tau_{\text{SUPS}} \mathbf{e}_i \cdot \left(\mathbf{r}_M^h \cdot \nabla \mathbf{u}^h \right) dQ + \int_{Q_n} \mathbf{e}_i \cdot \rho \left(\nabla \cdot \mathbf{u}^h \right) \mathbf{u}^h dQ, \tag{4.27}
\end{aligned}$$

and the following is obtained from the advective part:

$$\begin{aligned} \int_{Q_n} \mathbf{e}_i \cdot \rho \left(\mathbf{u}^h \cdot \nabla \mathbf{u}^h \right) dQ &= \int_{(P_n)_h} \left(\mathbf{e}_i \cdot \rho \mathbf{u}^h \right) \left(\mathbf{n} \cdot \left(\mathbf{u}^h - \mathbf{v}^h \right) \right) dP \\ &\quad - \int_{Q_n} \mathbf{e}_i \cdot \rho \left(\nabla \cdot \mathbf{u}^h \right) \mathbf{u}^h dQ. \end{aligned} \quad (4.28)$$

The first term in the right side of Eq. (4.27) is equal with opposite sign to the penultimate term of Eq. (4.26). The last terms of Eqs. (4.27) and (4.28) removes each other. Hence, we can write:

$$\begin{aligned} &\int_{Q_n} \mathbf{e}_i \cdot \rho \left(\frac{\partial \mathbf{u}^h}{\partial t} - \mathbf{f}^h \right) dQ + \int_{(P_n)_h} \left(\mathbf{e}_i \cdot \rho \mathbf{u}^h \right) \left(\mathbf{n} \cdot \left(\mathbf{u}^h - \mathbf{v}^h \right) \right) dP \\ &+ \int_{\Omega_n} \mathbf{e}_i \cdot \rho \left(\left(\mathbf{u}^h \right)_n^+ - \left(\mathbf{u}^h \right)_n^- \right) d\Omega - \int_{(P_n)_h} \mathbf{e}_i \cdot \mathbf{h}^h dP \\ &= - \int_{Q_n} \tau_{\text{SUPS}} \mathbf{e}_i \cdot \left(\mathbf{r}_M^h \cdot \varepsilon_{ijk} \omega_i \mathbf{e}_j \mathbf{e}_k \right) dQ. \end{aligned} \quad (4.29)$$

Remark 3

Equation (4.29) shows that the nonconservative form of the ST-VMS formulation in the NRF does not conserve the linear momentum globally.

Using the test functions $q^h \leftarrow \rho \mathbf{u}^h \cdot \mathbf{e}_i$ and $\mathbf{w}^h \leftarrow \mathbf{e}_i$, in the nonconservative form of the ST-VMS formulation in the IRF, given in Eq. (3.17), with Eqs. (4.27) and (4.28), we can write:

$$\begin{aligned} &\int_{Q_n} \mathbf{e}_i \cdot \rho \left(\frac{\partial \mathbf{u}^h}{\partial t} - \mathbf{f}^h \right) dQ + \int_{(P_n)_h} \left(\mathbf{e}_i \cdot \rho \mathbf{u}^h \right) \left(\mathbf{n} \cdot \left(\mathbf{u}^h - \mathbf{v}^h \right) \right) dP \\ &+ \int_{\Omega_n} \mathbf{e}_i \cdot \rho \left(\left(\mathbf{u}^h \right)_n^+ - \left(\mathbf{u}^h \right)_n^- \right) d\Omega - \int_{(P_n)_h} \mathbf{e}_i \cdot \mathbf{h}^h dP = 0. \end{aligned} \quad (4.30)$$

Remark 4

Equation (4.30) shows that the nonconservative form of the ST-VMS formulation

in the IRF globally conserves the linear momentum.

4.3.3 Global conservation of angular momentum

Conservative version

For angular momentum conservation, we need to take the position vector \mathbf{r}^h into account. We can also test the formulation just by taking cross product of the i th Cartesian basis vector with the position vector, since the position vector is also in the same discrete space. Writing $q^h \leftarrow 0$ and $\mathbf{w}^h \leftarrow \mathbf{e}_i \times \mathbf{r}^h$ as the test functions in Eq. (4.18) we obtain:

$$\begin{aligned}
& \int_{Q_n} \left(\mathbf{e}_i \times \mathbf{r}^h \right) \cdot \rho \left(\frac{\partial \mathbf{u}^h}{\partial t} + \nabla \left(\mathbf{u}^h \mathbf{u}^h \right) - \mathbf{f}^h \right) dQ \\
& + \int_{Q_n} \boldsymbol{\varepsilon} \left(\left(\mathbf{e}_i \times \mathbf{r}^h \right) \right) : \boldsymbol{\sigma}^h dQ - \int_{(P_n)_h} \left(\mathbf{e}_i \times \mathbf{r}^h \right) \cdot \mathbf{h}^h dP \\
& + \int_{\Omega_n} \left(\mathbf{e}_i \times \mathbf{r}^h \right) \cdot \rho \left(\left(\mathbf{u}^h \right)_n^+ - \left(\mathbf{u}^h \right)_n^- \right) d\Omega \\
& + \int_{Q_n} \frac{\tau_{\text{SUPS}}}{\rho} \left(\rho \left(\frac{\partial \left(\mathbf{e}_i \times \mathbf{r}^h \right)}{\partial t} + \left(\mathbf{u}^h - \boldsymbol{\omega} \times \mathbf{r}^h \right) \cdot \nabla \left(\mathbf{e}_i \times \mathbf{r}^h \right) \right) \right) \cdot \mathbf{r}_M^h dQ \\
& + \int_{Q_n} \nu_{\text{LSIC}} \nabla \cdot \left(\mathbf{e}_i \times \mathbf{r}^h \right) \rho r_C^h dQ \\
& + \int_{Q_n} \tau_{\text{SUPS}} \mathbf{r}_M^h \cdot \left(\nabla \left(\mathbf{e}_i \times \mathbf{r}^h \right) \right) \cdot \left(\mathbf{u}^h - \boldsymbol{\omega} \times \mathbf{r}^h \right) dQ \\
& - \int_{Q_n} \frac{\tau_{\text{SUPS}}^2}{\rho} \mathbf{r}_M^h \cdot \left(\nabla \left(\mathbf{e}_i \times \mathbf{r}^h \right) \right) \cdot \mathbf{r}_M^h dQ = 0. \tag{4.31}
\end{aligned}$$

Here, the test function of $\mathbf{e}_i \times \mathbf{r}^h$ is written as follows:

$$\mathbf{e}_i \times \mathbf{r}^h = \varepsilon_{ijk} r_j^h \mathbf{e}_k, \tag{4.32}$$

where $\varepsilon_{ijk} = (\mathbf{e}_i \times \mathbf{e}_j) \cdot \mathbf{e}_k$ is the Levi–Civita symbol, which is 1 if (i, j, k) is a cyclic shift of $(1, 2, 3)$, -1 if (i, j, k) is a cyclic shift of $(3, 2, 1)$, and 0 otherwise. Taking the gradient of the test function, we obtain:

$$\begin{aligned}
\nabla \left(\varepsilon_{ijk} r_j^h \mathbf{e}_k \right) &= \frac{\partial \left(\varepsilon_{ijk} r_j^h \right)}{\partial \mathbf{x}} \mathbf{e}_k \\
&= \frac{\partial \left(\varepsilon_{ijk} r_j^h \right)}{\partial x_l} \mathbf{e}_l \mathbf{e}_k \\
&= \varepsilon_{ijk} \delta_{jl} \mathbf{e}_l \mathbf{e}_k \\
&= \varepsilon_{ijk} \mathbf{e}_j \mathbf{e}_k,
\end{aligned} \tag{4.33}$$

which results out a skew-symmetric tensor. Here, $\delta_{jl} = \mathbf{e}_j \cdot \mathbf{e}_l$, and $\boldsymbol{\varepsilon}(\varepsilon_{ijk} r_j^h \mathbf{e}_k) = \mathbf{0}$ because of that:

$$\begin{aligned}
\boldsymbol{\varepsilon}(\varepsilon_{ijk} r_j^h \mathbf{e}_k) &= \frac{1}{2} \left(\nabla \left(\varepsilon_{ijk} r_j^h \mathbf{e}_k \right) + \left(\nabla \varepsilon_{ijk} r_j^h \mathbf{e}_k \right)^\top \right) \\
&= \frac{1}{2} \left(\varepsilon_{ijk} \mathbf{e}_j \mathbf{e}_k + \left(\varepsilon_{ijk} \mathbf{e}_j \mathbf{e}_k \right)^\top \right) \\
&= \frac{1}{2} \left(\varepsilon_{ijk} \mathbf{e}_j \mathbf{e}_k - \varepsilon_{ijk} \mathbf{e}_j \mathbf{e}_k \right) = \mathbf{0}.
\end{aligned} \tag{4.34}$$

The conservative form of the advective term can be written as:

$$\begin{aligned}
&\int_{Q_n} \left(\mathbf{e}_i \times \mathbf{r}^h \right) \cdot \rho \left(\nabla \cdot \left(\mathbf{u}^h \mathbf{u}^h \right) \right) dQ \\
&= \int_{(P_n)_h} \left(\left(\mathbf{e}_i \times \mathbf{r}^h \right) \cdot \rho \mathbf{u}^h \right) \left(\mathbf{n} \cdot \left(\mathbf{u}^h - \mathbf{v}^h \right) \right) dP - \int_{Q_n} \nabla \left(\mathbf{e}_i \times \mathbf{r}^h \right) : \rho \left(\mathbf{u}^h \mathbf{u}^h \right) dQ.
\end{aligned} \tag{4.35}$$

Addition of the last four terms of Eq. (4.31) and the last term of Eq. (4.35) is zero since it is a symmetric tensor, which is orthogonal to the gradient of the test function as given in Eq. (4.33). Considering this and using Eqs. (4.32)–(4.35) in Eq. (4.31),

the following is obtained:

$$\begin{aligned}
& \int_{Q_n} \mathbf{e}_i \cdot \rho \left(\frac{\partial}{\partial t} (\mathbf{r}^h \times \mathbf{u}^h) - \mathbf{r}^h \times \mathbf{f}^h \right) dQ \\
& + \int_{(P_n)_h} \left(\mathbf{e}_i \cdot \rho (\mathbf{r}^h \times \mathbf{u}^h) \right) \left(\mathbf{n} \cdot (\mathbf{u}^h - \mathbf{v}^h) \right) dP \\
& + \int_{\Omega_n} \mathbf{e}_i \cdot \rho \left((\mathbf{r}^h \times \mathbf{u}^h)_n^+ - (\mathbf{r}^h \times \mathbf{u}^h)_n^- \right) d\Omega \\
& - \int_{(P_n)_h} \mathbf{e}_i \cdot (\mathbf{r}^h \times \mathbf{h}^h) dP = 0.
\end{aligned} \tag{4.36}$$

Remark 5

Equation (4.36) shows that the conservative form of the ST-VMS formulation in the NRF globally conserves the angular momentum.

Remark 6

Equation (4.36) can also be obtained, in the IRF, using the weighting functions $q^h \leftarrow 0$ and $\mathbf{w}^h \leftarrow \mathbf{e}_i \times \mathbf{r}^h$ in Eq. (3.10). This means that the conservative form of the ST-VMS formulation in the IRF globally conserves the angular momentum.

Nonconservative version

In the nonconservative form of the ST-VMS formulation, we obtain some additional terms when we use $q^h \leftarrow 0$. Considering this, we replace the test functions with $q^h \leftarrow \rho \mathbf{u}^h \cdot (\mathbf{e}_i \times \mathbf{r}^h)$ instead of zero (see also [26]) and $\mathbf{w}^h \leftarrow (\mathbf{e}_i \times \mathbf{r}^h)$ in Eq. (4.19),

and write as follows:

$$\begin{aligned}
& \int_{Q_n} \left(\mathbf{e}_i \times \mathbf{r}^h \right) \cdot \rho \left(\frac{\partial \mathbf{u}^h}{\partial t} + \mathbf{u}^h \cdot \nabla \mathbf{u}^h - \mathbf{f}^h \right) dQ \\
& + \int_{Q_n} \boldsymbol{\varepsilon} \left(\left(\mathbf{e}_i \times \mathbf{r}^h \right) \right) : \boldsymbol{\sigma}^h dQ - \int_{(P_n)_h} \left(\mathbf{e}_i \times \mathbf{r}^h \right) \cdot \mathbf{h}^h dP \\
& + \int_{Q_n} \left(\rho \mathbf{u}^h \cdot \left(\mathbf{e}_i \times \mathbf{r}^h \right) \right) \nabla \cdot \mathbf{u}^h dQ + \int_{\Omega_n} \left(\mathbf{e}_i \times \mathbf{r}^h \right) \cdot \rho \left(\left(\mathbf{u}^h \right)_n^+ - \left(\mathbf{u}^h \right)_n^- \right) d\Omega \\
& + \int_{Q_n} \frac{\tau_{\text{SUPS}}}{\rho} \left(\rho \left(\frac{\partial \left(\mathbf{e}_i \times \mathbf{r}^h \right)}{\partial t} + \mathbf{u}^h \cdot \nabla \left(\mathbf{e}_i \times \mathbf{r}^h \right) \right) + \nabla \left(\rho \mathbf{u}^h \cdot \left(\mathbf{e}_i \times \mathbf{r}^h \right) \right) \right) \cdot \mathbf{r}_M^h dQ \\
& - \int_{Q_n} \tau_{\text{SUPS}} \left(\boldsymbol{\omega} \times \mathbf{r}^h \right) \cdot \nabla \left(\mathbf{e}_i \times \mathbf{r}^h \right) \cdot \mathbf{r}_M^h dQ + \int_{Q_n} \nu_{\text{LSIC}} \nabla \cdot \left(\mathbf{e}_i \times \mathbf{r}^h \right) \rho r_C^h dQ \\
& - \int_{Q_n} \tau_{\text{SUPS}} \left(\mathbf{e}_i \times \mathbf{r}^h \right) \cdot \left(\mathbf{r}_M^h \cdot \nabla \mathbf{u}^h \right) dQ \\
& + \int_{Q_n} \tau_{\text{SUPS}} \left(\mathbf{e}_i \times \mathbf{r}^h \right) \cdot \left(\mathbf{r}_M^h \cdot \nabla \left(\boldsymbol{\omega} \times \mathbf{r}^h \right) \right) dQ \\
& - \int_{Q_n} \frac{\tau_{\text{SUPS}}^2}{\rho} \mathbf{r}_M^h \cdot \left(\nabla \left(\mathbf{e}_i \times \mathbf{r}^h \right) \right) \cdot \mathbf{r}_M^h dQ = 0. \tag{4.37}
\end{aligned}$$

Arranging the mass balance part, as follows:

$$\begin{aligned}
& \int_{Q_n} \frac{\tau_{\text{SUPS}}}{\rho} \nabla q^h \cdot \mathbf{r}_M^h dQ + \int_{Q_n} q^h \nabla \cdot \mathbf{u}^h dQ \\
& = \int_{Q_n} \tau_{\text{SUPS}} \left(\mathbf{e}_i \times \mathbf{r}^h \right) \cdot \left(\mathbf{r}_M^h \cdot \nabla \mathbf{u}^h \right) dQ + \int_{Q_n} \left(\mathbf{e}_i \times \mathbf{r}^h \right) \cdot \rho \left(\nabla \cdot \mathbf{u}^h \right) \mathbf{u}^h dQ, \tag{4.38}
\end{aligned}$$

and from the advective term:

$$\begin{aligned}
\int_{Q_n} \left(\mathbf{e}_i \times \mathbf{r}^h \right) \cdot \rho \left(\mathbf{u}^h \cdot \nabla \mathbf{u}^h \right) dQ & = \int_{(P_n)_h} \left(\left(\mathbf{e}_i \times \mathbf{r}^h \right) \cdot \rho \mathbf{u}^h \right) \left(\mathbf{n} \cdot \left(\mathbf{u}^h - \mathbf{v}^h \right) \right) dP \\
& - \int_{Q_n} \left(\mathbf{e}_i \times \mathbf{r}^h \right) \cdot \rho \left(\nabla \cdot \mathbf{u}^h \right) \mathbf{u}^h dQ, \tag{4.39}
\end{aligned}$$

are acquired. The first term of Eq. (4.38) removes the ninth term of Eq. (4.37).

The last terms of Eqs. (4.38) and (4.39) equal with opposite signs. The last term of Eq. (4.37) is zero because of the orthogonality of the skew-symmetric tensor (see

Eq. (4.33)) to a symmetric tensor. Using all these and Eq. (4.34), from Eq. (4.37) we achieve:

$$\begin{aligned}
& \int_{Q_n} \mathbf{e}_i \cdot \rho \left(\frac{\partial}{\partial t} (\mathbf{r}^h \times \mathbf{u}^h) - \mathbf{r}^h \times \mathbf{f}^h \right) dQ \\
& + \int_{(P_n)_h} \left(\mathbf{e}_i \cdot \rho (\mathbf{r}^h \times \mathbf{u}^h) \right) \left(\mathbf{n} \cdot (\mathbf{u}^h - \mathbf{v}^h) \right) dP \\
& + \int_{\Omega_n} \mathbf{e}_i \cdot \rho \left((\mathbf{r}^h \times \mathbf{u}^h)_n^+ - (\mathbf{r}^h \times \mathbf{u}^h)_n^- \right) d\Omega - \int_{(P_n)_h} \mathbf{e}_i \cdot (\mathbf{r}^h \times \mathbf{h}^h) dP \\
& = - \int_{Q_n} \tau_{\text{SUPS}} \left((\mathbf{u}^h - \boldsymbol{\omega} \times \mathbf{r}^h) \cdot \varepsilon_{ijk} \mathbf{e}_j \mathbf{e}_k \right) \cdot \mathbf{r}_M^h dQ \\
& - \int_{Q_n} \tau_{\text{SUPS}} \varepsilon_{ijk} r_j \mathbf{e}_k \cdot \left(\mathbf{r}_M^h \cdot \varepsilon_{ijk} \omega_i \mathbf{e}_j \mathbf{e}_k \right) dQ. \tag{4.40}
\end{aligned}$$

Remark 7

Equation (4.40) shows that the nonconservative form of the ST-VMS formulation in the NRF does not conserve the angular momentum globally.

Using the weighting functions $q^h \leftarrow \rho (\mathbf{e}_i \times \mathbf{r}^h) \cdot \mathbf{u}^h$ and $\mathbf{w}^h \leftarrow \mathbf{e}_i \times \mathbf{r}^h$ in Eq. (3.17), with Eqs. (4.34), (4.38) and (4.39), the following is obtained:

$$\begin{aligned}
& \int_{Q_n} \mathbf{e}_i \cdot \rho \left(\frac{\partial}{\partial t} (\mathbf{r}^h \times \mathbf{u}^h) - \mathbf{r}^h \times \mathbf{f}^h \right) dQ \\
& + \int_{(P_n)_h} \left(\mathbf{e}_i \cdot \rho (\mathbf{r}^h \times \mathbf{u}^h) \right) \left(\mathbf{n} \cdot (\mathbf{u}^h - \mathbf{v}^h) \right) dP \\
& + \int_{\Omega_n} \mathbf{e}_i \cdot \rho \left((\mathbf{r}^h \times \mathbf{u}^h)_n^+ - (\mathbf{r}^h \times \mathbf{u}^h)_n^- \right) d\Omega - \int_{(P_n)_h} \mathbf{e}_i \cdot (\mathbf{r}^h \times \mathbf{h}^h) dP \\
& = - \int_{Q_n} \tau_{\text{SUPS}} \left(\mathbf{u}^h \cdot \varepsilon_{ijk} \mathbf{e}_j \mathbf{e}_k \right) \cdot \mathbf{r}_M^h dQ. \tag{4.41}
\end{aligned}$$

Remark 8

Equation (4.41) shows that the nonconservative form of the ST-VMS formulation in the IRF does not conserve the angular momentum globally.

Chapter 5

U-duct Turbulent-Flow Analysis

The U-duct turbulent-flow, which is a benchmark problem with an experimental study [82], is computed and represented in this chapter. The high curvature of the computational domain, the high Reynolds number of the flow and inflow profile dependence of flow are the computational challenges. To encounter these challenges, all computations in this chapter are performed on the computational domains represented by quadratic NURBS meshes, and using a fully-developed flow field on the inflow of the U-duct. The flow is developed in a straight duct with translational-periodicity condition applied with the ST-SI. The variation of results with the time-averaging range, mesh refinement, and the Courant number are investigated. We show how the ST-VMS with isogeometric discretization performs in this kind of a turbulent-flow computation comparing the results to experimental data [82].

5.1 Definitions for the data analysis

5.1.1 Scale separation

The velocity is scaled as

$$\mathbf{u} = \bar{\mathbf{u}} + \mathbf{u}'. \quad (5.1)$$

Here the “ $\bar{\cdot}$ ” denotes the averaging over the period $\mathcal{T} = (T_1, T_2)$. We note that this scale separation is different from that given in Eqs. (3.4)–(3.7) and it is only for

post-processing. The time-averaging is calculated as:

$$\bar{f} = \frac{1}{T_2 - T_1} \int_{T_1}^{T_2} f dt. \quad (5.2)$$

Here, f is any scalar or vector. This is extended to the ST context with

$$\bar{\bar{f}} = \frac{1}{\int_{\mathcal{T}} \int_{\Omega_t} d\Omega dt} \int_{\mathcal{T}} \int_{\Omega_t} f d\Omega dt \quad (5.3)$$

$$= \frac{1}{\int_Q dQ} \int_Q f dQ, \quad (5.4)$$

where $Q = \{ \mathbf{x}(t) \in \Omega_t \mid t \in \mathcal{T} \}$.

The L_q is norm of a scalar which is defined as:

$$\|f\|_{q,\mathcal{T}} = \left(\frac{1}{T_2 - T_1} \int_{T_1}^{T_2} |f|^q dt \right)^{\frac{1}{q}}, \quad (5.5)$$

and this is extended to the ST context with

$$\|f\|_{q,Q} = \left(\frac{1}{\int_{\mathcal{T}} \int_{\Omega_t} d\Omega dt} \int_{\mathcal{T}} \int_{\Omega_t} |f|^q d\Omega dt \right)^{\frac{1}{q}} \quad (5.6)$$

$$= \left(\frac{1}{\int_Q dQ} \int_Q |f|^q dQ \right)^{\frac{1}{q}}. \quad (5.7)$$

5.1.2 Nondimensionalization

The scaled quantities are defined with ρ , U and D , that are the scales for the density, velocity and length,

$$\mathbf{u}^* = \frac{\mathbf{u}}{U}, \quad (5.8)$$

$$t^* = \frac{tU}{D}, \quad (5.9)$$

$$p^* = \frac{p}{\rho U^2}. \quad (5.10)$$

5.1.3 Wall-related scaling

The friction velocity u_τ is written as follows:

$$u_\tau = \sqrt{\frac{\|\mathbf{h}_v\|}{\rho}}. \quad (5.11)$$

Here, the wall shear stress is shown by \mathbf{h}_v . The streamwise component of the velocity is nondimensionalized around the wall as $u^+ = u_s/u_\tau$. The scaled wall-normal coordinate is written as:

$$y^+ = \frac{yu_\tau}{\nu}, \quad (5.12)$$

where y is the coordinate along the wall normal.

5.2 Straight duct with periodicity condition

5.2.1 Problem setup

The straight duct with $D \times D$ cross-sectional area and $5D$ length is the computational model used in this study. The cases with $\text{Re} = 4 \times 10^4$ and 10^5 are calculated. The Reynolds number is defined by $\text{Re} = \frac{UD}{\nu}$ with the streamwise velocity averaged in time and over the cross-section, U . \mathbf{e}_1 , \mathbf{e}_2 and \mathbf{e}_s in Figure 5.1 illustrates the basis vectors. The data analysis is performed expressing the velocity components as $u_k = \mathbf{u} \cdot \mathbf{e}_k$, where $k = 1, 2, s$.

5.2.2 Mesh

The mesh used for the computations with both $\text{Re} = 4 \times 10^4$ and 10^5 , is demonstrated in Figure 5.2. The uniform mesh in the streamwise direction is made of 72^3 quadratic NURBS elements. Corresponding to the cases with $\text{Re} = 4 \times 10^4$ and 10^5 , the normal-direction thickness for the first elements near the wall are $y^+ = 0.43$ and 0.95 . These

values are calculated based on Eqs. (5.12) and (5.11), using the estimation of wall shear stress $\|\mathbf{h}_v\|$ with the pipe friction factor f as given in [83],

$$\frac{1}{f^{0.5}} = 2 \log (\text{Re } f^{0.5}) - 0.8. \quad (5.13)$$

The friction factors for the $\text{Re} = 4 \times 10^4$ and 10^5 are $f = 2.2 \times 10^{-2}$ and 1.8×10^{-2} .

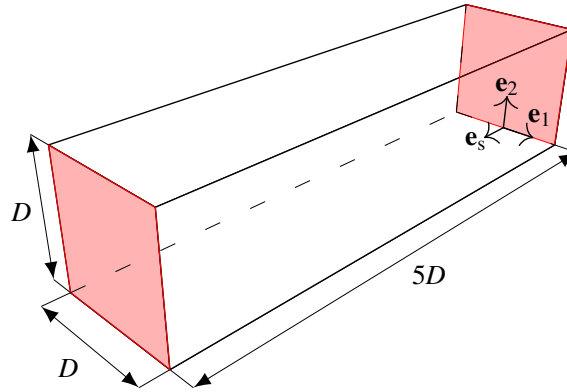


Figure 5.1: Straight duct geometry. The *red* planes show the boundaries where the periodicity condition is enforced. \mathbf{e}_s , \mathbf{e}_1 and \mathbf{e}_2 are the coordinate basis vectors in the streamwise and wall-normal directions. This figure was also shown in [1]

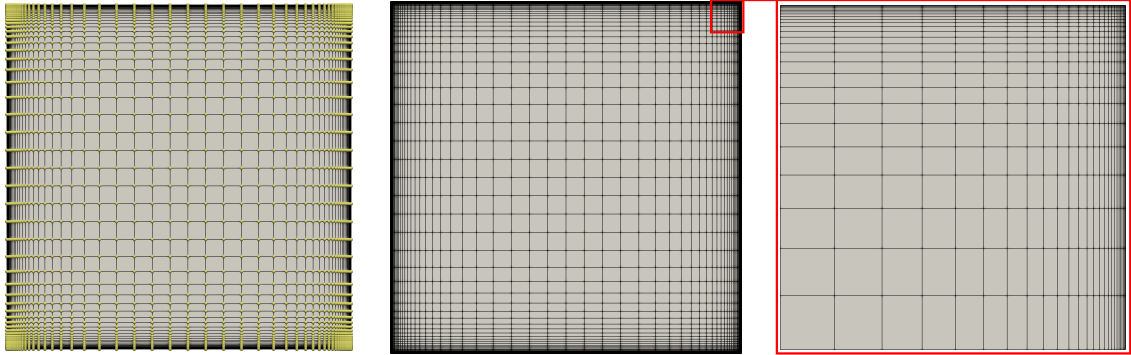


Figure 5.2: The control mesh (*left*) and the corresponding mesh (*middle*) with a close view of it (*right*). The control points are shown by the *yellow* points. This figure was also shown in [1]

5.2.3 Boundary conditions

The no-slip conditions enforced weakly are employed on the walls. In both cases, the pressure gradient specified along the model is arranged until the case Reynolds number is approached enough. That approximate Reynolds number becomes the actual value we compute.

5.2.4 Computational conditions

The ST-VMS formulation with the stabilization parameters given by Eqs. (A.1)–(A.3), (A.12) and (A.13) are computed. The Courant number is defined as $C_{\Delta t} = \frac{U\Delta t}{h_s}$, to determine the time-step size Δt . Here, h_s is the streamwise directional element length. The Courant number of $C_{\Delta t} = 0.322$ is set. 3 nonlinear iterations per time step and 500 GMRES iterations per nonlinear iteration are calculated. A period of flow is defined as $T = L/U$, where L is the length of the straight duct. $20T$ of the flow after achieving the actual Reynolds number is calculated in 4,474 time steps.

5.2.5 Results

The pressure difference specified across the SI is adjusted and the Reynolds number values of 3.96×10^4 and 9.98×10^4 are achieved at the normalized pressure gradient values of 5.6×10^{-2} and 4.7×10^{-2} , respectively. In neither cases the variation of the calculated Reynolds numbers from the expected ones are more than 1 %.

We compare \bar{u}_s and $\|u'_s\|_{2,Q}$ to the experimental data [82] in Figure 5.3, for $Re = 10^5$. In the experiment published in 1994 by Cheah et. al [82], the turbulent flow in a U-duct was investigated by the laser-Doppler anemometry (LDA) method. The streamwise directional time-averaged velocity profiles and the root-mean-square velocity fluctuations were some of the results reported on the center and a near-wall planes along the U-duct (see Figure 5.6). The flow profiles were provided at the inlet

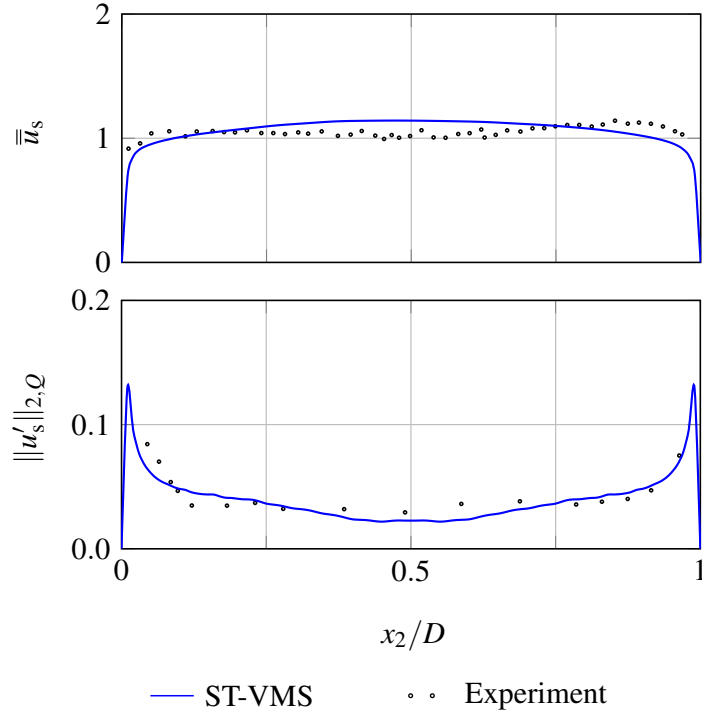


Figure 5.3: \bar{u}_s and $\|u'_s\|_{2,Q}$ at $\text{Re} = 10^5$. Velocity profiles are calculated in the straight duct with $Q = \left\{ \mathbf{x} = (0, x_2, x_s) \mid x_s \in (0, 5D), t \in (8.5T, 20T) \right\}$. The reference study is [82]. This figure was also shown in [1]

of the U-duct in the experimental study. However, for certainty, we use this fully-developed inflow profile, which also has a reasonable agreement with the experiment as shown in Figure 5.3. The ST-averaged streamwise velocity profiles near the wall, \bar{u}^+ , are shown Figure 5.4, for the flows at two different Reynolds numbers, which are i) 4×10^4 and ii) 10^5 . The reason is that we aim to evaluate our results with a reliable reference study at the closest-possible value to 10^5 , the Reynolds number used in the U-duct. In [84], Pirozzoli et. al reported detailed results of flow computations at four different Reynolds numbers. From this Direct Numerical Simulation (DNS) study, the flow at the Reynolds number of 4×10^4 is taken reference. This is the closest available data obtained in a square duct by DNS when our flow calculation is performed, according to our search and as mentioned in [85].

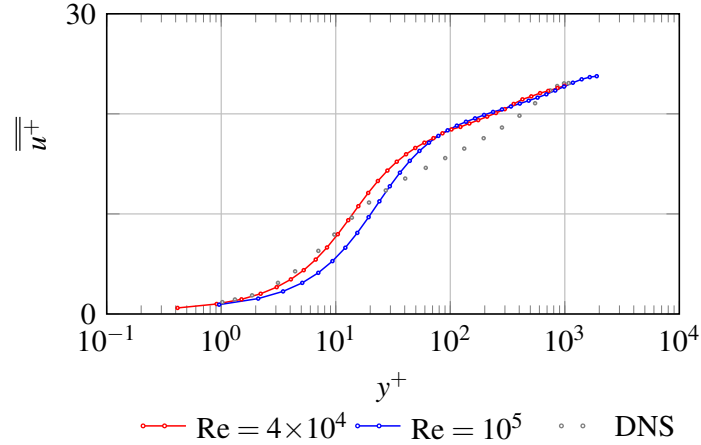


Figure 5.4: $\overline{u^+}$ at $\text{Re} = 4 \times 10^4$ and $\text{Re} = 10^5$. Velocity profiles are calculated in the straight duct with $Q = \left\{ \mathbf{x} = (0, x_2, x_s) \mid x_s \in (0, 5D), t \in (8.5T, 20T) \right\}$. The reference study is [84] at $\text{Re} = 4 \times 10^4$. This figure was also shown in [1]

5.3 U-duct

5.3.1 Problem setup

The geometry of the U-duct with the coordinate basis vectors are shown in Figure 5.5. The Reynolds number is $\text{Re} = 10^5$. The flow characteristics are reported along the model at several locations which are shown in Figure 5.6.

5.3.2 Boundary conditions

The fully-developed velocity profile is averaged in space and in time, $\overline{\mathbf{u}}$, and it is used as the inlet condition. The no-slip conditions enforced weakly are employed on the walls and the zero-stress condition is used at the outlet.

5.3.3 Mesh

The geometry is represented exactly using four patches of quadratic NURBS meshes. Figure 5.7 illustrates how we define the weights of the control points. Five different meshes named Mesh A, B, C, D and E are generated by a sequence of knot insertions.

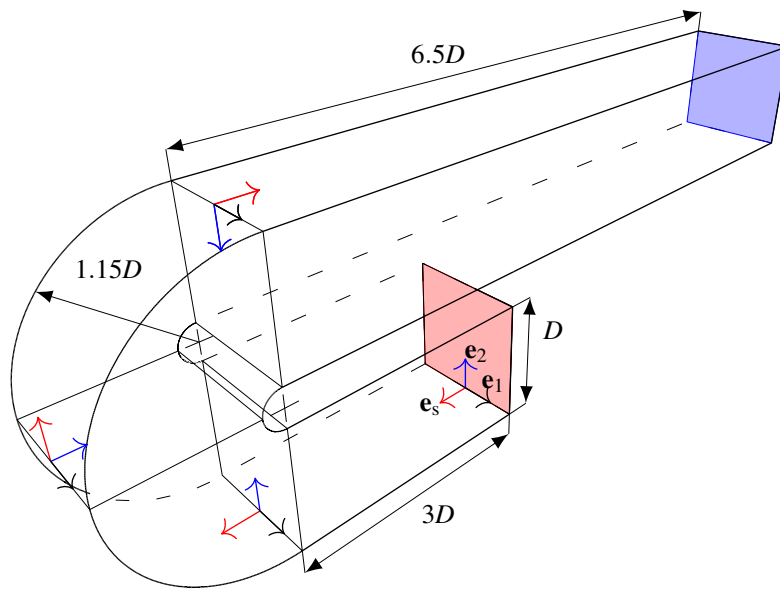


Figure 5.5: U-duct geometry. The *red* and *blue* planes show the inlet and outlet. \mathbf{e}_s , \mathbf{e}_1 and \mathbf{e}_2 are the coordinate basis vectors in the streamwise and wall-normal directions. This figure was also shown in [1]

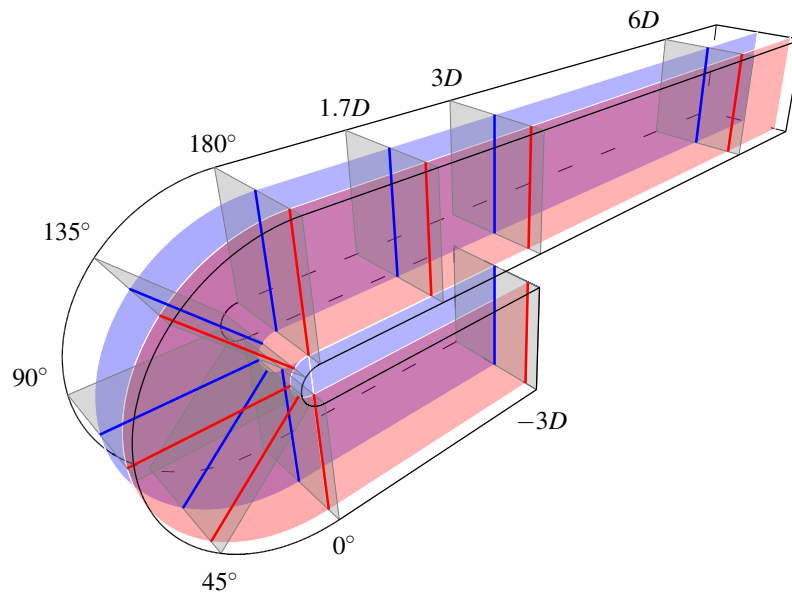


Figure 5.6: The locations where the flow characteristics are reported. The *red* plane is the near-wall ($x_1/D = 0.375$) and the *blue* plane is the center ($x_1 = 0$) planes. The flow field is generated and investigated along the model on the *red* and *blue* lines. This figure was also shown in [1]

Table 5.1: The mesh details. nc , ne and ne_b are the number of control points, quadratic NURBS elements in the whole model and along the bend. The $h_{s,\text{inlet}}$ and $h_{s,\text{min}}$ are the first and minimum element lengths in the streamwise direction which are located at the inlet and in the curvature

Mesh	nc	ne	ne_b	$h_{s,\text{inlet}}$	$h_{s,\text{min}}$	y^+
Mesh A	$20^2 \times 60$	$18^2 \times 55$	12	$2.77 \times 10^{-1} D$	$3.6 \times 10^{-2} D$	3.79
Mesh B	$38^2 \times 115$	$36^2 \times 110$	24	$1.39 \times 10^{-1} D$	$1.8 \times 10^{-2} D$	1.90
Mesh C	$56^2 \times 170$	$54^2 \times 165$	36	$0.93 \times 10^{-1} D$	$1.2 \times 10^{-2} D$	1.26
Mesh D	$74^2 \times 225$	$72^2 \times 220$	48	$0.69 \times 10^{-1} D$	$0.9 \times 10^{-2} D$	0.95
Mesh E	$74^2 \times 278$	$72^2 \times 273$	96	$0.69 \times 10^{-1} D$	$0.45 \times 10^{-2} D$	0.95

First, Mesh A is generated. Later Mesh B, C and D are obtained by 2, 3 and 4 times the number of elements of Mesh A. The Mesh E is obtained by twice number of elements in the curvature and additional 5 elements in both lower and upper straight parts. Additional elements of Mesh E are used to keep the maximum ratio between two adjacent elements lower than 2. The Mesh D and E have the same cross-section mesh as the straight-duct (see Section 5.2) has. All five meshes are illustrated in Figure 5.8, and the data for all five is given in Table 5.1.

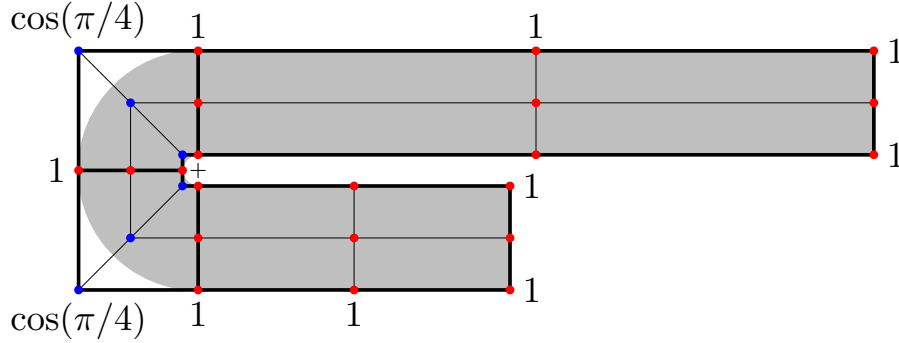


Figure 5.7: Exact arc representation by NURBS. The weight values of $\cos(\pi/4)$ and 1 are set on the *blue* and the *red* points. This figure was also shown in [1]

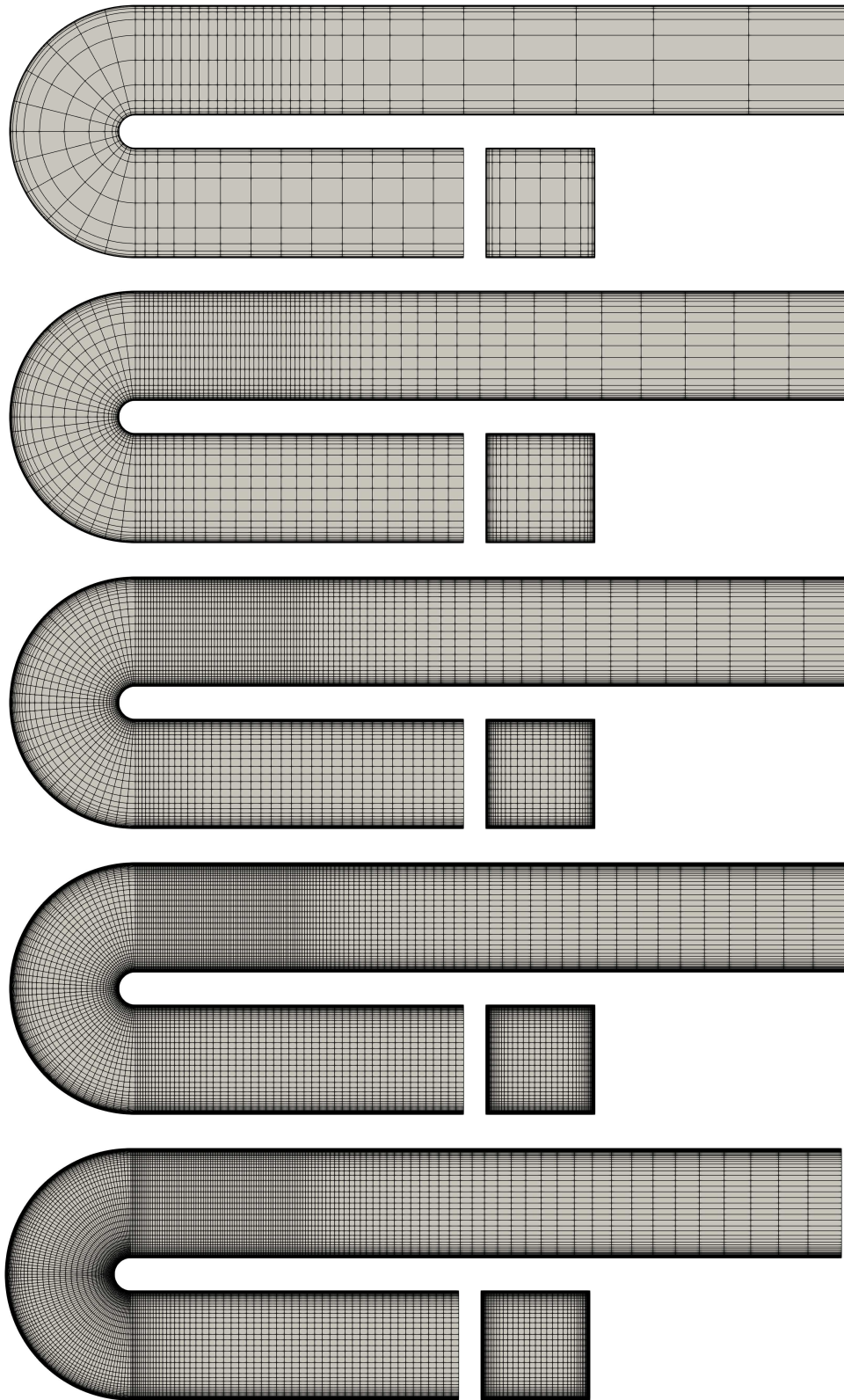


Figure 5.8: Mesh A, B, C, D and E on the U-duct. This figure was also shown in [1]

5.3.4 Computational conditions

The ST-VMS formulation with the stabilization parameters given by Eqs. (A.1)–(A.3), (A.12) and (A.13) are computed. The time-step size is decided from the Courant number that is based on the minimum element length in the streamwise direction (see Table 5.1). 3 nonlinear iterations per time step and 500 GMRES iterations per nonlinear iteration are calculated. A period of flow is defined as $T = L/U$, where $L = (3 + 0.65\pi + 6.5)D$ is the length of the U-duct.

5.3.5 Results

Sequence of computations The Mesh A is employed initially to compute the flow for $\mathcal{T} = (0, 40T)$. Later, data at $t = 29T$ is projected on Mesh B and used as initial condition for Mesh B computations. Having computed one T of the flow with Mesh B, the initial condition for Mesh C is obtained by least-squares projection at $t = 30T$. Following the same procedure, the initial conditions are obtained for Mesh D and E by least-squares projection, from Mesh C at $t = 31T$ and D at $t = 32T$.

Effect of the time-averaging range The flow development and effect of the time-averaging range is studied in this section using $C_{\Delta t} = 10$. Flow development is shown by the velocity and pressure distributions on the center plane along the model in Figure 5.9. It is generated in different time-averaging ranges all spanning $10T$. Significant differences are not observed for the time ranges after the flow is developed in the first $10T$. Figure 5.10 also represents the developing flow by Fourier decomposition of u_2 in various time ranges all for $10T$. The plots obtained from the time ranges beyond $\mathcal{T} = (0, 10T)$ fluctuate similarly. We investigated the time-averaging range effect on the results decomposing u_2 into the frequency domain in various time ranges in Figure 5.11. The lowest frequency of local maximum is observed around $0.67 T^{-1}$, and is covered by all the ranges shown in the legend.

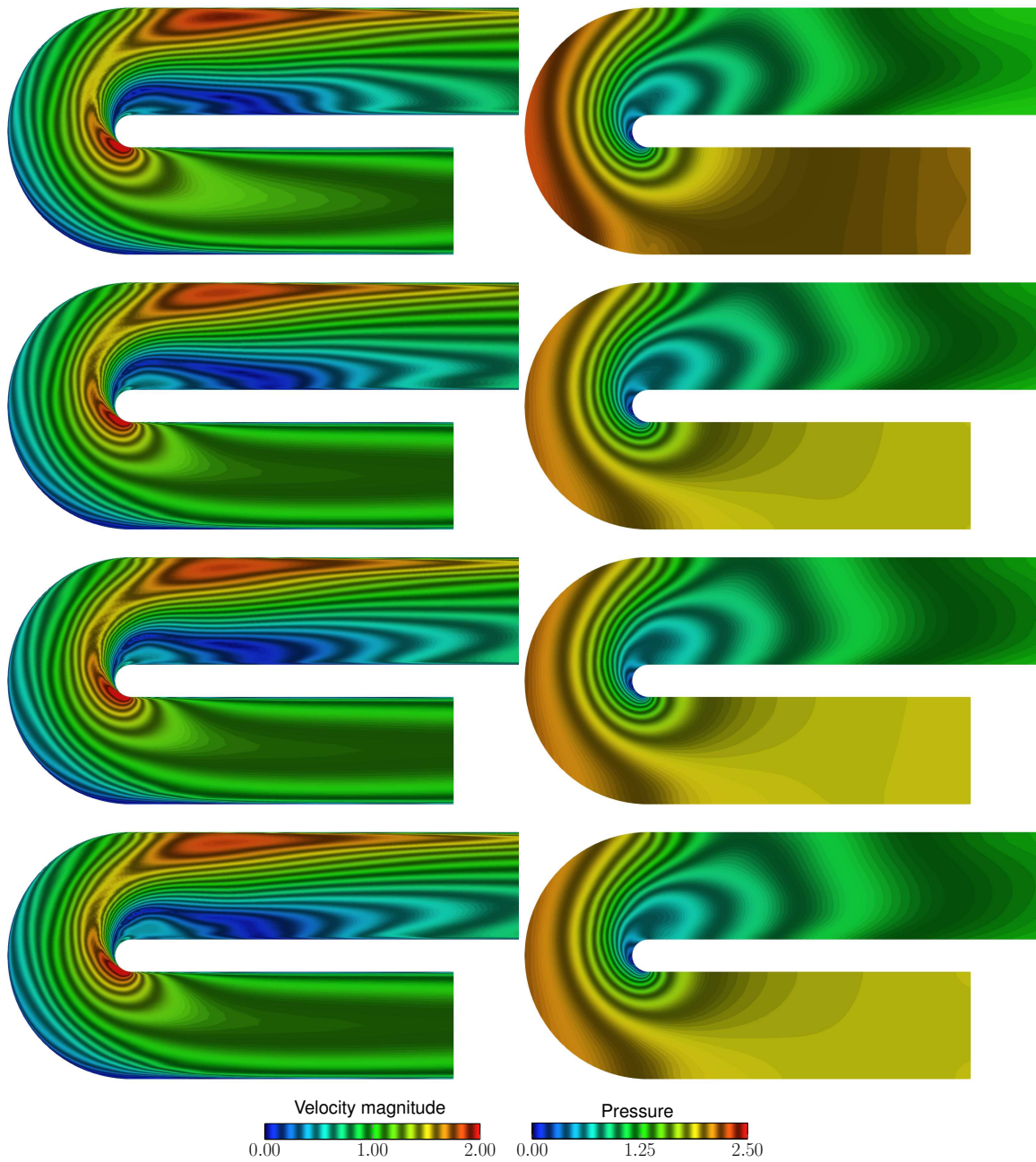


Figure 5.9: Flow development with the velocity magnitude ($\|\bar{\mathbf{u}}\|$) and pressure (\bar{p}) distributions along the U-duct on the center plane. The time-average is taken over $\mathcal{T} = (0, 10T)$, $(10T, 20T)$, $(20T, 30T)$, and $(30T, 40T)$ from *top* to *bottom*. This figure was also shown in [1]

This frequency value approximately corresponds to a period of $1.5T$. Accordingly, $3T$ is a long enough averaging period for taking the statistics of the flow field.

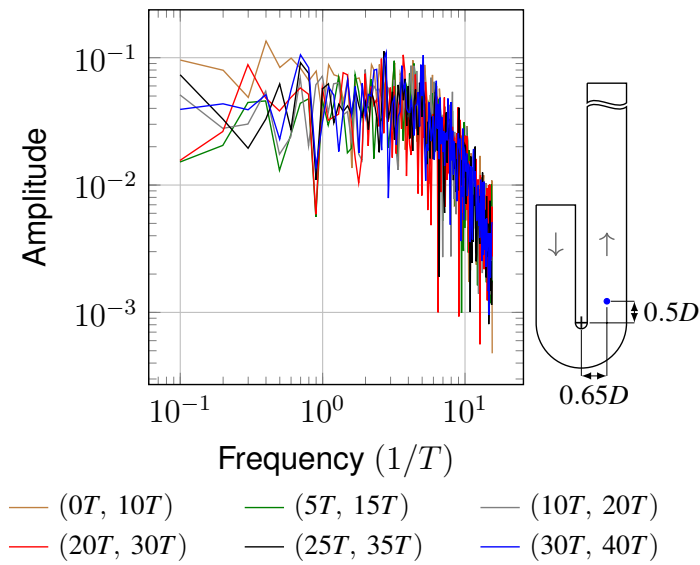


Figure 5.10: Effect of the flow development by Fourier transform of u_2 at the point shown in *blue* on the center plane. The time intervals that the transformation is performed are given in the legend. This figure was also shown in [1]

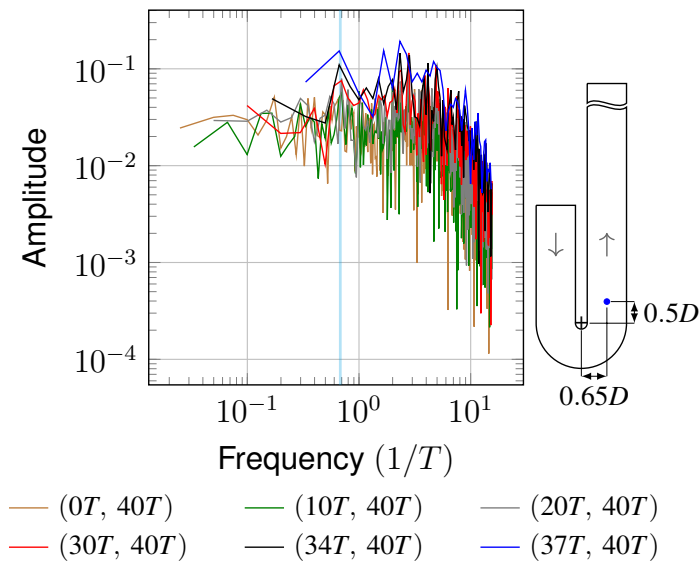


Figure 5.11: Effect of the averaging range by Fourier transform of u_2 at the point shown in *blue* on the center plane. The time intervals that the transformation is performed are given in the legend. The lowest frequency of local maximum is emphasized by the *cyan* line at $0.67T$. This figure was also shown in [1]

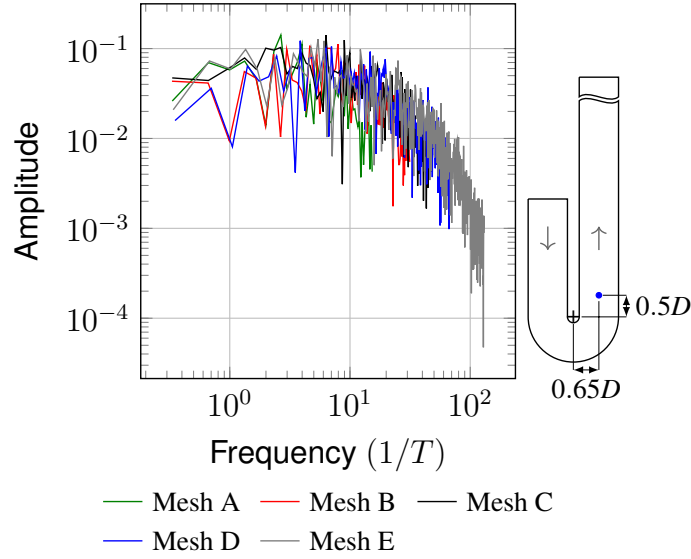


Figure 5.12: Effect of the mesh refinement by Fourier transform of u_2 at the point shown in *blue* on the center plane. The time range is $\mathcal{T} = (33T, 36T)$. This figure was also shown in [1]

Effect of the mesh refinement Data computed with five different meshes are compared in this study at $C_{\Delta t} = 10$. The u_2 is decomposed into the frequency domain by Fourier transform. It is shown in Figure 5.12 in the time range $\mathcal{T} = (33T, 36T)$. The results from Mesh A to E are in good agreement. The representation gets shorter at the higher end of the frequency as the coarser mesh is used. The streamwise directional velocity, \bar{u}_s on the center plane, along the U-duct is shown in Figure 5.13. Here the results are time-averaged over $\mathcal{T} = (33T, 36T)$, compared to the experimental data from [82]. The effect of mesh refinement is observed slightly between the results from Mesh A and the finer meshes up to Mesh D. A good agreement is observed in the results obtained with Mesh B, C and D, while those with Mesh E differ slightly around the curvature. A deeper investigation is given in Section 5.3.5 about the differences between the results obtained with Mesh D and E.

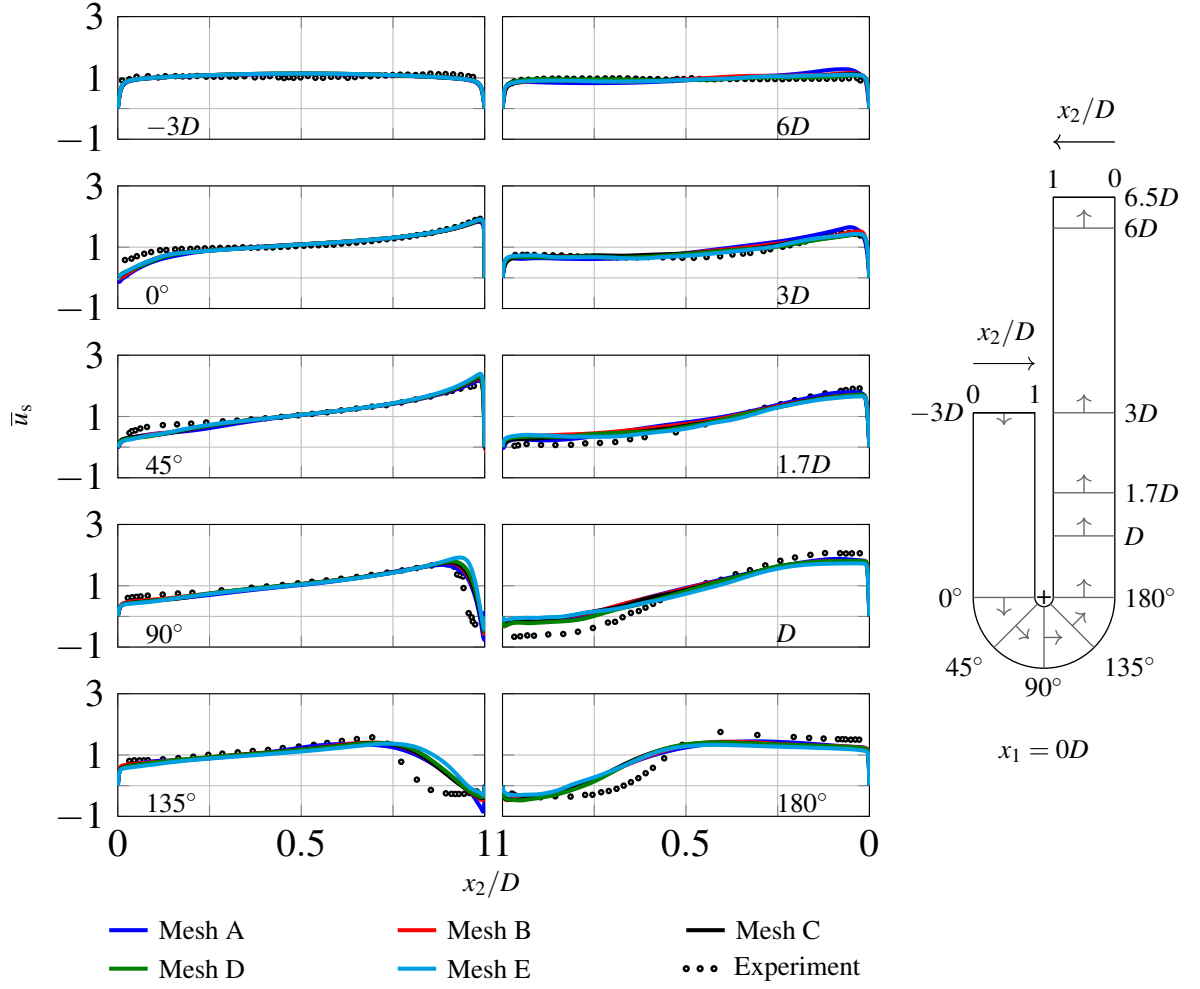


Figure 5.13: Effect of the mesh refinement on the streamwise velocity along the U-duct. \bar{u}_s is calculated on the center plane. Time-average is taken over $\mathcal{T} = (33T, 36T)$. The reference results are adapted from [82]. Numerical results are adapted from [1]

Effect of the Courant number The results computed with Mesh D and E are compared in this study at $C_{\Delta t} = 10, 5$ and 2.5 , in $\mathcal{T} = (33T, 36T)$. The isosurfaces corresponding to a positive value of the second invariant of $\nabla \bar{\mathbf{u}}$ colored by velocity magnitude are shown in Figure 5.14. Decreasing the Courant number, we do not observe a significant difference in the results with Mesh D. The flow separation and reverse flow region length is similar in the results with Mesh E at $C_{\Delta t} = 10$. However, with Mesh E at $C_{\Delta t} = 5$ and 2.5 , the flow separation occurs earlier and the length of

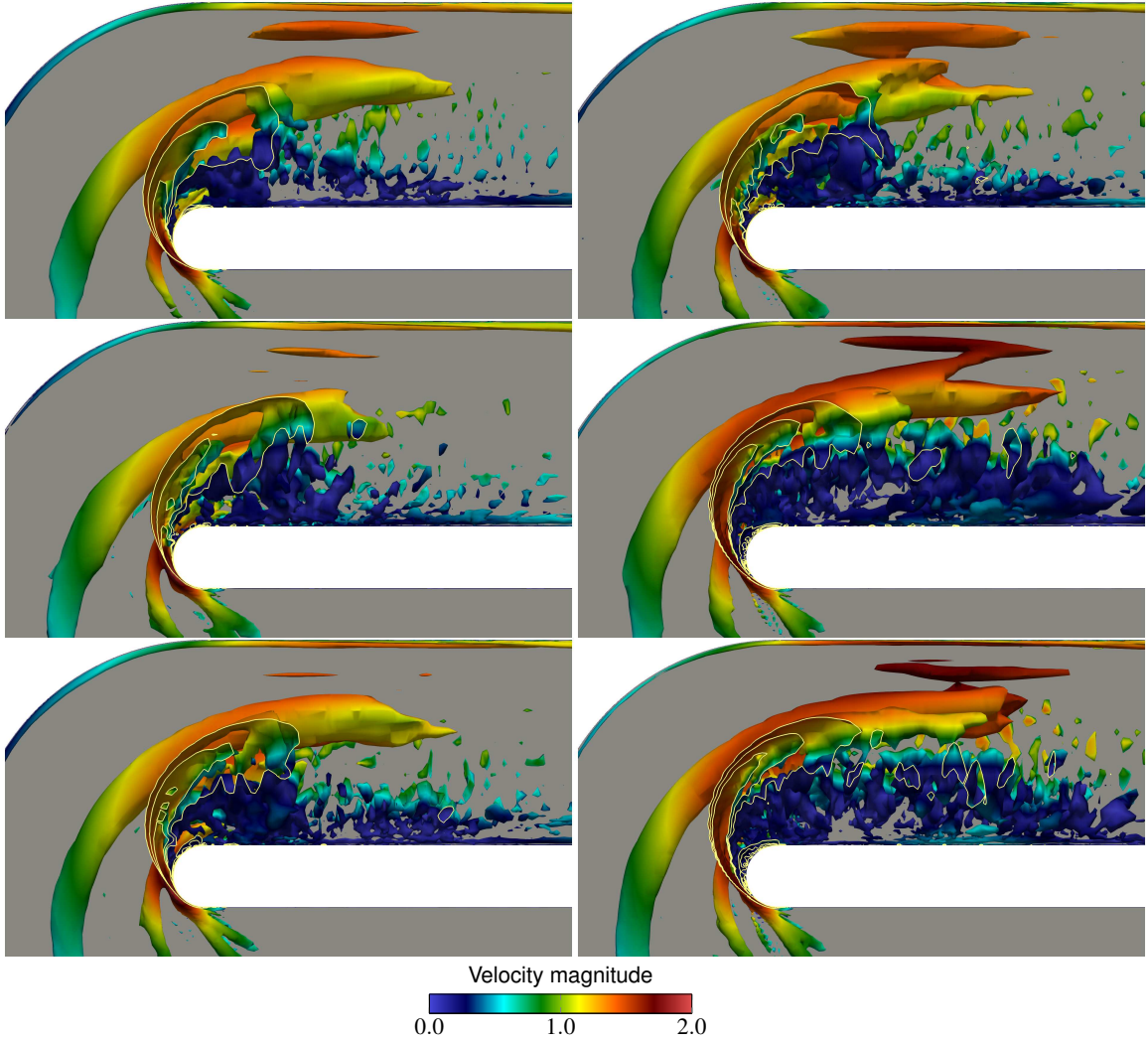


Figure 5.14: Effect of the Courant number by the isosurfaces corresponding to a positive value of the second invariant of $\nabla\bar{\mathbf{u}}$. Isosurfaces are colored by velocity magnitude ($\|\bar{\mathbf{u}}\|$). Time-average is taken over $\mathcal{T} = (33T, 36T)$. Results obtained using Mesh D and E are given on the *left* and *right*. $C_{\Delta t} = 10, 5$ and 2.5 from *top* to *bottom*. The intersection between the isosurfaces and the center plane is represented by the lines in *yellow*. This figure was also shown in [1]

reverse flow region becomes longer. This is observed more obviously in Figures 5.15 and 5.16 with \bar{u}_s . Figures show the flow field together with the experimental results of [82] on the center and near-wall planes. Figures 5.17 and 5.18 show $\|u'_s\|_{2,\mathcal{T}}$ on those planes. To conclude, the results calculated using Mesh E at $C_{\Delta t} = 5$ and 2.5 are in good agreement with the data from the experiment.

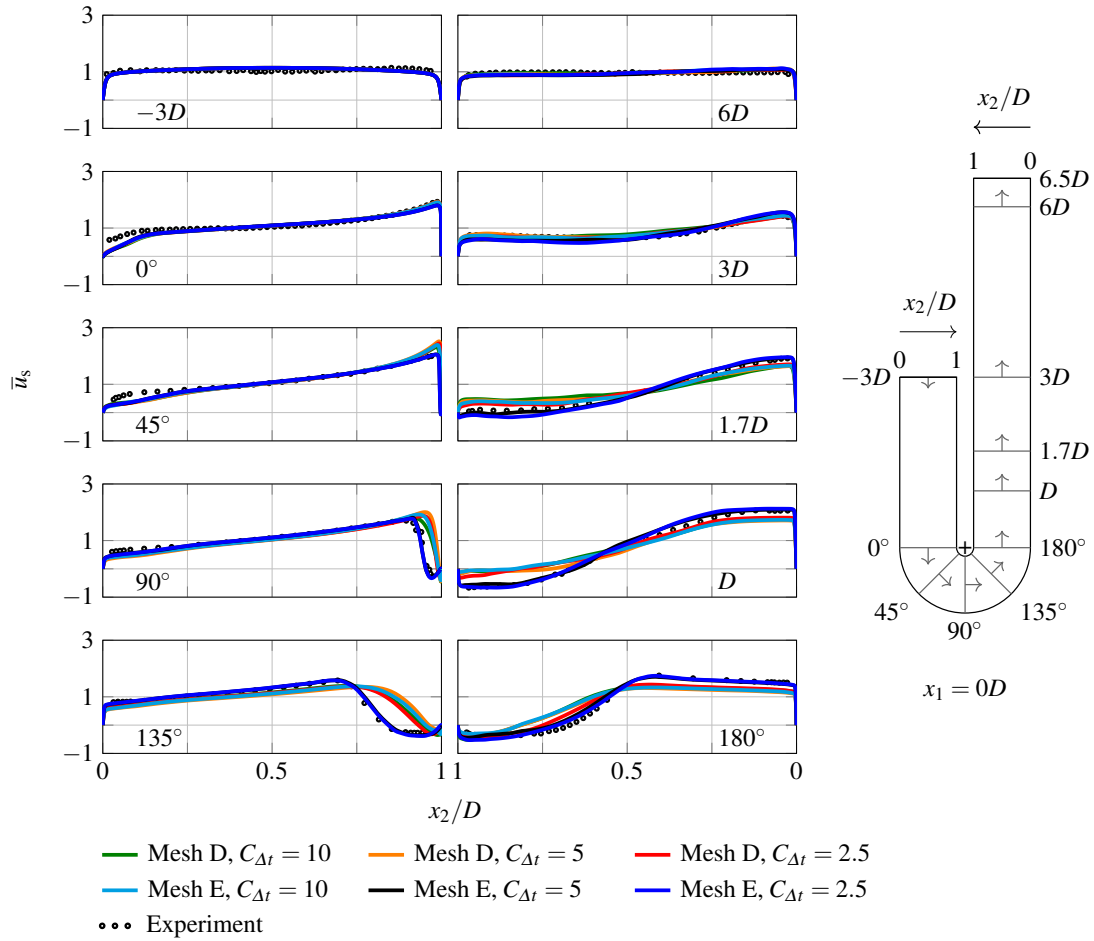


Figure 5.15: Effect of the Courant number on the streamwise velocity along the U-duct. Results are obtained using Mesh D and E. \bar{u}_s is calculated on the center plane. Time-average is taken over $\mathcal{T} = (33T, 36T)$. The reference results are adapted from [82]. Numerical results are adapted from [1]

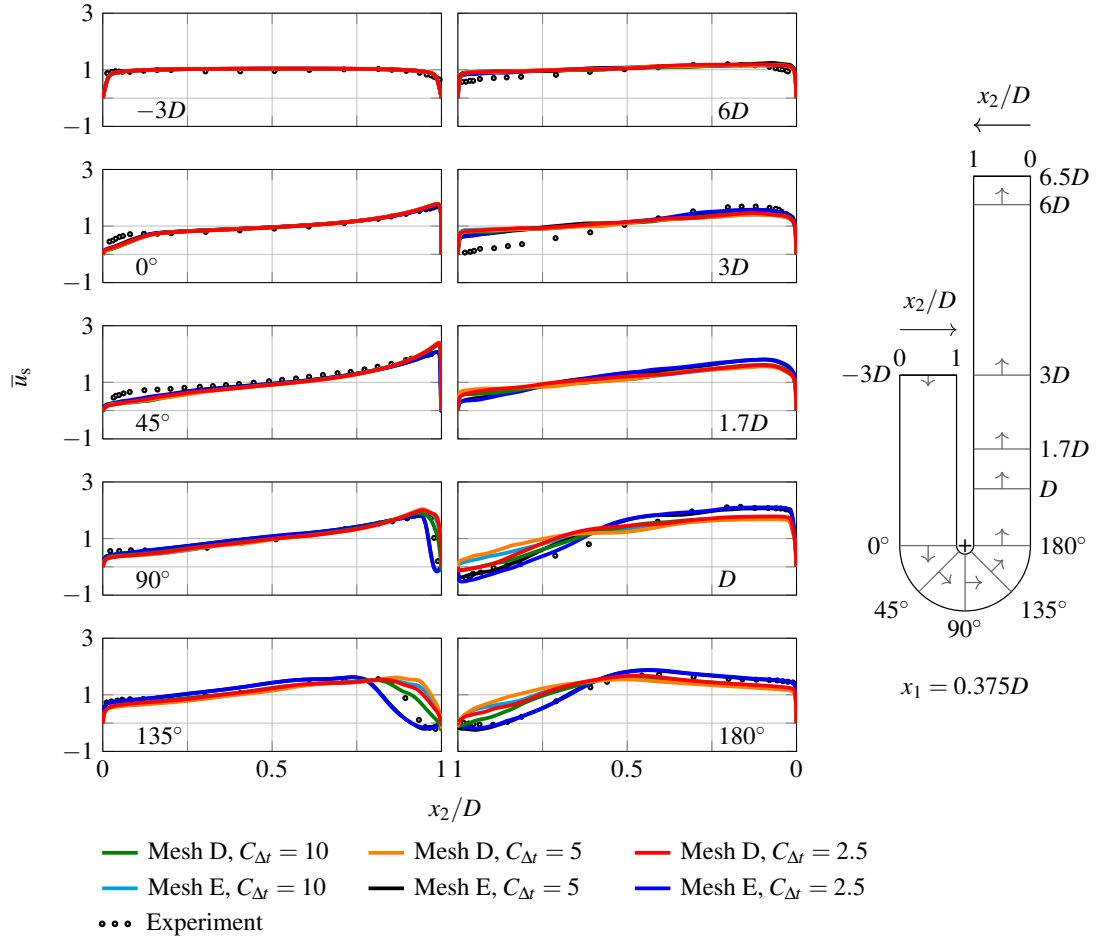


Figure 5.16: Effect of the Courant number on the streamwise velocity along the U-duct. Results are obtained using Mesh D and E. \bar{u}_s is calculated on the near-wall plane. Time-average is taken over $\mathcal{T} = (33T, 36T)$. The reference results are adapted from [82]. Numerical results are adapted from [1]

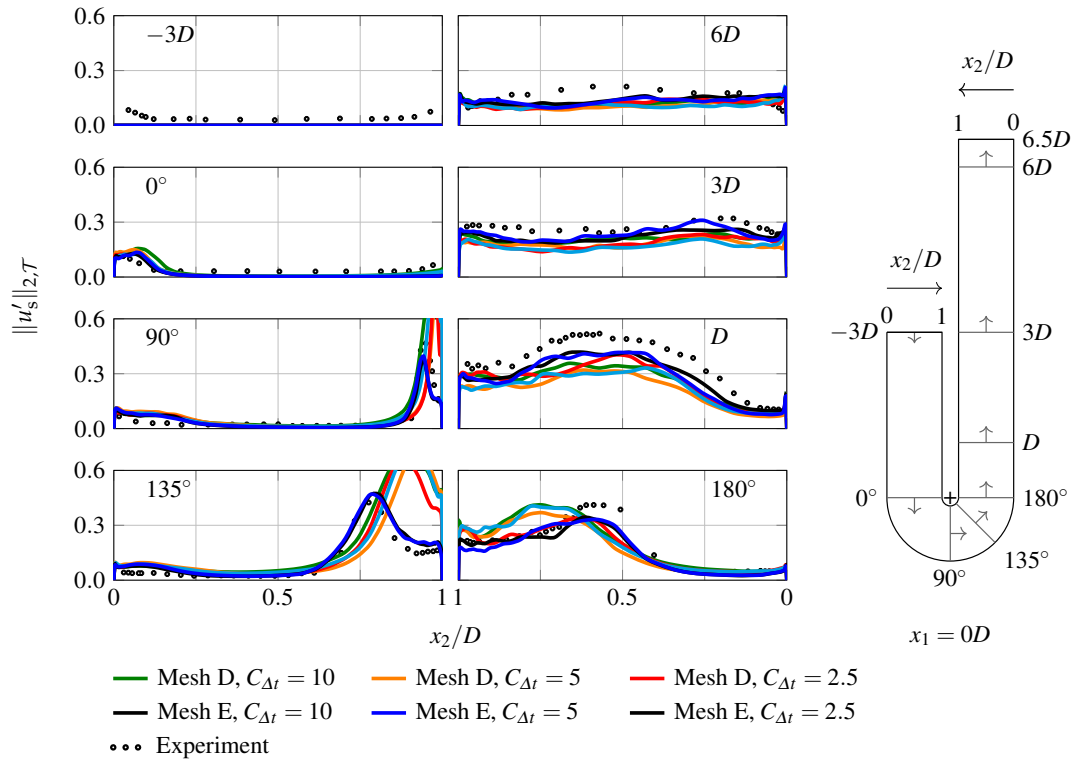


Figure 5.17: Effect of the Courant number on the root-mean-square fluctuating velocity along the U-duct. Results are obtained using Mesh D and E. $\|u'_s\|_{2,\mathcal{T}}$ is calculated on the center plane. Time-average is taken over $\mathcal{T} = (33T, 36T)$. The reference results are adapted from [82]. Numerical results are adapted from [1]

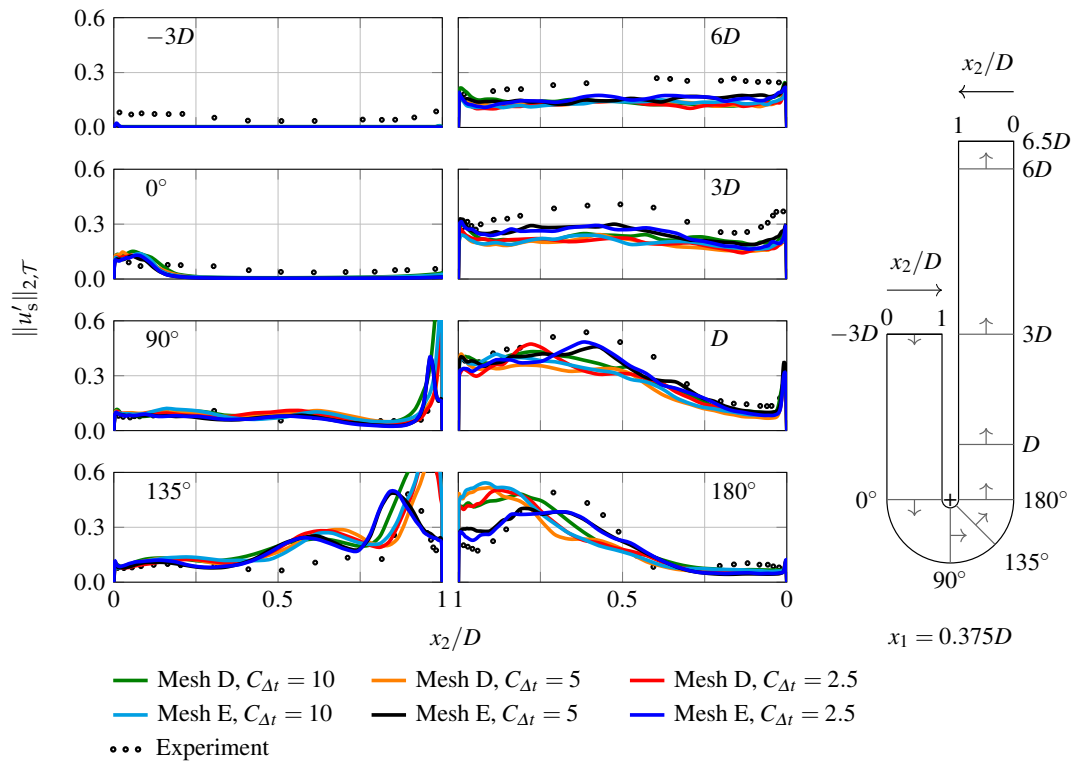


Figure 5.18: Effect of the Courant number on the root-mean-square fluctuating velocity along the U-duct. Results are obtained using Mesh D and E. $\|u'_s\|_{2,\mathcal{T}}$ is calculated on the near-wall plane. Time-average is taken over $\mathcal{T} = (33T, 36T)$. The reference results are adapted from [82]. Numerical results are adapted from [1]

Chapter 6

Taylor–Couette Flow Analysis

The classical Taylor–Couette flow problem that presents a range of flow patterns at different speeds of the inner and outer cylinders is studied and represented in this chapter. Accurate and efficient solution of these flow patterns significantly depends on the methods, with a reasonable computational cost, representing the geometry and motion of the cylinders accurately. Computations for four different Reynolds number combinations, in four different representations, including rotational-periodicity, of the computational domain, with two different enforcement of the prescribed velocities in two different reference frames using the conservative and nonconservative forms of the ST-VMS are conducted. The ST-VMS method with isogeometric discretization is performed in this chapter to address these challenges of simulating the Taylor–Couette flow. The cylindrical flow domain is exactly represented in space using quadratic NURBS patches. Rotation is exactly represented in the computations with the reference frame choice of IRF using the ST/NURBS Mesh Update Method, with temporal NURBS basis functions, and with NRF enforcing the angular velocity of the inner cylinder into the governing equations. With four different combinations of the Reynolds numbers, we computed the cases leading to the Couette flow, the Taylor vortex flow and the wavy vortex flow, where the waves are in motion. Our work shows that all these ST methods, integrated together, offer a high-fidelity computational analysis platform for the Taylor–Couette flow and for other classes of flow problems with similar features.

6.1 Problem setup

The computational domain for the Taylor–Couette flow is given in Figure 6.1. The flow conditions are represented by the cylinder radii r_i and r_o for the inner and outer cylinders, and $\eta = \frac{r_i}{r_o}$. The local orthonormal basis set \mathbf{e}_r , \mathbf{e}_θ and \mathbf{e}_z is used in the cylindrical coordinate system. Accordingly, u_r , u_θ and u_z denote the components of \mathbf{u} . With $\boldsymbol{\omega} = \omega \mathbf{e}_z$, the inner and outer cylinder velocities are written $U_i = \omega_i r_i$ and $U_o = \omega_o r_o$. Two different Reynolds numbers, $\text{Re}_i = \frac{U_i(r_o - r_i)}{\nu}$ and $\text{Re}_o = \frac{U_o(r_o - r_i)}{\nu}$ are defined. Here, $\nu = \frac{\mu}{\rho}$ is kinematic viscosity. A negative Reynolds number value defined by the outer cylinder velocity represents that the outer cylinder rotates in opposite direction to the inner cylinder. The time scale is defined as $T = \frac{2\pi}{\omega_i - \omega_o}$.

The ratio of cylinder radii, $\eta = 0.883$, is chosen the same as in [86]. Figure 6.2 illustrates the flow patterns depending on the inner and outer cylinder speeds. The combinations for the different speeds of the cylinders are given in Table 6.1. The reason why these cases are chosen is that the cylinders rotate in the same relative

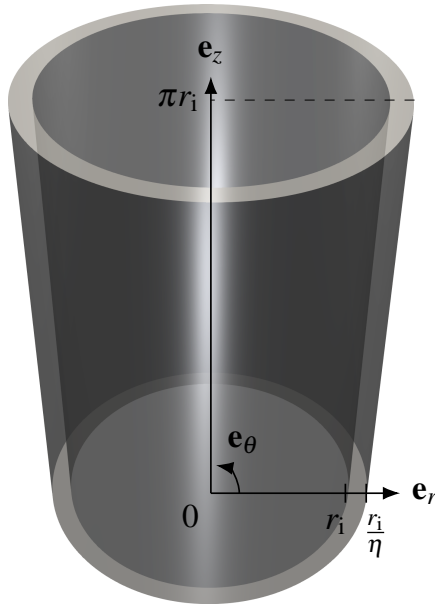


Figure 6.1: Computational domain. The local orthonormal basis set \mathbf{e}_r , \mathbf{e}_θ and \mathbf{e}_z is used in the cylindrical coordinate system

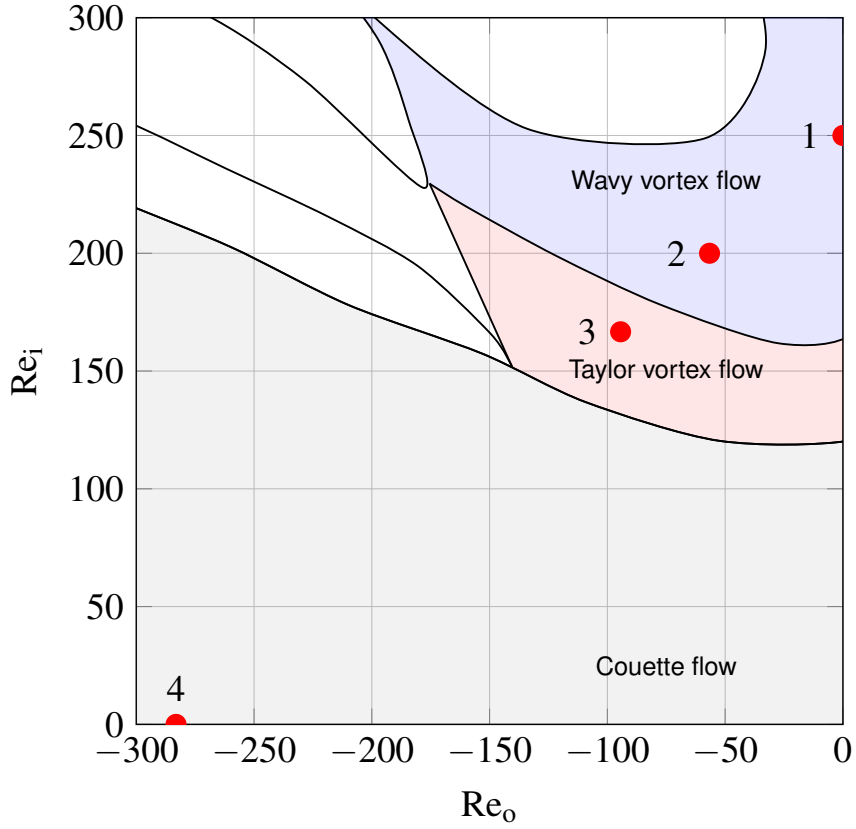


Figure 6.2: Taylor–Couette flow patterns. The Couette, Taylor vortex and wavy vortex flow are shown in *blue*, *red* and *gray* regions. The cases calculated in this study are marked by the *red* points. The inner cylinder rotation is given in the counter-clockwise direction and the negative Reynolds number means that the outer cylinder rotation in the clockwise direction. The figure has been adapted from [86] and also shown in [2]

Table 6.1: The Reynolds number combinations used in the computations

Case	Re_i	ηRe_o	Flow pattern
1	250	0	Wavy vortex
2	200	-50	Wavy vortex
3	166.67	-83.33	Taylor vortex
4	0	-250	Couette

speed to each other. Accordingly, $Re_i - \eta Re_o = 250$ for all.

To test the effect of reference frame in the computations, the mesh is rotated in the inner cylinder speed in the IRF. In the NRF, on the other hand, the rotation is represented by the angular velocity of the inner cylinder. The outer cylinder motion

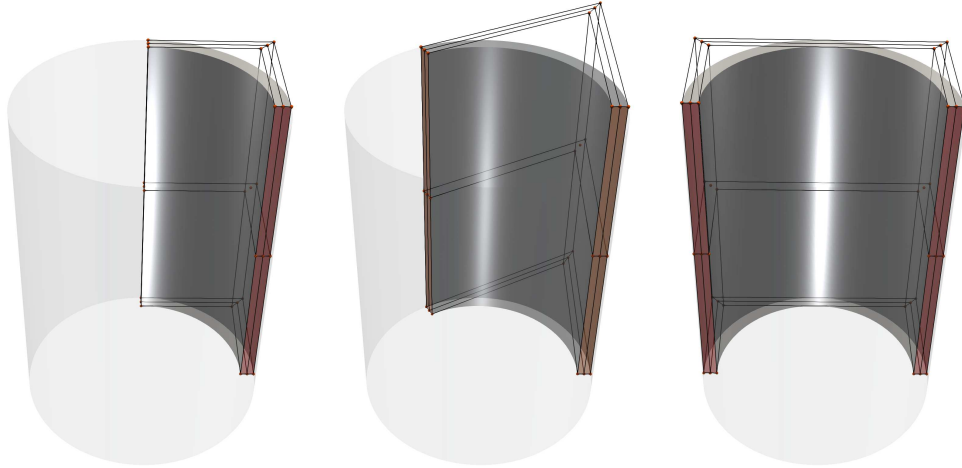


Figure 6.3: The circular geometry representation with quadratic NURBS patches that have quarter, one-third and half-domain sizes (*left to right*). This figure was also shown in [2]

in both situations is given by the prescribed-velocity condition. The flow domain is represented by axial periodicity over the length $L = \pi r_i$, and with both the full-domain and rotational-periodicity representations in the circumferential direction.

6.2 Meshes

The circular geometry of the problem is exactly represented by quadratic NURBS patches. The quarter, one-third and half-domain size models are represented by a patch while the full-domain size model is represented using two half-domain patches and connected in a C^0 continuous fashion. Figure 6.3 shows how the circular geometry is represented by quadratic NURBS patches with the minimum number of elements.

The quarter and one-third domain size patches are represented by using an element each, while the half-domain size has two elements to define the NURBS weights with positive values. Figure 6.4 shows the “coarse” meshes obtained from the meshes given in Figure 6.3 and using the knot-insertion method. The “medium” and “fine” meshes are obtained refining the coarse mesh twice and four times in all three spatial

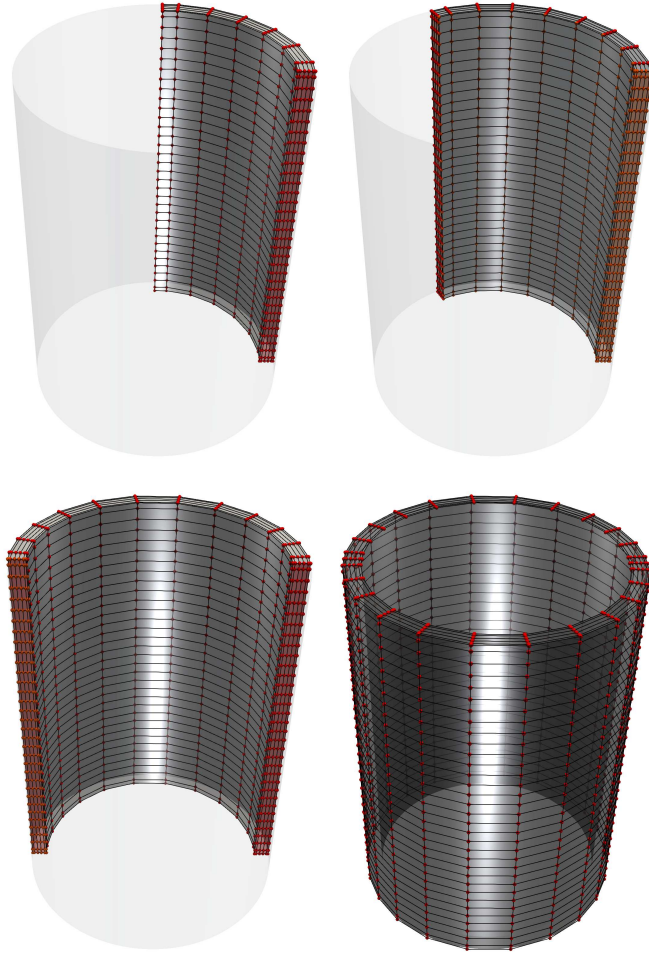


Figure 6.4: The coarse control meshes for the quarter, one-third, half-domain sizes and the full domain (*left to right, top to bottom*). The control points are shown by *red* circles

Table 6.2: Number of elements (ne) and control points (nc) in the radial, circumferential and axial directions

Mesh	Refinement	ne	nc
Quarter	Coarse	$4 \times 6 \times 32$	$6 \times 8 \times 34$
One-third	Coarse	$4 \times 8 \times 32$	$6 \times 10 \times 34$
Half	Coarse	$4 \times 12 \times 32$	$6 \times 14 \times 34$
Half	Medium	$8 \times 24 \times 64$	$10 \times 26 \times 66$
Half	Fine	$16 \times 48 \times 128$	$18 \times 50 \times 130$
Full	Coarse	$4 \times 24 \times 32$	$6 \times 26 \times 34$

dimensions. The number of elements and control points are shown in Table 6.2.

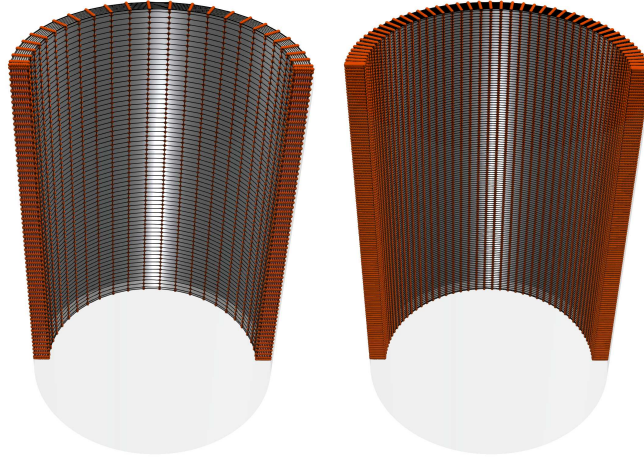


Figure 6.5: The medium and fine control meshes for the patch that has half-domain size. The control points are shown by *red* circles. This figure was also shown in [2]

6.3 Boundary conditions and mesh motions

The no-slip conditions are enforced strongly or weakly, depending on the test computation, on the inner and outer cylinder surfaces. The periodicity is enforced with the ST-SI in the axial direction. For the computations in the IRF, $U_i \mathbf{e}_\theta$ and $U_o \mathbf{e}_\theta$ are prescribed on the inner and outer surfaces, and the mesh is rotated at inner surface rotational speed of ω_i . For the computations in the NRF, zero and $(U_o - U_i \frac{1}{\eta}) \mathbf{e}_\theta$ are prescribed on the inner and outer surfaces, and the mesh is not moved. The fictitious forces are inserted into the momentum equation based on the ω_i .

6.4 Computational conditions

We use the conservative or nonconservative form of the ST-VMS, in different test computations. The rotation is based on quadratic NURBS functions, while the flow solution is based on linear functions in time. The time-step size is set $\Delta t = \frac{T}{60}$, $\frac{T}{120}$ and $\frac{T}{240}$ for the computations performed using the coarse, medium and fine meshes. The mesh rotation in a time step is set 6° , 4.8° and 4° in the Cases 1, 2 and 3 for the computations with the coarse mesh in the IRF. The amounts are

halved for the medium mesh and quartered for the fine mesh considering the use of the same Courant number. The time-step size is important in the computations for the accuracy in representing the prescribed velocity. 500 GMRES iterations are performed per nonlinear iteration which is 3 per time step in all variations except the computations given in Section 6.5.6. In that section, we set the nonlinear iteration number 5 per time step for a detailed investigation.

6.5 Results

The Taylor–Couette flow analysis is performed for different scenarios and the results are presented under flow development, rotational periodicity analysis, mesh refinement, different flow patterns and different methods subsections of this section.

The conservative form of the ST-VMS is used and the prescribed velocity is strongly enforced in all variations except the last subsection where we used both conservative and nonconservative versions of the ST-VMS with both weak and strong enforcements of the prescribed velocities.

Figure 6.6 shows the configurations we used for flow visualization. The axial velocity isosurfaces and velocity magnitude are visualized in the volume and sections given in Figure 6.6. The computation results obtained in the NRF are transformed to the IRF, and the quarter, one-third and half-domain sizes are replicated for visualization.

The notation $\mathcal{T} = (T_1, T_2)$ is used to indicate the time range to represent a time-averaging period. The space or time average of a quantity is shown with an overbar, for example $\bar{\omega}$, and if the average of a quantity is taken in both space and time, it is shown with a double overbar, for example $\overline{\bar{\omega}}$.

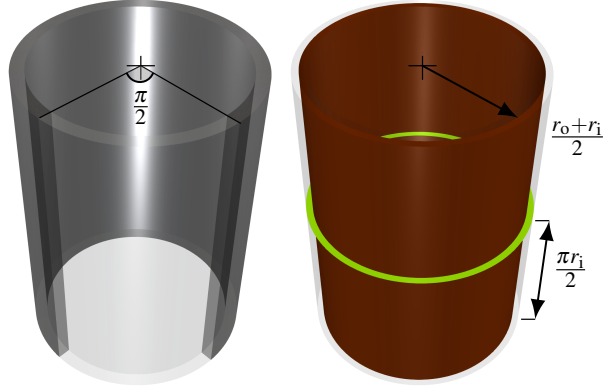


Figure 6.6: Flow visualization configurations in a volume (*left*) and section (*right*). $\frac{1}{4}$ of the flow field is subtracted in a volume visualization and the results are shown in the remaining *gray* part. The *red* and *green* sections are placed at the center along the radial and axial directions for a section visualization. This figure was also shown in [2]

6.5.1 Flow development: Case 1

The domain is represented in the full size and the coarse mesh is used for all computations given in this subsection. The flow development is visualized by the $u_z / (U_i - \eta U_o)$ at various instants and analyzed with the f -based Fourier decomposition of $u_\theta / (U_i - \eta U_o)$ at $r = \frac{r_o+r_i}{2}$, $\theta = 0$ in Figures 6.7 and 6.8. A space average of the amplitude is taken to diminish the influence of the wave location in axial direction. 4 waves in the circumferential direction are observed in both figures, and 7 waves can be counted in the axial direction in Figure 6.7. The waves move in the circumferential direction with the same sign as $\omega_i - \omega_o$, and the lower-mode solutions clearly reflect the motion of the waves. The time-periodic solution is obtained after $50T$.

6.5.2 Flow development: Case 4

In Case 4, the full-domain representation and the coarse mesh is used in the computations. Figures 6.9 and 6.10 show velocity magnitude $\|\mathbf{u}\|$ at $t = 9T$ and space-averaged angular velocity $\bar{\omega}$ at various instants.

The solution in Case 4 is the steady state in the circumferential direction and there is no variation in the axial direction. The solution reaches the steady state regime after $t = 3T$, when the initial velocity is set zero everywhere except the outer cylinder surface.

6.5.3 Rotational periodicity: Case 1

In this section, the Taylor–Couette flow for Case 1 is computed in the periodic and full-domain models using the coarse mesh. The isosurfaces of $u_z / (U_i - \eta U_o)$ after the solutions become periodic (in Figure 6.11), and the λ -based Fourier decomposition of $u_\theta / (U_i - \eta U_o)$ at $t = 80T$ (in Figure 6.12) are shown, for both the periodic models and the full-domain representation in the IRF and NRF.

The amplitude is averaged in space along the axial direction. It is obvious in Figure 6.12 that the largest mean amplitude of the Fourier coefficients is at $\lambda = \pi \frac{r_o + r_i}{4}$. The results obtained using the one-third representation of the computational domain do not agree with the results from full-domain as was foreseeable. Additionally, the solutions achieved in the IRF and NRF are slightly different at higher modes. On the other hand, with the model representing half-domain size, the solution has a good settlement with the solution achieved by the full-domain. Following this fact, in the rest of this chapter, the rotational-periodicity representation with the model that has half-domain size is used.



Figure 6.7: Flow development in Case 1. Isosurfaces of $u_z / (U_i - \eta U_o)$ in the IRF (*left*) and NRF (*right*), with the full-domain representation of the flow field using the coarse mesh, at $t = 10T, 30T, 50T$ and $70T$ (from *top* to *bottom*). 16 isosurfaces are used in $-0.15 \leq u_z / (U_i - \eta U_o) \leq 0.15$. This figure was also shown in [2]

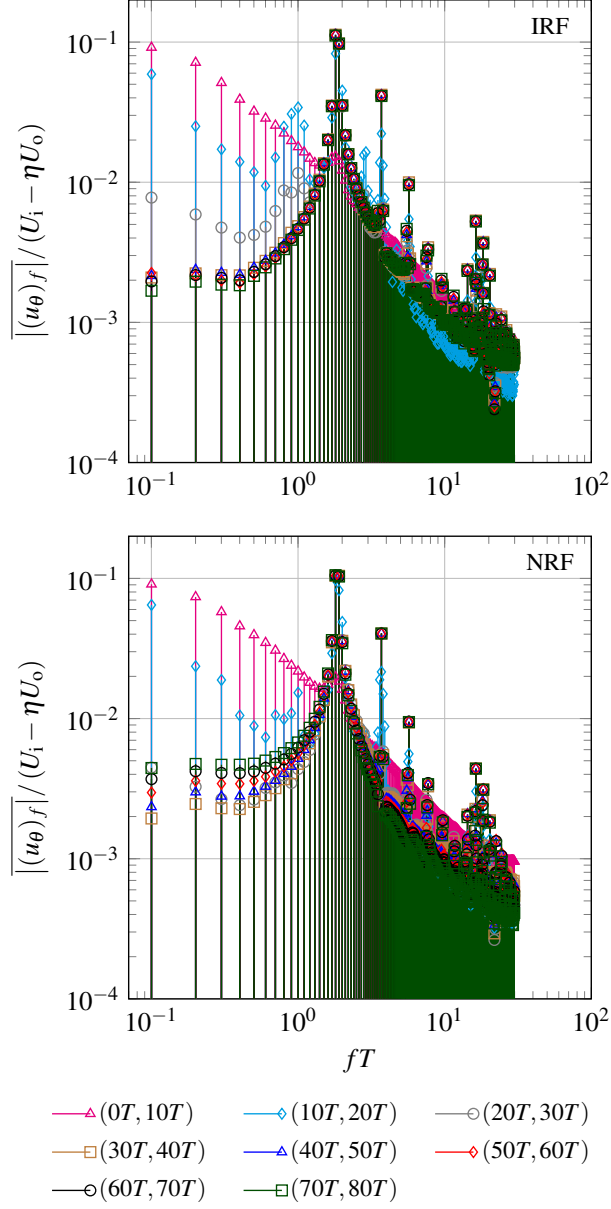


Figure 6.8: Flow development in Case 1 by the f -based Fourier decomposition of $u_\theta / (U_i - \eta U_o)$ at $r = \frac{r_o + r_i}{2}$, $\theta = 0$. The different time ranges, all spanning $10T$, are given in the legend. The amplitude of the Fourier coefficients is averaged in space along the axial direction at 56 equally-spaced points. This figure was also shown in [2]



Figure 6.9: $\|\mathbf{u}\| / (U_i - \eta U_o)$ at $t = 9T$ for Case 4. This figure was also shown in [2]

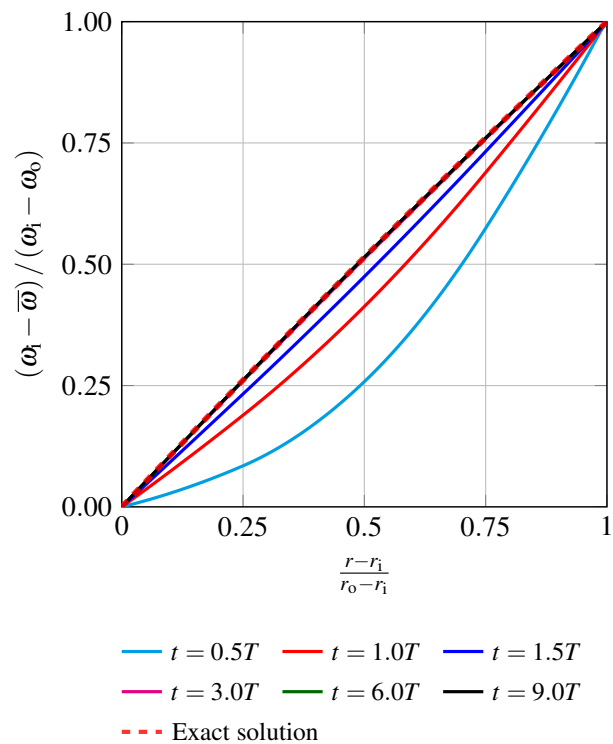


Figure 6.10: Flow development by $(\omega_i - \bar{\omega}) / (\omega_i - \omega_o)$ in Case 4. Velocity is averaged in space in both axial and circumferential directions. This figure was also shown in [2]



Figure 6.11: Isosurfaces of $u_z / (U_i - \eta U_o)$ in Case 1 in the IRF (*left*) and NRF (*right*), with the quarter, one-third, half-domain and full-domain representations of the flow field (from *top* to *bottom*), after the solutions become periodic. 16 isosurfaces are used in $-0.15 \leq u_z / (U_i - \eta U_o) \leq 0.15$. This figure was also shown in [2]

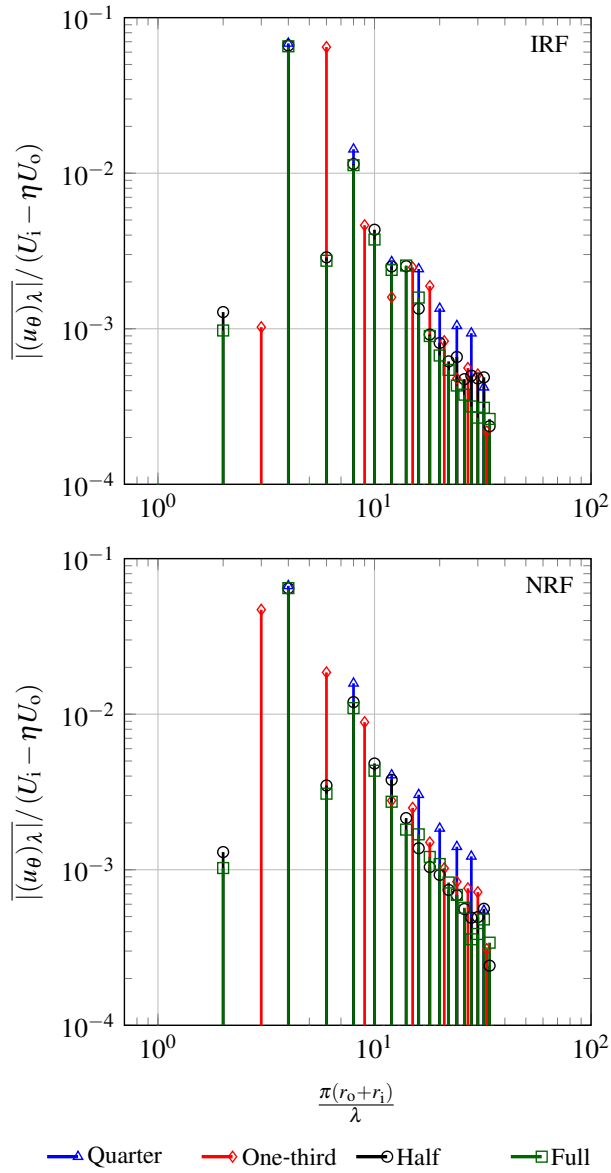


Figure 6.12: λ -based Fourier decomposition of $u_\theta / (U_i - \eta U_o)$ at $t = 80T$, $r = \frac{r_o+r_i}{2}$ in Case 1, with the quarter, one-third, half-domain and full-domain representations of the flow field. The amplitude of the Fourier coefficients is averaged in space along the axial direction at 56 equally-spaced points. This figure was also shown in [2]

6.5.4 Mesh refinement: Case 1

Three levels of mesh refinement with the rotational-periodicity representation with the model that has half-domain size are tested in this section. After the solutions become periodic, the effect of mesh is investigated in Figures 6.13 and 6.14 both in the IRF and NRF, by the isosurfaces of $u_z / (U_i - \eta U_o)$ and $\|\mathbf{u}\| / (U_i - \eta U_o)$. The ST-averaged angular velocity, $(\omega_i - \bar{\omega}) / (\omega_i - \omega_o)$ is shown in Figure 6.15, in the IRF and NRF, for the coarse, medium and fine meshes. The solution convergence with the mesh refinement is evident.

6.5.5 Flow patterns: Cases 2 and 3

We know from Figure 6.2 that Case 3 has no waves in the circumferential direction. We also know from a prior computation we conducted for Case 2 with the full-domain representation, which we do not report here, that the number of waves in the circumferential direction is even. Therefore we compute both cases with the rotational-periodicity representation with the patch that has half-domain size. We use the medium mesh.

Figures 6.16 and 6.17 show, for Case 2, for both the IRF and NRF, the isosurfaces of $u_z / (U_i - \eta U_o)$ and section values of $\|\mathbf{u}\| / (U_i - \eta U_o)$ at various instants. For both the IRF and NRF, we see eight waves in the circumferential direction. They move in the circumferential direction with the same sign as $\omega_i - \omega_o$. Figure 6.18 shows, for both the IRF and NRF, $(\omega_i - \bar{\omega}) / (\omega_i - \omega_o)$. It clearly indicates that the IRF and NRF solutions are in very good agreement.

Figure 6.19 shows, for Case 3, for both the IRF and NRF, the isosurfaces of $u_z / (U_i - \eta U_o)$ at $t = 15T$. For both the IRF and NRF, we see the Taylor-vortex flow pattern. Figure 6.20 shows, for both the IRF and NRF, $(\omega_i - \bar{\omega}) / (\omega_i - \omega_o)$, which clearly indicates that the two solutions are in very good agreement.

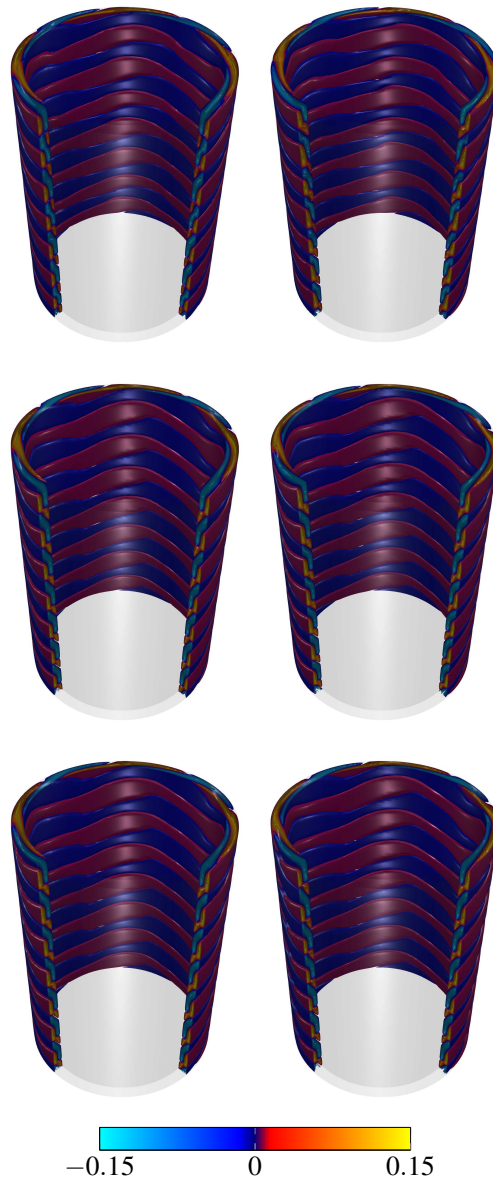


Figure 6.13: Mesh refinement in Case 1. Isosurfaces of $u_z / (U_i - \eta U_o)$ in the IRF (*left*) and NRF (*right*), with the half-domain representation of the flow field, using the coarse, medium and fine meshes (from *top* to *bottom*). 16 isosurfaces are used in $-0.15 \leq u_z / (U_i - \eta U_o) \leq 0.15$. This figure was also shown in [2]

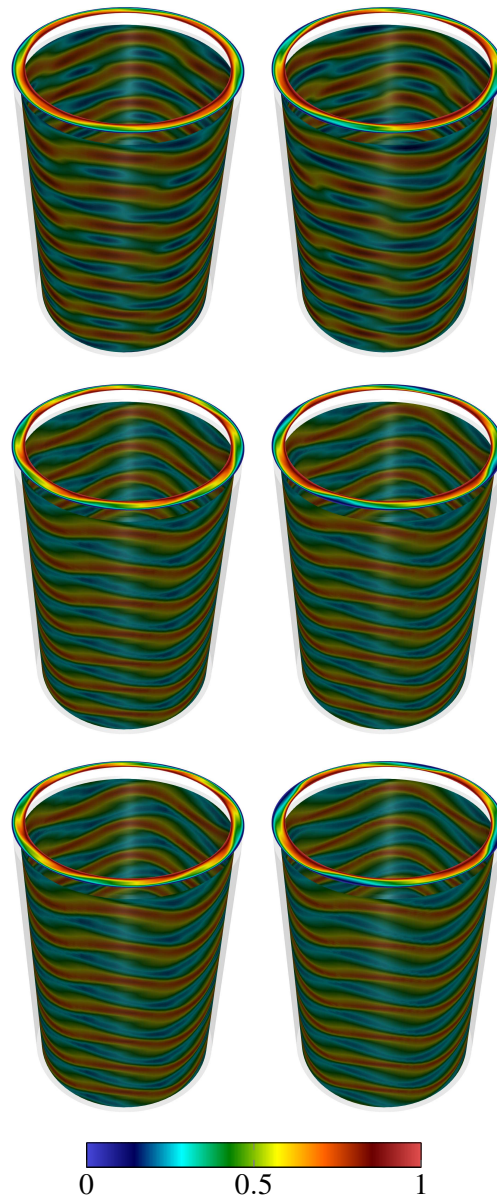


Figure 6.14: Mesh refinement in Case 1. $\|\mathbf{u}\| / (U_i - \eta U_o)$ in the IRF (*left*) and NRF (*right*), with the half-domain representation of the flow field, using the coarse, medium and fine meshes (from *top* to *bottom*). This figure was also shown in [2]

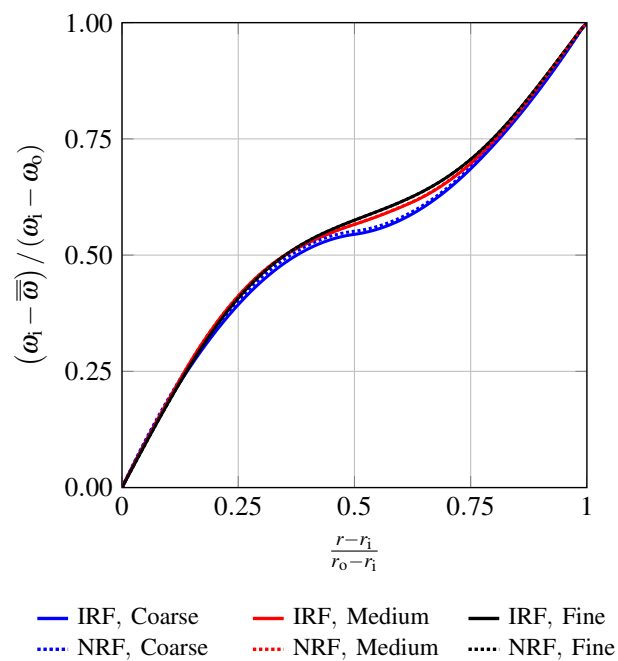


Figure 6.15: The ST-averaged angular velocity, $(\omega_i - \bar{\omega}) / (\omega_i - \omega_o)$ in Case 1 over the range $\mathcal{T} = (97T, 100T)$. The velocity is averaged in space along both axial and circumferential directions. This figure was also shown in [2]

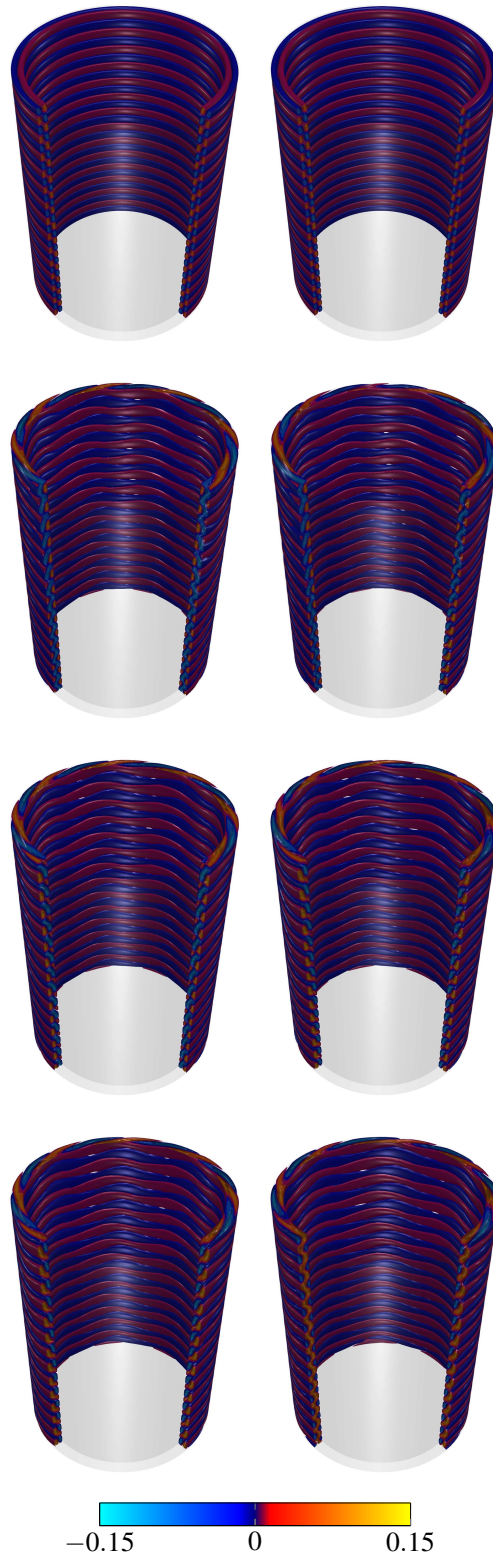


Figure 6.16: Flow development in Case 2. Isosurfaces of $u_z / (U_i - \eta U_o)$ in the IRF (*left*) and NRF (*right*), with the half-domain representation of the flow field, using the medium mesh, at $t = 5T, 10T, 15T$ and $20T$ (from *top* to *bottom*). 16 isosurfaces are used in $-0.15 \leq u_z / (U_i - \eta U_o) \leq 0.15$. This figure was also shown in [2]

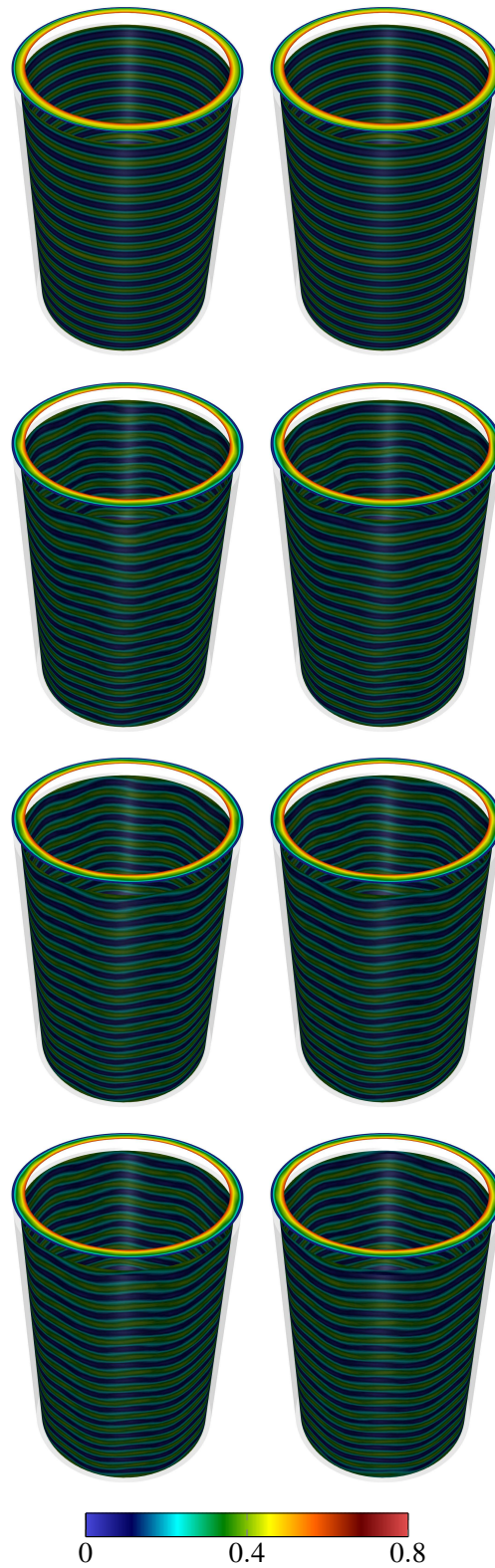


Figure 6.17: Flow development in Case 2. $\|\mathbf{u}\| / (U_i - \eta U_o)$ in the IRF (*left*) and NRF (*right*), with the half-domain representation of the flow field, using the medium mesh, at $t = 5T, 10T, 15T$ and $20T$ (from *top* to *bottom*). This figure was also shown in [2]

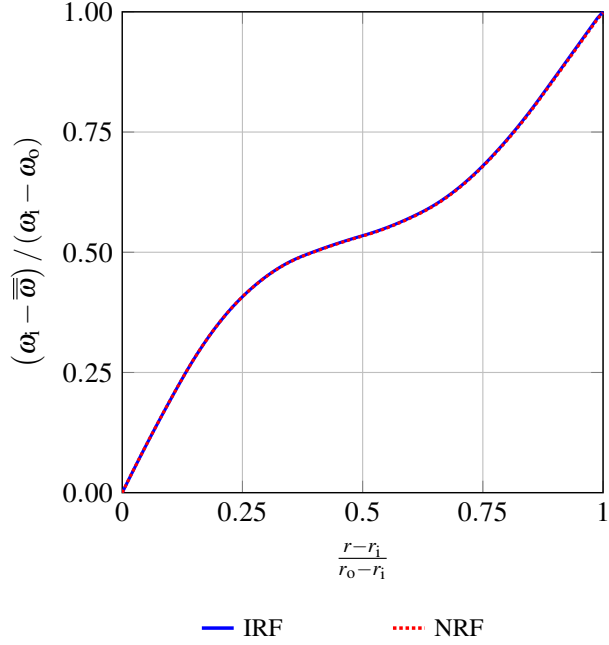


Figure 6.18: The ST-averaged angular velocity, $(\omega_i - \bar{\omega}) / (\omega_i - \omega_o)$ in Case 2 over the range $\mathcal{T} = (15T, 20T)$. The velocity is averaged in space along both axial and circumferential directions. This figure was also shown in [2]

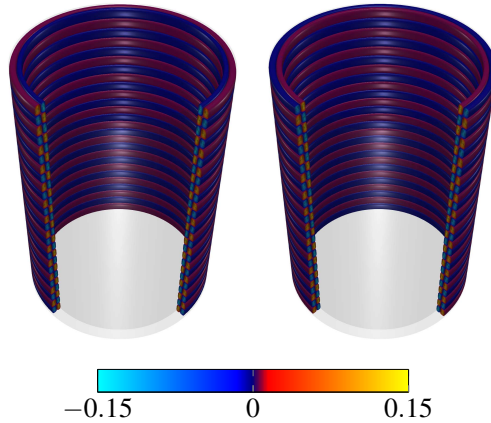


Figure 6.19: Case 3. Isosurfaces of $u_z / (U_i - \eta U_o)$ in the IRF (*left*) and NRF (*right*), with the half-domain representation of the flow field, using the medium mesh, at $t = 15T$. 16 isosurfaces are used in $-0.15 \leq u_z / (U_i - \eta U_o) \leq 0.15$. This figure was also shown in [2]

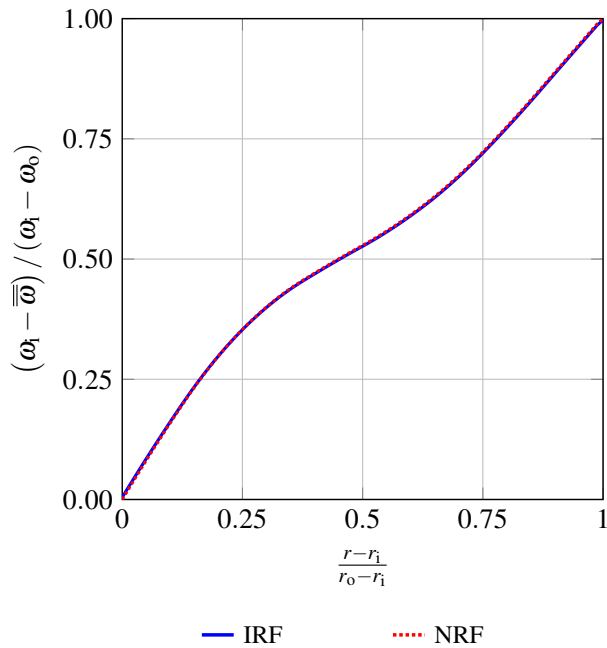


Figure 6.20: The ST-averaged angular velocity, $(\omega_i - \bar{\omega})/(\omega_i - \omega_o)$ in Case 3 over the range $\mathcal{T} = (10T, 15T)$. The velocity is averaged in space along both axial and circumferential directions. This figure was also shown in [2]

6.5.6 Methods: Case 1

Eight different cases of the computations are compared in this section. All the computations are performed over the rotational-periodicity representation with the model of half-domain size by the medium mesh. The prescribed velocities are enforced both strongly and weakly, using both the conservative and nonconservative versions of the ST-VMS, and both in the IRF and NRF. The number of GMRES iterations per nonlinear iteration is the same as the previous section and 500, while we increased the number of nonlinear iterations to 5 in this section for detailed comparison purposes. Figure 6.21 shows the ST-averaged angular velocity $(\omega_i - \bar{\omega})/(\omega_i - \omega_o)$. All the cases are in a good agreement in terms of the velocity profiles.

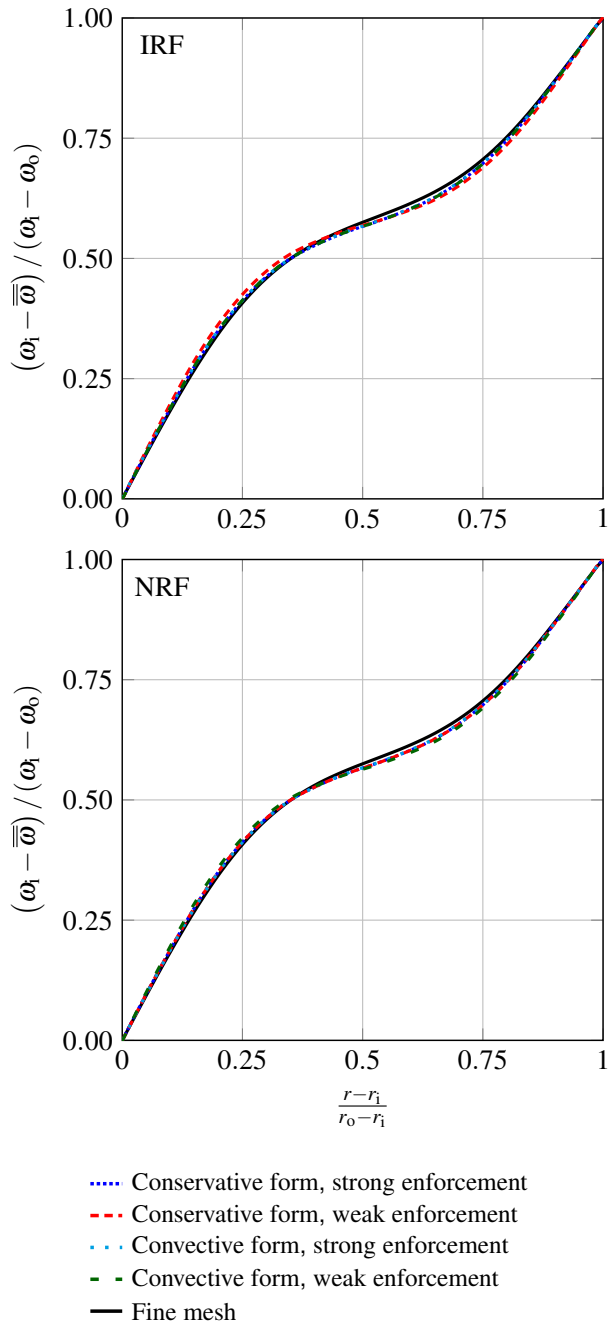


Figure 6.21: The ST-averaged angular velocity, $(\omega_i - \bar{\omega}) / (\omega_i - \omega_o)$ in Case 1 over the range $\mathcal{T} = (105T, 110T)$. The velocity is averaged in space along both axial and circumferential directions. The solution computed using the fine mesh is also shown as a reference, using the strong enforcement of the prescribed velocities, with the conservative version of the ST-VMS, in the IRF. This figure was also shown in [2]

In the rest of this section, the global conservation of angular momentum by the torque acting on the cylinders is investigated. The global conservation formulations are derived from the both form of the ST-VMS equation in both reference frames in Section 4.3. But here, for simplicity, we define the angular momentum in the n^{th} time slab as follows:

$$\mathbf{L}_n^- = \int_{\Omega_n} \mathbf{r} \times \mathbf{u}_n^- d\Omega, \quad (6.1)$$

and the angular momentum time-averaged over the range $\mathcal{T} = (T_1, T_2)$ as

$$\bar{\mathbf{L}} = \frac{1}{T_2 - T_1} \int_Q \mathbf{r} \times \mathbf{u} dQ, \quad (6.2)$$

where Q is the ST domain between the times T_1 and T_2 . The torques acting on the cylinders are defined as follows:

$$(\Upsilon_n)_{\text{IB}} = \frac{1}{\Delta t} \int_{(P_n)_{\text{IB}}} \mathbf{r} \times \mathbf{h} dP, \quad (6.3)$$

$$(\Upsilon_n)_{\text{OB}} = \frac{1}{\Delta t} \int_{(P_n)_{\text{OB}}} \mathbf{r} \times \mathbf{h} dP. \quad (6.4)$$

Here, \mathbf{h} , which is the boundary flux as given in previous chapters in detail, is computed on the cylinder surfaces as a part of the flow solution, in different ways for the strong and weak enforcements of the prescribed velocity. The definition $(\Upsilon_n)_{\text{IB}}$ and $(\Upsilon_n)_{\text{OB}}$ are used to denote the axial components. The global conservation of the angular momentum can be written as

$$\frac{\mathbf{L}_{n+1}^- - \mathbf{L}_n^-}{\Delta t} = (\Upsilon_n)_{\text{IB}} + (\Upsilon_n)_{\text{OB}}, \quad (6.5)$$

for every time step. Theoretically, the angular momentum is only balanced in the conservative version of the ST-VMS.

Table 6.3: Angular momentum ($\bar{L}/\bar{L}_{\text{FINE}}$) and torque $\bar{\Upsilon}_{\text{IB}}T/\bar{L}_{\text{FINE}}$ of the eight cases with respect to angular momentum from fine mesh

Velocity enforcement	Formulation	$\bar{L}/\bar{L}_{\text{FINE}}$		$\bar{\Upsilon}_{\text{IB}}T/\bar{L}_{\text{FINE}}$	
		IRF	NRF	IRF	NRF
Strong	Conservative	1.0066	1.0072	0.7102	0.7102
	Nonconservative	1.0067	1.0066	0.7093	0.7083
Weak	Conservative	1.0080	1.0068	0.7469	0.7111
	Nonconservative	1.0065	1.0102	0.7093	0.7334

In Table 6.3, $\bar{L}/\bar{L}_{\text{FINE}}$ and $\bar{\Upsilon}_{\text{IB}}T/\bar{L}_{\text{FINE}}$ are shown for all cases tested in this section. The time-averaged torque is defined using the torque counterpart of Eq. (6.2). The mean angular momentum from fine mesh \bar{L}_{FINE} , is calculated using strong enforcement of the prescribed velocities with the conservative version of the ST-VMS in the IRF in $\mathcal{T} = (97T, 102T)$. All \bar{L} values are calculated quite close to \bar{L}_{FINE} , while the $\bar{\Upsilon}_{\text{IB}}$ values vary slightly between the cases. The global angular momentum balance given in Eq. (6.5) is shown in Figures 6.22–6.24, with some arrangements for $\frac{(L_{n+1}^- - L_n^-)T}{\Delta t \bar{L}_{\text{FINE}}}$, $\frac{(\Upsilon_{\text{IB}} + \Upsilon_{\text{OB}})T}{\bar{L}_{\text{FINE}}}$. For comparison purpose, we also show the same with the fine mesh in Figure 6.24. It is clear that, in all the cases, global angular momentum balanced practically at every time step. In all cases, there are fluctuations with the same period with variable magnitude. Representation of the prescribed velocities are exact in the computations with the NRF and in the computations with weak enforcement. According to this, it can be said that the fluctuations are not coming from how the prescribed velocities are presented. The reason of the fluctuations can be explained by the inertia itself or nonuniform element lengths in the circumferential direction. Even in the computation with nonconservative form of the ST-VMS, weak enforcement of the prescribed velocities, and the NRF, where we see the largest fluctuations in $\frac{(L_{n+1}^- - L_n^-)T}{\Delta t \bar{L}_{\text{FINE}}}$, the maximum fluctuation is 0.3 %. Therefore, we consider these fluctuations to be acceptable in computation of the wavy-vortex flows.

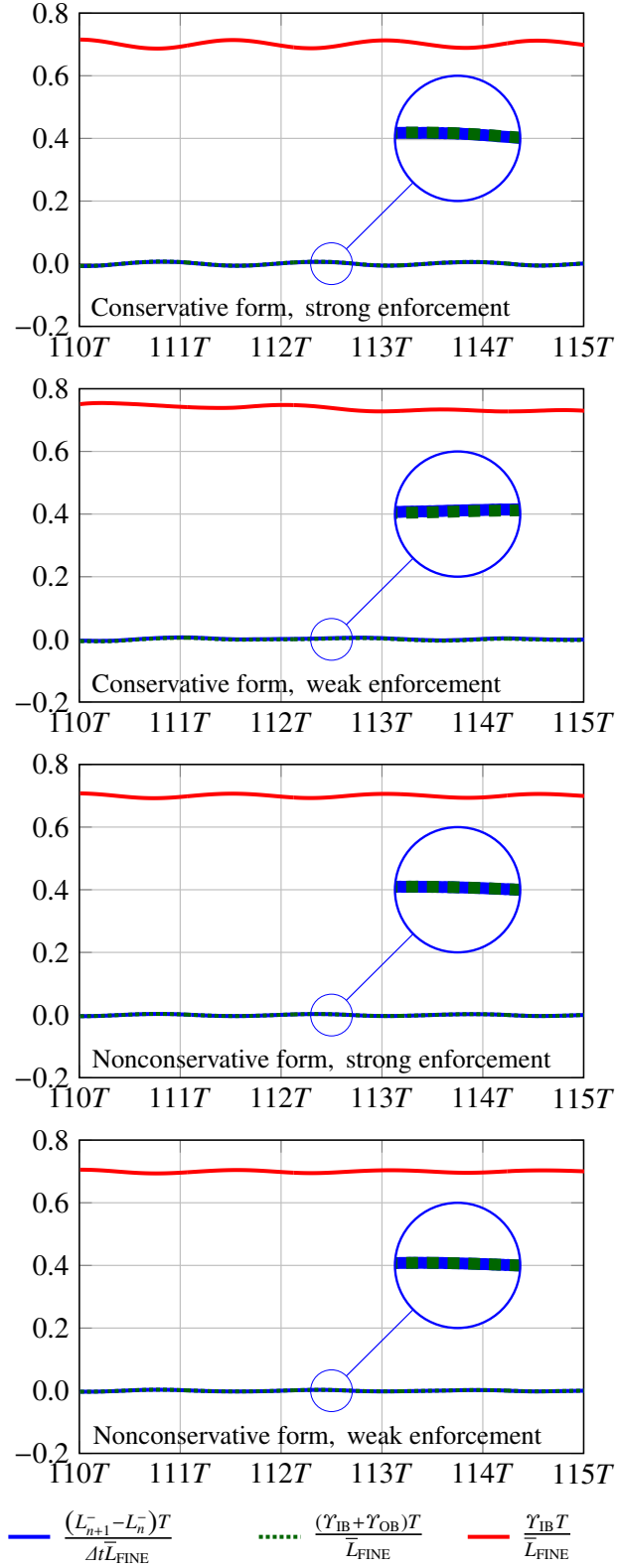


Figure 6.22: Global angular momentum balance in Case 1, in the IRF. The *blue* circles show a closer view for each case. Figure is adapted from [2]

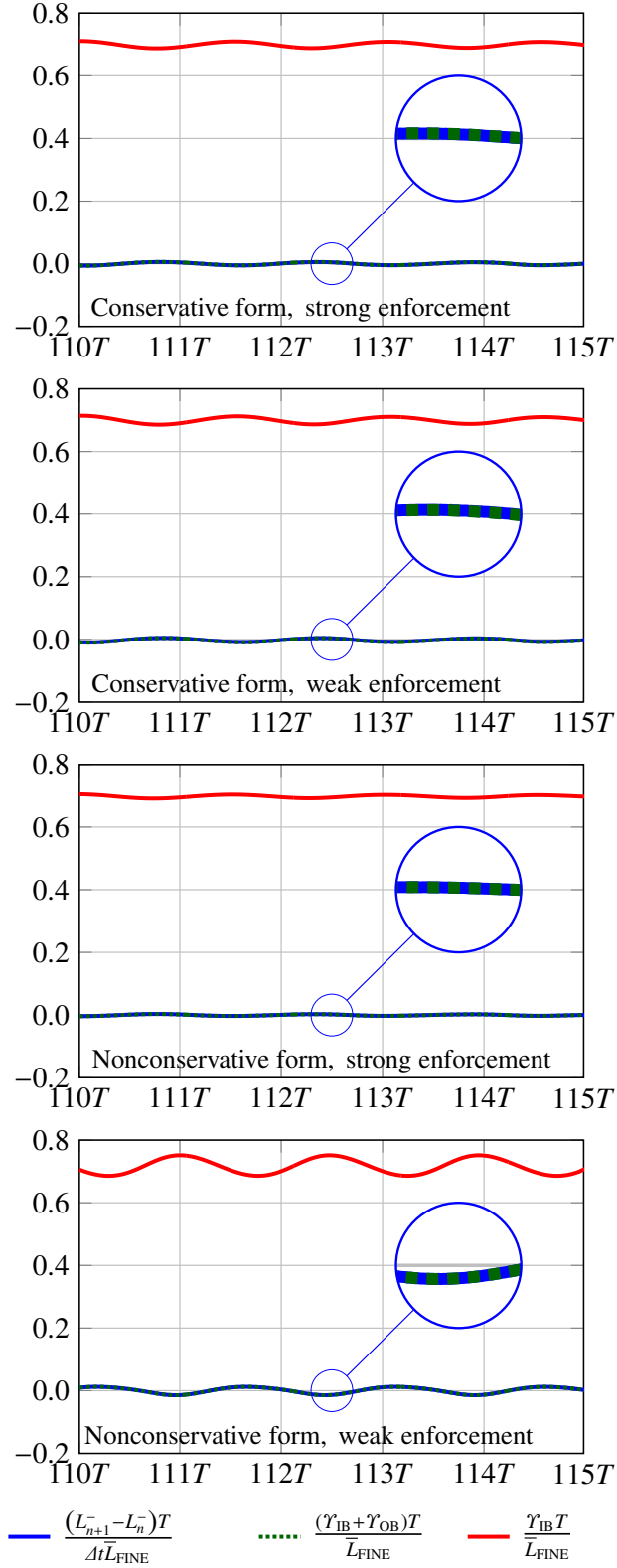


Figure 6.23: Global angular momentum balance in Case 1, in the NRF. The *blue* circles show a closer view for each case. Figure is adapted from [2]

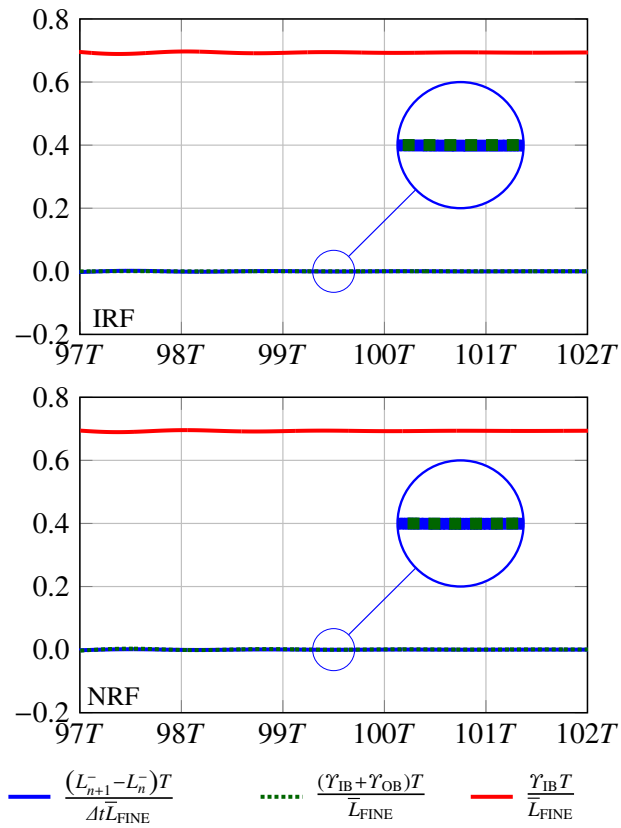


Figure 6.24: Global angular momentum balance in Case 1, in the IRF and NRF for the solution achieved using the fine mesh. The prescribed velocities are enforced strongly and conservative version of the ST-VMS is used. The *blue* circles show a closer view for each case. Figure is adapted from [2]

Chapter 7

Computations in an Engineering Application

Flow analysis in a double-suction centrifugal pump is studied and represented in this chapter. Fluid flow modeling in centrifugal pumps, involving turbulence, flow separation and recirculation, is one of the most challenging subjects in CFD. Time dependent impeller position with respect to the outer volute tongues causes strong pressure fluctuations. Extremely distorted flow pattern and unsteady dynamic forces occur due to the pressure fluctuations and it is known as the main source of noise and vibration. This situation is also responsible for pump performance losses.

In order to address these challenges in this real-world turbomachinery flow problem, we used the ST-VMS method with isogeometric discretization which was found accurate and efficient in turbulent-flow computations in Chapter 5 and in flow computations with rotating components in Chapter 6. The geometry is represented accurately with a reasonably coarse mesh using the power of the ST-IGA. The rotation of the impeller in the IRF is represented exactly by quadratic NURBS basis functions in time. The rotating components in this reference frame are connected to the stationary parts by the ST-SI. For seven different flow rate values, the pump performance is calculated and compared to some experimental results. In addition, one-fifth of the impeller with hub and shroud is represented by the rotational-periodicity by the ST-SI, and the symmetry in the axial direction is represented using a slip condition. The flow around impeller is calculated using this flow domain in the NRF. The inflow velocity profile is used from the computations with the full-domain at the impeller entrance. The shaft power obtained in this part matched well with the reference data.

7.1 Problem setup

The Reynolds number is more than that $Re = \frac{\rho U D}{\mu} = 10^6$, where D is suction volute inlet diameter. U is calculated from the volumetric flow rate and inlet cross sectional area as $U = Q_0/A$ at the best efficiency point. The computations are performed for seven different cases with the flow rates as $Q = 0.4 Q_0, 0.6 Q_0, 0.8 Q_0, 1.0 Q_0, 1.2 Q_0, 1.4 Q_0$ and $1.6 Q_0$.

Inlet velocity is defined in the normal inward direction as an average speed. Figure 7.1 represents the boundary conditions. The inflow and outflow surfaces, the surfaces where the pump performance is calculated and the SIs between spinning and non-moving parts and between multiple stationary parts, such as in the suction volute, are given and explained in the caption.

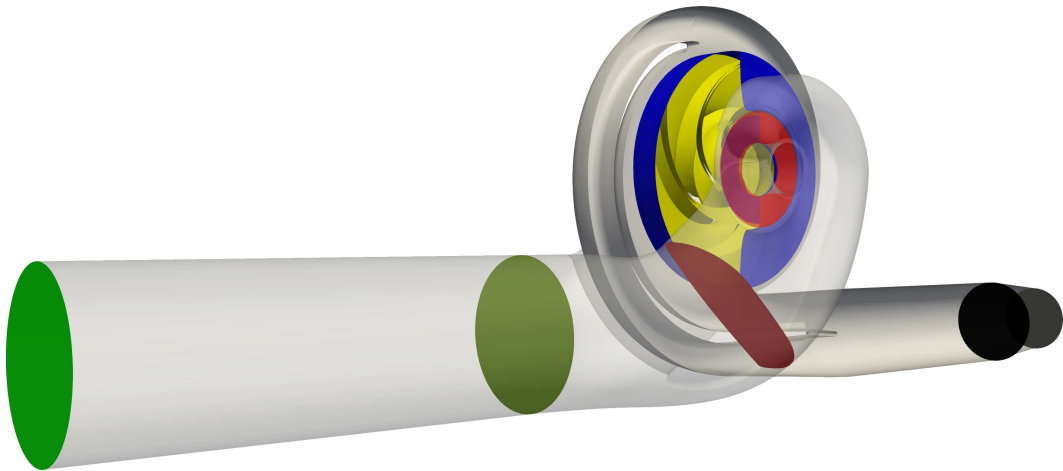


Figure 7.1: Boundary conditions. SIs are represented by *blue* and *red*, inlet is *green*, outlet is *gray*. Impeller parts are shown by *yellow*. The *grass green* and *black* are the surfaces, where pump efficiency is measured between

7.2 Mesh generation

The computational domain is divided into six parts (see Figure 7.2). One of the reasons is to connect the moving parts of the mesh to the rest. The other reason is that dividing the model at some places to split into NURBS patches, and connect them without having the same tangential parametrization. This makes the mesh generation process easier. Each patch is represented by two different colors. At least one of the colors is changed on the patch boundaries, which have C^0 continuity fashion. The number of control points and the number of elements used in the suction and outer volutes and around impeller are given in Table 7.1.

Table 7.1: Number of control points (nc) and elements (ne) in three different parts of the flow domain

Part	nc	ne
Suction casing	58,480	31,872
Outer volute	22,176	9,462
Impeller	73,680	30,854
Total	154,336	72,188

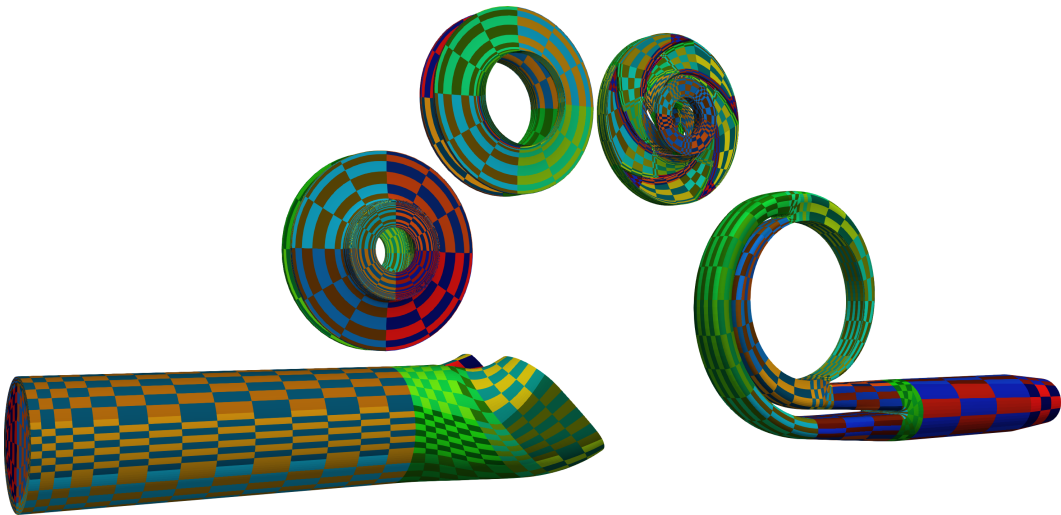


Figure 7.2: Parts of the mesh. The patching strategy. Please note that a part of the suction casing is not given because it is a confidential information. The mesh and parametrization in that part is also similar to the other parts which are given clearly

7.3 Computational conditions

The convective form of the ST-VMS (see Eq. (3.17)) is used for the computations. The rotation is employed with the mesh rotation in the IRF using the STNMUM. The time-step size is set to $\Delta t = \frac{T}{90}$ in the computations with all discharge values. Here T is the time period for a full rotation of the impeller. 500 GMRES iterations are performed per nonlinear iteration which is 3 per time step.

First, we computed the flow with $Q = Q_0$ keeping the impeller stationary until the flow reaches in a steady regime. This increases the stability of the computations in the first couple of cycles. Later we used this flow as initial condition and computed at least for $9T$ with seven different flow rates.

7.4 Flow development

In order to understand if our computations reach to a time-periodic solution, we calculated f -based Fourier decomposition of pressure at the point around the top tongue in outer volute as shown in Figure 7.3. A line is drawn from the center of the impeller tangent to the top tongue on the symmetry plane. Pressure is reduced in the middle of the intersection place and at the end point of the line. Figure 7.4 shows the f -based Fourier decomposition of pressure ($|(p)_f|/(\rho U^2)$) for six different cases. The time-periodic solution is reached after the first $3T$ mostly. However, as

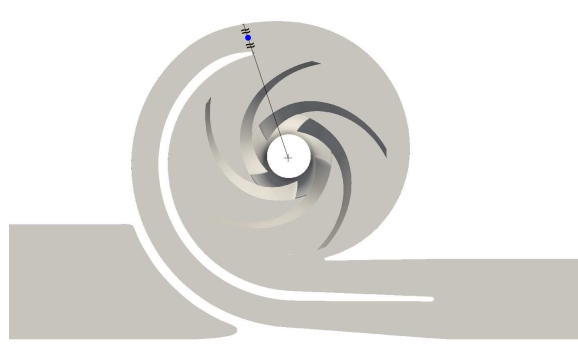


Figure 7.3: The point location used for f -based Fourier decomposition

expected, an unstable solution is observed with small discharge values in the first $6T$. Therefore, we found the time period in $(8T, 9T)$ safe for pump performance calculations.

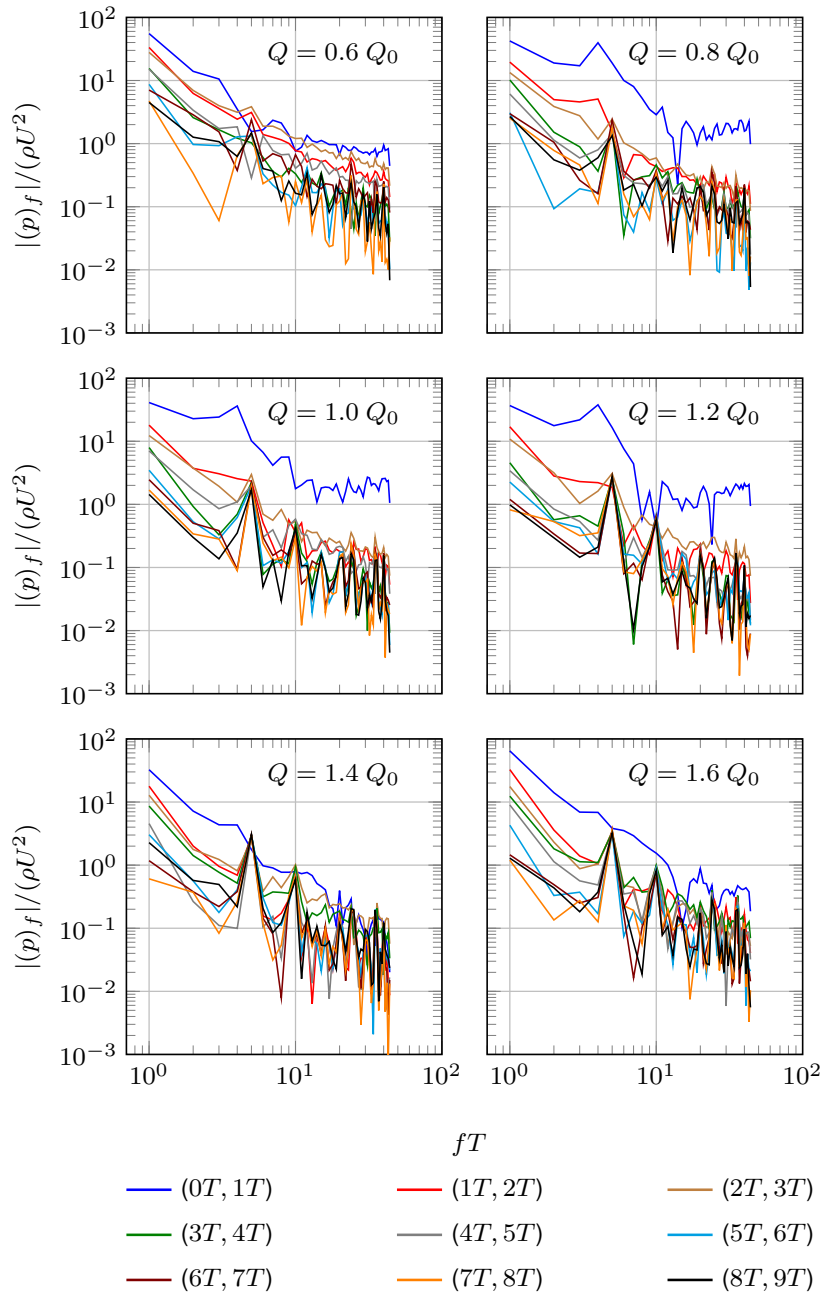


Figure 7.4: Flow development. f -based Fourier decomposition of $p/(\rho U^2)$

7.5 Pump performance

The shaft power P_S , hydraulic power P_H , and efficiency η are defined as follows:

$$P_S = 2\pi\Upsilon\omega, \quad (7.1)$$

$$P_H = \int_{\Gamma_{\text{inf}}} \mathbf{n} \cdot \mathbf{u} \left(\frac{1}{2}\rho\|\mathbf{u}\|^2 + p \right) d\Gamma + \int_{\Gamma_{\text{out}}} \mathbf{n} \cdot \mathbf{u} \left(\frac{1}{2}\rho\|\mathbf{u}\|^2 + p \right) d\Gamma, \quad (7.2)$$

$$\eta = \frac{P_H}{P_S}. \quad (7.3)$$

Subscripts “inf” and “out” represent the inflow and outflow surfaces, where pump performance is calculated between, as explained in Figure 7.1. The hydraulic head, h_H is defined as:

$$h_H = \frac{P_H}{Q\rho g}, \quad (7.4)$$

where g is the gravitational acceleration.

Figure 7.5 shows the pump performance calculated by different discharge values. The best efficiency point is plotted by the volumetric flow rate of $Q = Q_0$ as expected. The head is also computed inversely proportional to the flow rate as it is anticipated. Time average is taken in $\mathcal{T} = (8T, 9T)$. The results are given dividing by the reference performance values at $Q = Q_0$, and the computational pump head and efficiency differ smaller than 2 % from the reference values.

Figure 7.6 shows the shaft power, scaled with the experimental values ($P_{S_{\text{exp}}}$) at $Q = Q_0$, in $(8T, 9T)$ with seven different cases. At $Q = Q_0$, a good agreement is observed with the reference data. At the lower discharge values, it fluctuates strongly, possibly because of the flow separation as shown in Figure 7.8.

Head drop rate increases at higher values of discharge (see Figure 7.5). This behavior can also be seen in pressure distribution in Figure 7.7. The pressure change

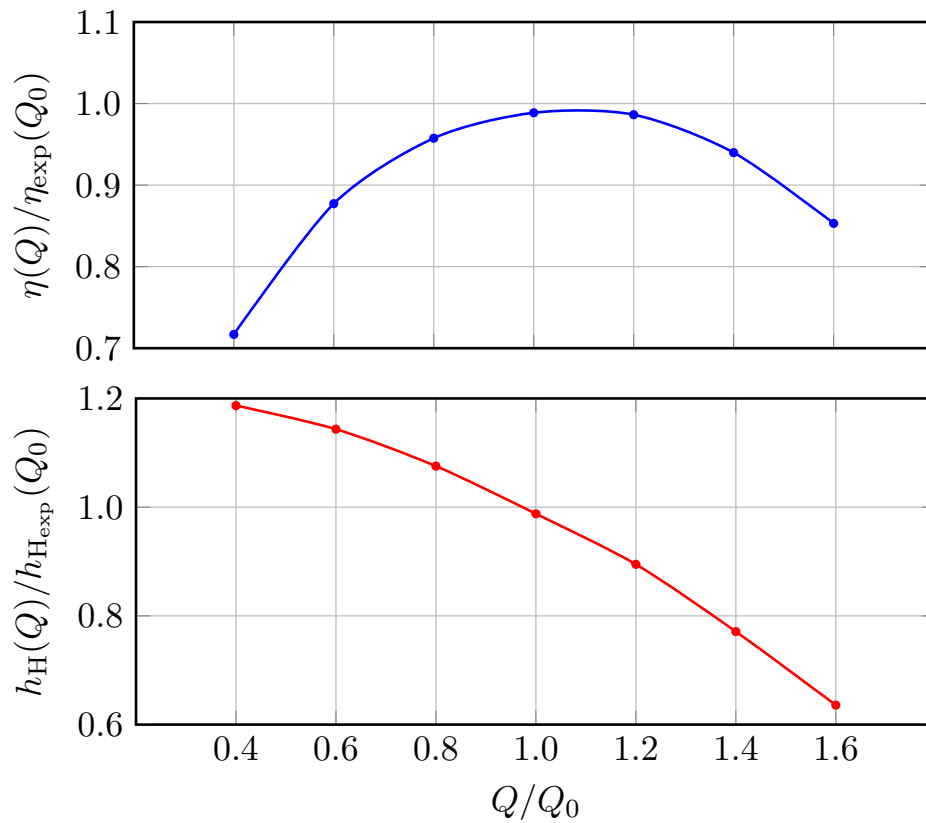


Figure 7.5: Pump efficiency (*blue*) and hydraulic head (*red*), scaled with the experimental values, with seven different volumetric flow rates. Time average is taken in $\mathcal{T} = (8T, 9T)$

is shown along the whole pump. According to this figure, the pressure (and the head loss) difference decreases by the raise of discharge. In Figure 7.8, the time-averaged streamlines around impeller are shown. It is clear that small volumetric flow rates cause large vortices around impeller.

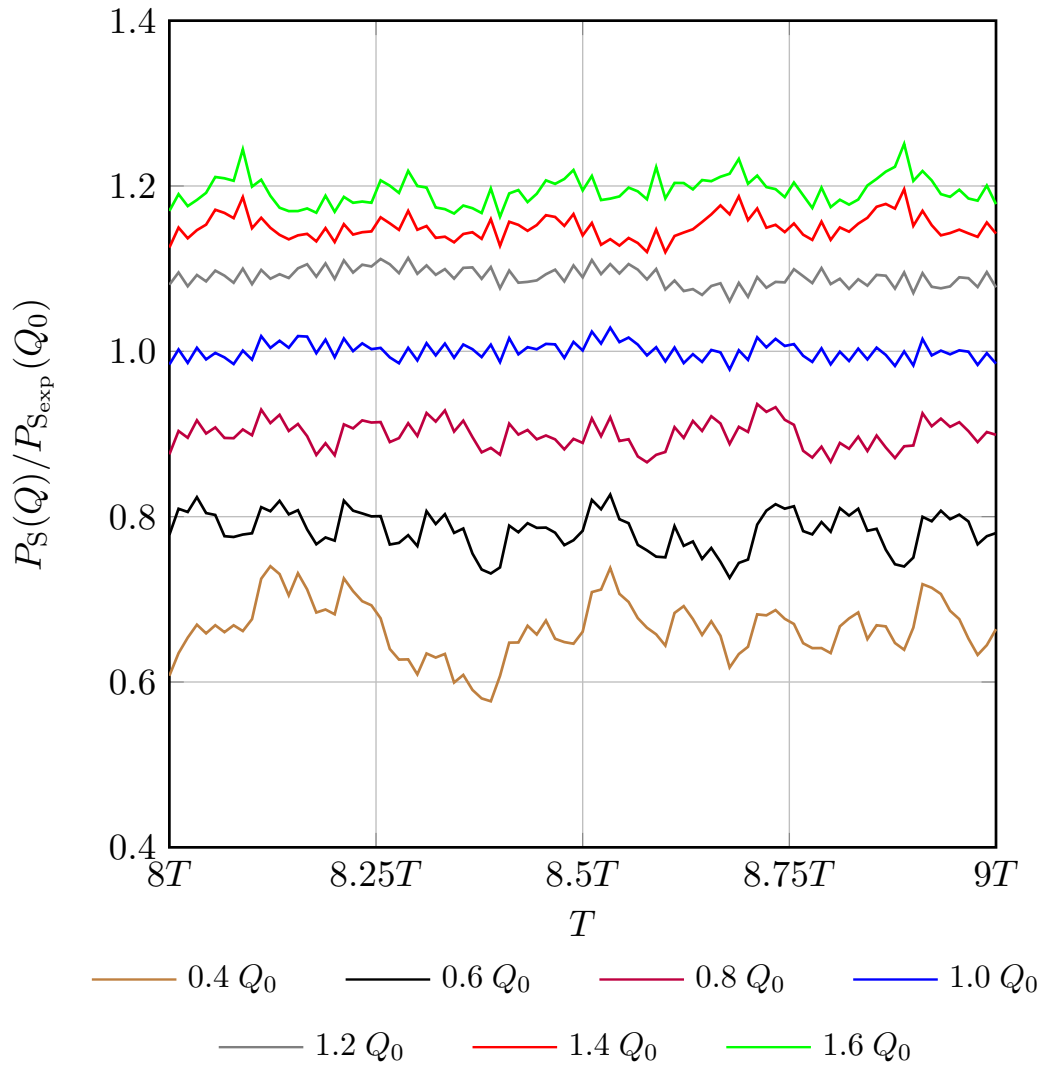


Figure 7.6: Shaft power, scaled with the experimental value, at $Q = Q_0$, by various volumetric flow rates in $(8T, 9T)$

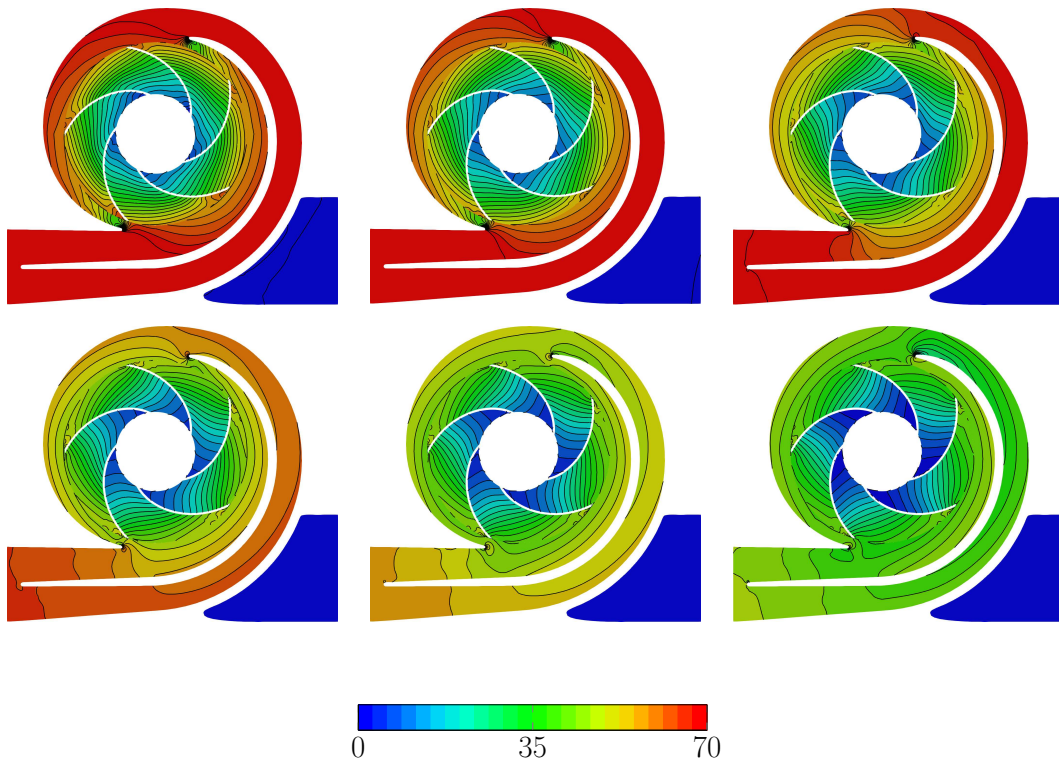


Figure 7.7: Time-averaged absolute pressure, $\bar{p}/(\rho U^2)$, on the symmetry plane. Computations with different discharge values of $Q = 0.4 Q, 0.6 Q, 0.8 Q, 1.0 Q, 1.2 Q$ and $1.4 Q$ are displayed from *left to right* and *top to bottom*. Results are averaged in $\mathcal{T} = (8T, 9T)$

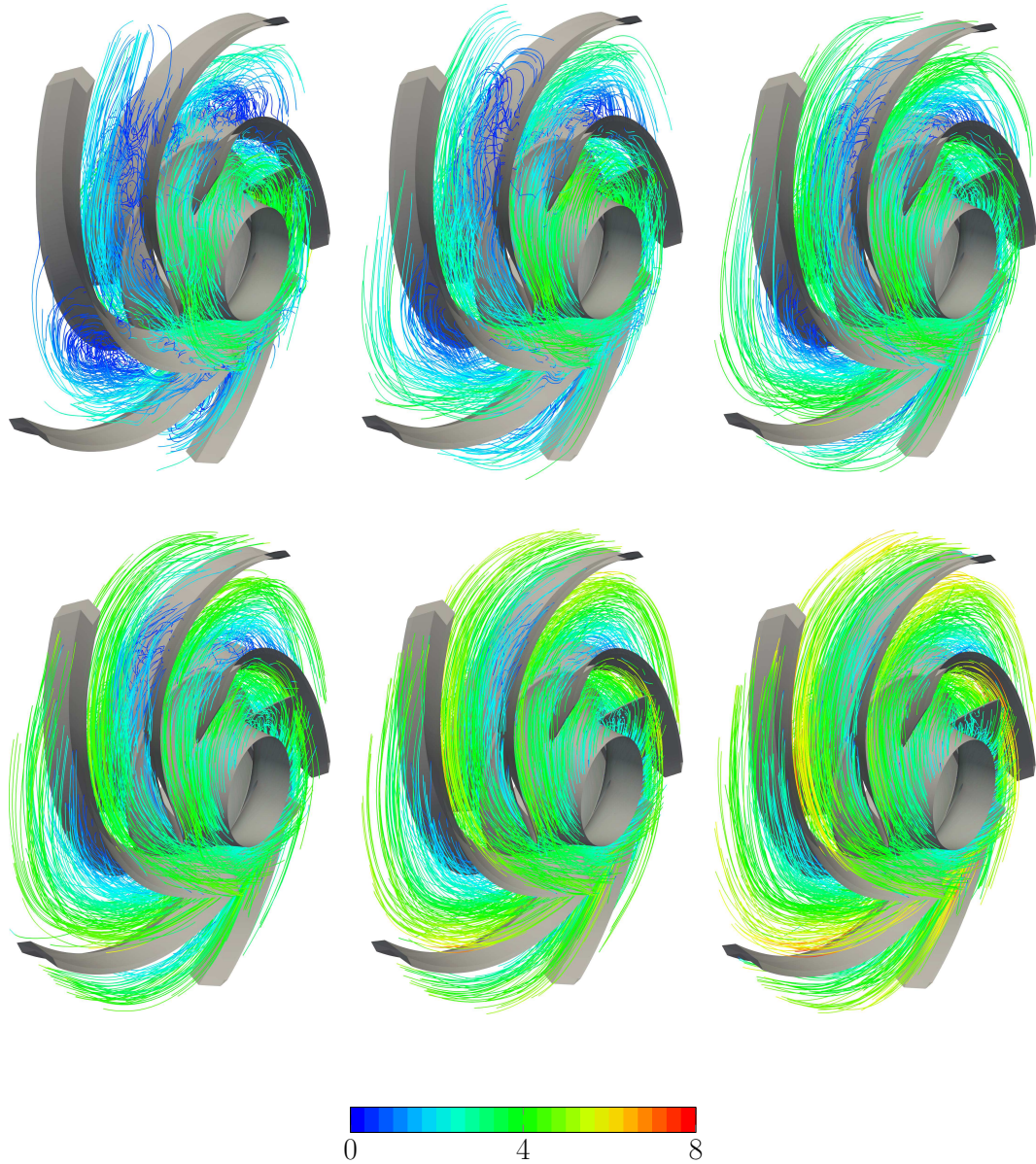


Figure 7.8: Time-averaged flow field around impeller by streamlines colored by velocity magnitude, $\|\bar{\mathbf{u}}_{\mathbf{R}}\|/U$. Streamlines and velocity magnitude are calculated relative to the impeller. Computations with different discharge values of $Q = 0.4 Q$, $0.6 Q$, $0.8 Q$, $1.0 Q$, $1.2 Q$ and $1.4 Q$ are displayed from *left to right* and *top to bottom*. Results are averaged in $\mathcal{T} = (8T, 9T)$

7.6 Flow around impeller in the NRF

Rotational-periodicity is explained in Chapter 2 and used in Chapter 6. Here we analyzed flow around one-fifth of the impeller blades (see Figure 7.9) with rotational-periodicity. We also used a slip condition to represent the symmetry in the axial direction. Figure 7.10 shows the boundary conditions enforced on the computational domain.

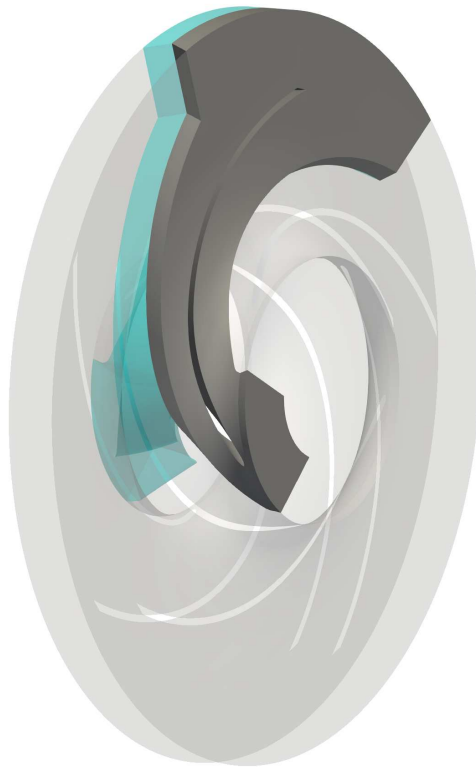


Figure 7.9: Computational domain

The coarse mesh used in this particular study is given in the computational domain in Figure 7.11. A refinement is performed around the blade, hub and shroud by the knot insertion algorithm as shown in Figure 7.11. The number of control points and elements are shown in Table 7.2.

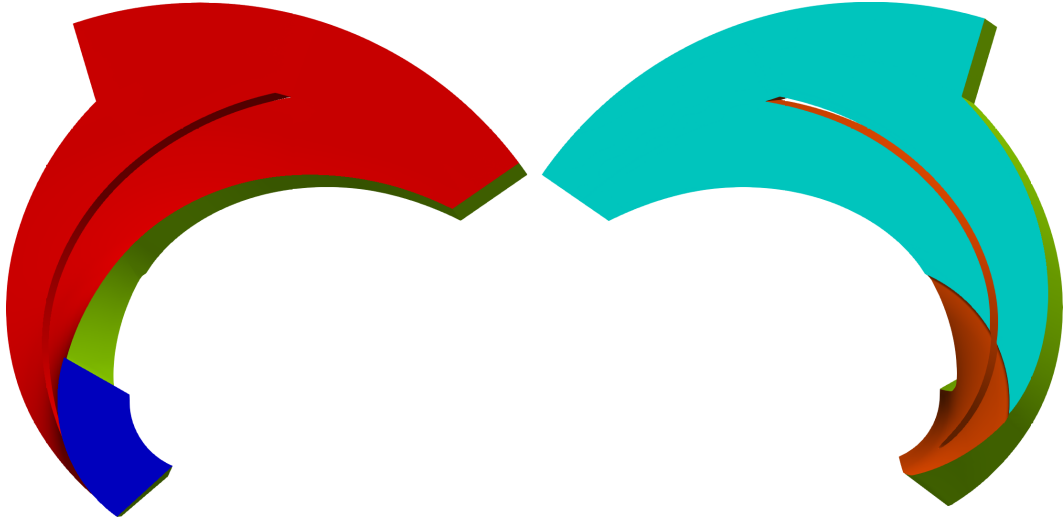


Figure 7.10: Boundary conditions. The *blue, red, green, cyan* shows the inflow, no-slip, periodic and slip boundaries

Table 7.2: Number of control points (nc) and elements (ne) in the coarse, medium and fine meshes

Mesh	nc	ne
Coarse	19,390	10,280
Medium	38,424	24,520
Fine	58,144	39,872

7.7 Results

The computations performed with the periodic blade is for $Q = Q_0$. The inflow velocity profile is extracted from the computations with the full-domain in $(10T, 15T)$ at the same discharge value. Here T is also defined for the one full rotation of the impeller in the actual situation as it is defined in the computations with the full-domain representation. We compute with the coarse mesh for $15T$ using the inflow profile ($5T$) three times periodically. Having computed far enough period of computations to reach a time-periodic solution, at $t = 12T$, the mesh is refined as shown in Figure 7.11 as well as data. In $(12T, 15T)$ period, we compute with both the coarse and finer meshes. Considering that the element with minimum size in streamwise direction is divided into two and four elements by knot-insertion algo-

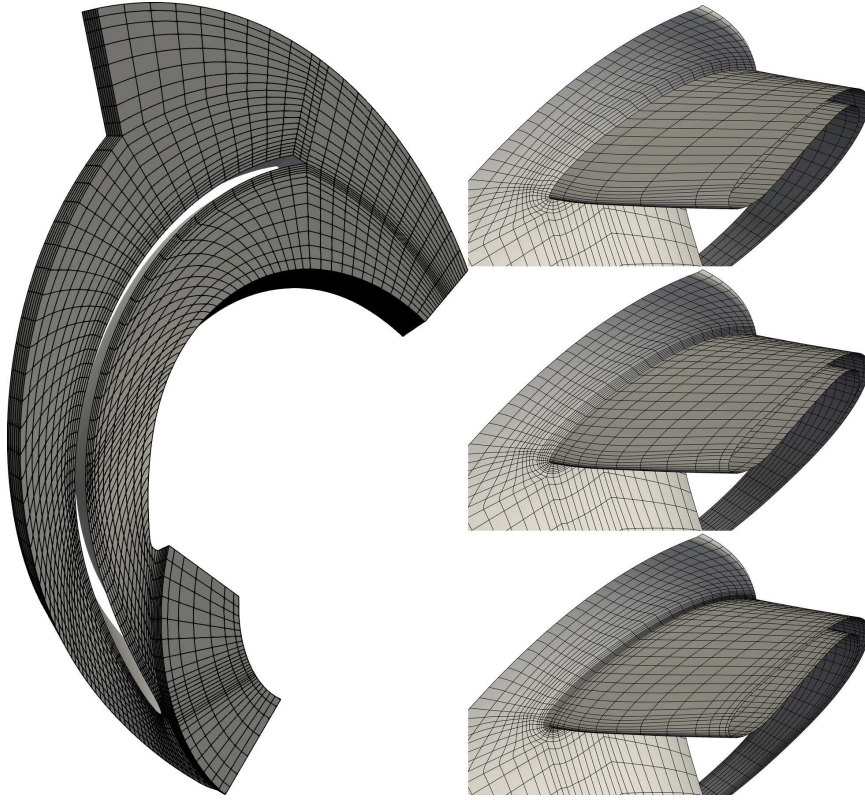


Figure 7.11: The coarse mesh around blade *left* and the mesh refinement *right*, the coarse, medium and fine meshes from *top* to *bottom*

rithm, the time-step sizes are set equivalent to 4° , 2° and 1° rotation per step of the impeller. The inflow profiles used in the computations with the medium and fine meshes are obtained interpolating the initial profile used for the coarse mesh in time considering the time-step size.

We show the shaft power with respect to the reference results in Table 7.3. Time average is taken in $\mathcal{T} = (14T, 15T)$.

Table 7.3: Shaft power (P_S), scaled with the experimental value ($P_{S_{\text{exp}}}$), at $Q = Q_0$. The values are averaged in $\mathcal{T} = (14T, 15T)$

Mesh	$P_S(Q_0)/P_{S_{\text{exp}}}(Q_0)$
Coarse	0.9425
Medium	0.9848
Fine	1.0167

Figure 7.12 shows the time-averaged streamlines colored by velocity magnitude.

Flow field is calculated relative to the impeller in this figure. Results are at $Q = Q_0$ and the pattern is in a good agreement with the results shown in Figure 7.8 from the solution computed using the full-domain.

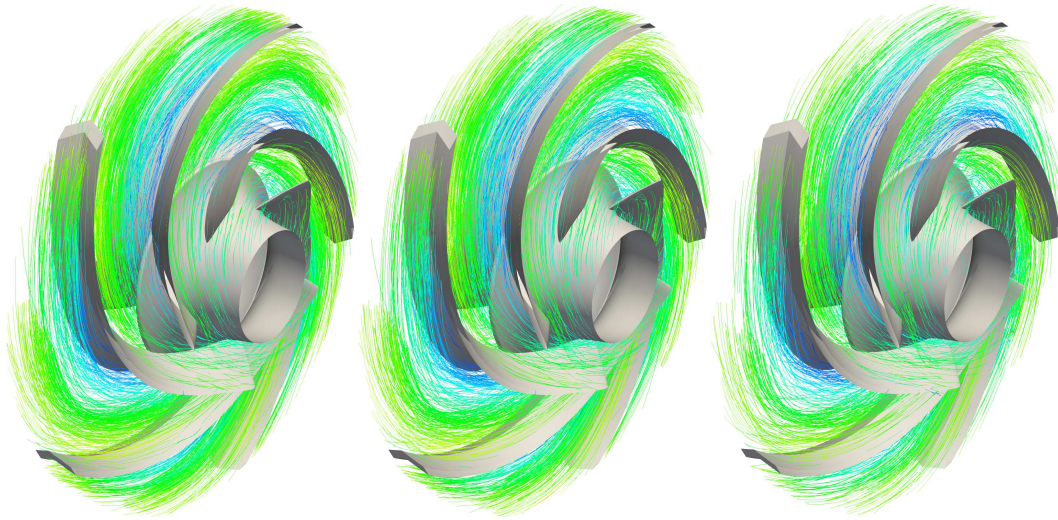


Figure 7.12: Time-averaged flow field around impeller by streamlines colored by velocity magnitude, $\|\bar{\mathbf{u}}_R\|/U$. Streamlines and velocity magnitude are calculated relative to the impeller. Results are obtained using the coarse, medium and fine meshes (from *left to right*) and averaged in $\mathcal{T} = (14T, 15T)$

Chapter 8

Concluding Remarks

CFD analysis of turbomachinery is challenging because of their complex geometries with high curvature and high Reynolds number causing secondary flows. To overcome the challenges involved in simulating this complex flow, accurate representations of the computational domain and motion of the rotating parts are essential. In this thesis, a computational method for high-fidelity turbomachinery flow analysis is developed, and the integration of this method with the existing ST methods is validated. Two essential challenges in turbomachinery flow computation are focused on. Firstly, the accuracy of the ST framework in turbulent-flow computations is shown with a high Reynolds number flow in a computational model with high curvature. Secondly, we focused on rotating computational models. The method developed during this research is used in computations with rotating boundaries and validated with the existing methods which are used for turbomachinery flows previously and provided good accuracy.

The ST-VMS with the ST isogeometric discretization has been tested using a known benchmark problem, U-duct turbulent-flow. It is a high Reynolds number flow, including high curvature geometry. These are the challenges in the problem. A fully-developed flow field in a straight duct was computed with periodicity condition and used as the inflow profile of the U-duct problem. The ST-IGA was used to enable the analysis with the exact representation of the arc in the model. It increased the accuracy of the solution. We calculated the time-averaged flow field and compared to experimental data. We investigated the effect of the time-averaging range, mesh refinement, and the Courant numbers. The flow development and the effect of the

averaging range were evaluated by the Fourier decomposition of the velocity in time. Furthermore, some qualitative analysis was performed by instantaneous and time-averaged velocity and pressure distributions. The isosurfaces of the second invariant of the velocity gradient tensor were used to visualize the flow, and separation around the curvature and recirculation were investigated. We concluded that the ST-VMS provides an accurate solution in turbulent-flow problems. The exact representation of the arc by NURBS increased accuracy.

For the second investigation about the turbomachinery flows, we focused on the computations with rotating domains. The Taylor–Couette flow, which is a classical fluid mechanics problem, was chosen for testing the ST-VMS method with isogeometric discretization both in the IRF and also in the NRF for the first time in the ST framework in this research. We performed the computational analysis with various combinations of the inner and outer cylinder angular velocities, resulting in three different flow patterns. Computations were conducted in the full-domain as well as three rotational-periodicity representations of the flow field. The conservative and nonconservative versions of the ST-VMS with two different enforcement of the prescribed cylinder velocities were tested with different mesh refinements. The ST isogeometric discretization was used to represent the circular geometry exactly. In the computations where the mesh is rotating, the STNMUM, with NURBS basis functions in time, enabled us to represent the mesh rotation exactly in terms of both the paths of the mesh points and the velocity of the points along their paths. The rotational-periodicity in the partial models was enforced with the ST-SI method. The flow development was examined by the Fourier analysis of the circumferential velocity fluctuations in time. Then, the effect of rotational-periodicity on the results was tested by Fourier analysis in space, comparing the circumferential velocity fluctuations with the full-domain computation results. Additionally, the flow patterns were evaluated by the ST-averaged velocity profiles. The instantaneous axial

velocity isosurfaces and velocity magnitude distributions were investigated. The angular momentum balance with torque acting on the solid boundaries was investigated for eight different combinations. All the formulations solved in this study were found globally angular momentum conservative in practice. All these methods in the ST framework, integrated together in the IRF and NRF, offered a high-fidelity computational analysis platform for this class of flow problems.

Finally, a sample turbomachinery flow analysis was shown. The ST framework was employed to calculate the flow dynamics in a double-suction centrifugal pump and its performance at various flow rate values. The representation of the complex curved geometry was one of the challenges in this study. The flow around the high-speed rotating parts and small-scale stationary parts, such as leakage flow, increases the difficulty. The pressure fluctuations occurring because of the rotating parts' relative motion with respect to the volute parts. The ST-VMS method with isogeometric discretization was used as the method to address these difficulties making the flow problem multiscale and unstable. The curved geometries were represented more accurately with the ST-IGA even in very coarse meshes. The mesh rotation was represented by the STNMUM exactly. Interaction between the meshes surrounding the rotating and stationary parts was provided by the ST-SI method. The flow dynamics around the rotating parts, and the double-suction centrifugal pump performance at seven different flow rates were calculated accurately with the integration of these methods. In addition to the computations with full-domain representation, one-fifth of the impeller blades were represented with rotational-periodicity. The flow around this periodic domain was computed in the NRF. The pump performance was compared with the experiments and a good agreement was observed in both the computations with full-domain representation and with the rotational-periodicity.

Appendix A

Stabilization Parameters and Element Lengths

A.1 Stabilization parameters

The stabilization parameters for the momentum equation τ_{SUPS} and the incompressibility constraint ν_{LSIC} are defined in different ways. Here, we define τ_{SUPS} mostly from [1, 2, 74]:

$$\tau_{\text{SUPS}} = (\tau_{\text{SUGN12}}^{-2} + \tau_{\text{SUGN3}}^{-2} + \tau_{\text{SUGN4}}^{-2})^{-\frac{1}{2}}. \quad (\text{A.1})$$

The first two terms are written as:

$$\tau_{\text{SUGN12}}^{-2} = \begin{bmatrix} 1 \\ \mathbf{u} \end{bmatrix} \begin{bmatrix} 1 \\ \mathbf{u} \end{bmatrix} : \mathbf{G}^{\text{ST}} \quad (\text{A.2})$$

and

$$\tau_{\text{SUGN3}}^{-1} = \nu \mathbf{r}_s \mathbf{r}_s : \mathbf{G}. \quad (\text{A.3})$$

Here, \mathbf{r}_s is the solution direction given by:

$$\mathbf{r}_s = \frac{\nabla \|\mathbf{u}\|}{\|\nabla \|\mathbf{u}\|\|}. \quad (\text{A.4})$$

Here \mathbf{G}^{ST} is the ST, and \mathbf{G} is the space-only element metric tensors. We write:

$$\mathbf{G}^{\text{ST}} = \left(\hat{\mathbf{Q}}^{\text{ST}}\right)^{-\top} \cdot \left(\hat{\mathbf{Q}}^{\text{ST}}\right)^{-1}, \quad (\text{A.5})$$

$$\mathbf{G} = \hat{\mathbf{Q}}^{-\top} \cdot \hat{\mathbf{Q}}^{-1}, \quad (\text{A.6})$$

where

$$\hat{\mathbf{Q}}^{\text{ST}} = \mathbf{Q}^{\text{ST}} \cdot \left(\mathbf{D}^{\text{ST}}\right)^{-1}, \quad (\text{A.7})$$

$$\hat{\mathbf{Q}} = \mathbf{Q} \cdot \mathbf{D}^{-1}. \quad (\text{A.8})$$

The consistent Jacobian tensors are written as follows:

$$\mathbf{Q}^{\text{ST}} = \begin{bmatrix} \frac{\partial t}{\partial \theta} & \frac{\partial t}{\partial \boldsymbol{\xi}} \\ \frac{\partial \mathbf{x}}{\partial \theta} & \mathbf{Q} \end{bmatrix} \quad (\text{A.9})$$

and

$$\mathbf{Q} = \frac{\partial \mathbf{x}}{\partial \boldsymbol{\xi}}, \quad (\text{A.10})$$

where θ is the temporal and $\boldsymbol{\xi}$ is the spatial parametric coordinates. The transformation tensor is defined as follows:

$$\mathbf{D}^{\text{ST}} = \begin{bmatrix} D_\theta & \mathbf{0}^\top \\ \mathbf{0} & \mathbf{D} \end{bmatrix}. \quad (\text{A.11})$$

The definitions used for D_θ and \mathbf{D} play an important role, especially for higher-order isogeometric discretization [74, 75] and simplex elements [87]. In this dissertation, $D_\theta = 1$ and we set \mathbf{D} to its ‘‘RQD-MAX’’ version [75].

The third component, originating from [52], is written as:

$$\tau_{\text{SUGN4}} = \left\| \nabla \mathbf{u}^h \right\|_F^{-1}, \quad (\text{A.12})$$

where $\| \cdot \|_F$ is the Frobenius norm.

The stabilization parameter ν_{LSIC} associated with the incompressibility constraint is given in [18] as follows:

$$\nu_{\text{LSIC}} = \frac{h_{\text{LSIC}}^2}{\tau_{\text{SUPS}}}. \quad (\text{A.13})$$

A.2 Element lengths

In Eq. (A.13), h_{LSIC} is set equal to the minimum element length h_{MIN} which is given:

$$h_{\text{MIN}} = 2 \left(\max_{\mathbf{r}_s} (\mathbf{r}_s \mathbf{r}_s : \mathbf{G}) \right)^{-\frac{1}{2}}. \quad (\text{A.14})$$

The element length used in the ST-SI, in Eqs. (3.18) and (3.23) is written as:

$$h = \left(\frac{h_{\text{B}}^{-2} + h_{\text{A}}^{-2}}{2} \right)^{-\frac{1}{2}}, \quad (\text{A.15})$$

$$h_{\text{B}} = 2 (\mathbf{n}_{\text{B}} \mathbf{n}_{\text{B}} : \mathbf{G})^{-\frac{1}{2}} \quad (\text{for Side B}), \quad (\text{A.16})$$

$$h_{\text{A}} = 2 (\mathbf{n}_{\text{A}} \mathbf{n}_{\text{A}} : \mathbf{G})^{-\frac{1}{2}} \quad (\text{for Side A}), \quad (\text{A.17})$$

$$\hat{\mathbf{n}}_{\text{B}} = \frac{\mathbf{n}_{\text{B}} - \mathbf{n}_{\text{A}}}{\|\mathbf{n}_{\text{B}} - \mathbf{n}_{\text{A}}\|}. \quad (\text{A.18})$$

Appendix B

Path Representation

Most of the information in this section is written from [2, 3, 13, 15]. The exact representation of a circular-arc path and a prescribed velocity along that path is possible when the mesh is rotating with the secondary mappings Θ_t and Θ_x based on quadratic NURBS basis functions in time.

B.1 A circular-arc path

A circular-arc path of a moving point can be represented exactly by NURBS basis functions in time. Let us assume the point moves from \mathbf{x}^1 to \mathbf{x}^3 , with $\|\mathbf{x}^1\| = \|\mathbf{x}^3\|$, as shown in Figure B.1. Similar to arc representation in space given in Section 3.4.1, a circular-arc path can also be represented exactly by quadratic NURBS basis functions in time with three control points if $q < \frac{\pi}{2}$. The NURBS weights are

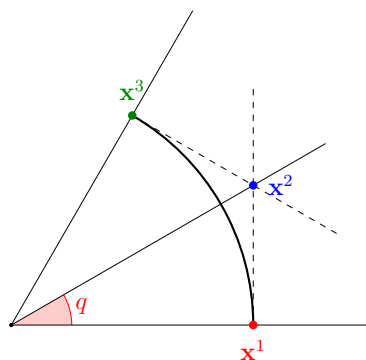


Figure B.1: A circular-arc path represented exactly by a quadratic NURBS element in time. This figure was also shown in [2]

$w^1 = w^3 = 1$, and $w^2 = \cos q$, where

$$\cos 2q = \frac{\mathbf{x}^1 \cdot \mathbf{x}^3}{r^2}, \quad r = \|\mathbf{x}^1\| = \|\mathbf{x}^3\|. \quad (\text{B.1})$$

This results in the temporal basis functions

$$T^1(\Theta) = \frac{(1 - \Theta)^2}{2((1 + \Theta^2) + w^2(1 - \Theta^2))}, \quad (\text{B.2})$$

$$T^2(\Theta) = \frac{w^2(1 - \Theta^2)}{(1 + \Theta^2) + w^2(1 - \Theta^2)}, \quad (\text{B.3})$$

$$T^3(\Theta) = \frac{(1 + \Theta)^2}{2((1 + \Theta^2) + w^2(1 - \Theta^2))}. \quad (\text{B.4})$$

and the control points are \mathbf{x}^1 ,

$$\mathbf{x}^2 = \frac{r}{w^2} \frac{\mathbf{x}^1 + \mathbf{x}^3}{\|\mathbf{x}^1 + \mathbf{x}^3\|} \quad (\text{B.5})$$

$$= \frac{1}{2(w^2)^2} (\mathbf{x}^1 + \mathbf{x}^3), \quad (\text{B.6})$$

and \mathbf{x}^3 . Therefore, the arc is represented as follows:

$$\mathbf{x}(\Theta_{\mathbf{x}}) = \mathbf{x}^1 T^1(\Theta_{\mathbf{x}}) + \mathbf{x}^2 T^2(\Theta_{\mathbf{x}}) + \mathbf{x}^3 T^3(\Theta_{\mathbf{x}}). \quad (\text{B.7})$$

In case a constant angular velocity, by combining Eqs. (B.6) and (B.7), we can write as:

$$\mathbf{x}(\Theta_{\mathbf{x}}) = \underbrace{\left(T^1(\Theta_{\mathbf{x}}) + \frac{1}{2w_2^2} T^2(\Theta_{\mathbf{x}}) \right)}_{Q^1(\Theta_{\mathbf{x}})} \mathbf{x}^1 + \underbrace{\left(T^3(\Theta_{\mathbf{x}}) + \frac{1}{2w_2^2} T^2(\Theta_{\mathbf{x}}) \right)}_{Q^3(\Theta_{\mathbf{x}})} \mathbf{x}^3, \quad (\text{B.8})$$

where Q^1 and Q^3 are introduced for notation convenience. Taking the cross product

with the unit vector along \mathbf{x}^2 , we get

$$\frac{\mathbf{x}^1 + \mathbf{x}^3}{\|\mathbf{x}^1 + \mathbf{x}^3\|} \times \mathbf{x}(\Theta_{\mathbf{x}}) = \frac{\mathbf{x}^1 \times \mathbf{x}^3}{r^2 \sin(2q)} r \sin(\omega t), \quad (\text{B.9})$$

where

$$-\frac{\Delta t}{2} \leq t \leq \frac{\Delta t}{2}, \quad (\text{B.10})$$

and $\omega \Delta t = 2q$ for notation convenience. From Eq. (B.9), we get

$$\frac{\mathbf{x}^1 + \mathbf{x}^3}{2r \cos q} \times \mathbf{x}(\Theta_{\mathbf{x}}) = \frac{\mathbf{x}^1 \times \mathbf{x}^3}{2r \sin q \cos q} \sin(\omega t). \quad (\text{B.11})$$

From Eqs. (B.8) and (B.11), we write as:

$$Q^3 - Q^1 = \frac{\sin(\omega t)}{\sin q}. \quad (\text{B.12})$$

From Eq. (B.12), it is written that

$$\Theta_{\mathbf{x}} = \frac{\sin q}{1 - \cos q} \frac{\sin(\omega t)}{1 + \cos(\omega t)}. \quad (\text{B.13})$$

Assuming time is represented with the same basis functions, we can write

$$t(\Theta_t) = \frac{\Delta t}{2} (T^3(\Theta_t) - T^1(\Theta_t)) \quad (\text{B.14})$$

$$= \frac{\Delta t \Theta_t}{1 + \Theta_t^2 + (1 - \Theta_t^2) \cos q}. \quad (\text{B.15})$$

Selecting $\frac{dt}{d\theta} = \frac{\Delta t}{2}$ and with Eq. (B.10), we achieve $t = \frac{\Delta t}{2} \theta$. We solve Eq. (B.15)

with that on the left-hand side, and obtain Θ_t as a function of θ :

$$\Theta_t(\theta) = \frac{\theta(1 + \cos q)}{1 + \sqrt{1 - (\theta \sin q)^2}}. \quad (\text{B.16})$$

Differentiating that with respect to θ , we reach

$$\frac{d\Theta_t}{d\theta} = \frac{1 + \cos q}{\sqrt{1 - (\theta \sin q)^2} \left(1 + \sqrt{1 - (\theta \sin q)^2}\right)}. \quad (\text{B.17})$$

For the circular-arc path of the moving point, the secondary mapping becomes

$$\Theta_{\mathbf{x}} = \frac{\sin q}{1 - \cos q} \frac{\sin(q\theta)}{1 + \cos(q\theta)}, \quad (\text{B.18})$$

and we can write

$$\frac{d\Theta_{\mathbf{x}}}{d\theta} = \frac{\sin q}{1 - \cos q} \frac{1}{1 + \cos(q\theta)} q. \quad (\text{B.19})$$

With this, the velocity of the point is obtained exactly as

$$\mathbf{v}(\theta) = \frac{d\mathbf{x}}{d\Theta_{\mathbf{x}}} \frac{d\Theta_{\mathbf{x}}}{d\theta} \frac{2}{\Delta t}. \quad (\text{B.20})$$

B.2 Prescribed velocity in the ST domain

The rotation-generated velocity can also be prescribed exactly along the circular path. Assuming we have a set of control points \mathbf{x}_a^α with corresponding basis functions T^α and N_a , a position in the ST domain is given with

$$\mathbf{x}^h(\theta, \xi) = \sum_{\alpha=1}^3 \sum_{a=1}^3 T^\alpha(\Theta_{\mathbf{x}}(\theta)) N_a(\xi) \mathbf{x}_a^\alpha. \quad (\text{B.21})$$

From that, we can write the prescribed velocity as follows:

$$\mathbf{g}^h(\theta, \xi) = \boldsymbol{\omega} \times \mathbf{x}^h(\theta, \xi) \quad (\text{B.22})$$

$$= \boldsymbol{\omega} \times \sum_{\alpha=1}^3 \sum_{a=1}^3 T^\alpha(\Theta_{\mathbf{x}}(\theta)) N_a(\xi) \mathbf{x}_a^\alpha \quad (\text{B.23})$$

$$= \sum_{\alpha=1}^3 \sum_{a=1}^3 T^\alpha(\Theta_{\mathbf{x}}(\theta)) N_a(\xi) (\boldsymbol{\omega} \times \mathbf{x}_a^\alpha). \quad (\text{B.24})$$

This implies $\mathbf{g}^h(\theta, \xi) = \sum_{\alpha=1}^3 \sum_{a=1}^3 T^\alpha(\Theta_{\mathbf{x}}(\theta)) N_a(\xi) \mathbf{g}_a^\alpha$, where

$$\mathbf{g}_a^\alpha = \boldsymbol{\omega} \times \mathbf{x}_a^\alpha. \quad (\text{B.25})$$

The exact representation of the prescribed velocity is also possible when the mesh is rotating with Θ_t and $\Theta_{\mathbf{x}}$. On the other hand, if the flow solution is based on linear functions in time, the representation of the prescribed velocity is not exact in the flow solution. This would cause lower accuracy at higher rotation angles per time step.

Bibliography

- [1] L. Aydinbakar, K. Takizawa, T.E. Tezduyar, and D. Matsuda, “U-duct turbulent-flow computation with the ST-VMS method and isogeometric discretization”, *Computational Mechanics*, published online, DOI: 10.1007/s00466-020-01965-4, February 2021, doi:10.1007/s00466-020-01965-4.
- [2] L. Aydinbakar, K. Takizawa, T.E. Tezduyar, and T. Kuraishi, “Space–time VMS isogeometric analysis of the Taylor–Couette flow”, to appear in *Computational Mechanics*, 2021.
- [3] Y. Bazilevs, K. Takizawa, and T.E. Tezduyar, *Computational Fluid–Structure Interaction: Methods and Applications*. Wiley, February 2013, ISBN 978-0470978771.
- [4] T.J.R. Hughes, *The Finite Element Method: Linear Static and Dynamic Finite Element Analysis*. Dover Publications, 2000, ISBN 978-0486411811.
- [5] T.J.R. Hughes, J.A. Cottrell, and Y. Bazilevs, “Isogeometric analysis: CAD, finite elements, NURBS, exact geometry, and mesh refinement”, *Computer Methods in Applied Mechanics and Engineering*, **194** (2005) 4135–4195.
- [6] W.T.L. Piegl, *The NURBS book*. Springer, 1997.
- [7] T.E. Tezduyar, M. Behr, and J. Liou, “A new strategy for finite element computations involving moving boundaries and interfaces – the deforming-spatial-domain/space–time procedure: I. The concept and the preliminary numerical tests”, *Computer Methods in Applied Mechanics and Engineering*, **94** (3) (1992) 339–351, doi:10.1016/0045-7825(92)90059-S.

- [8] T.E. Tezduyar and K. Takizawa, “Space–time computations in practical engineering applications: A summary of the 25-year history”, *Computational Mechanics*, **63** (2019) 747–753, doi:10.1007/s00466-018-1620-7.
- [9] K. Takizawa and T.E. Tezduyar, “Computational methods for parachute fluid–structure interactions”, *Archives of Computational Methods in Engineering*, **19** (2012) 125–169, doi:10.1007/s11831-012-9070-4.
- [10] K. Takizawa and T.E. Tezduyar, “Multiscale space–time fluid–structure interaction techniques”, *Computational Mechanics*, **48** (2011) 247–267, doi:10.1007/s00466-011-0571-z.
- [11] K. Takizawa, T.E. Tezduyar, H. Mochizuki, H. Hattori, S. Mei, L. Pan, and K. Montel, “Space–time VMS method for flow computations with slip interfaces (ST-SI)”, *Mathematical Models and Methods in Applied Sciences*, **25** (2015) 2377–2406, doi:10.1142/S0218202515400126.
- [12] K. Takizawa, T.E. Tezduyar, S. Asada, and T. Kuraishi, “Space–time method for flow computations with slip interfaces and topology changes (ST-SI-TC)”, *Computers & Fluids*, **141** (2016) 124–134, doi:10.1016/j.compfluid.2016.05.006.
- [13] K. Takizawa and T.E. Tezduyar, “Space–time fluid–structure interaction methods”, *Mathematical Models and Methods in Applied Sciences*, **22** (supp02) (2012) 1230001, doi:10.1142/S0218202512300013.
- [14] Y. Otaguro, *Space–Time Computational Methods and Isogeometric Discretization for Flow Problems with Complex Geometries and Moving Boundaries and Interfaces*, Ph.D. thesis, Waseda University, 2018.
- [15] K. Takizawa, B. Henicke, A. Puntel, T. Spielman, and T.E. Tezduyar, “Space–time computational techniques for the aerodynamics of flapping wings”, *Journal of Applied Mechanics*, **79** (2012) 010903, doi:10.1115/1.4005073.

- [16] K. Takizawa, B. Henicke, A. Puntel, N. Kostov, and T.E. Tezduyar, “Space–time techniques for computational aerodynamics modeling of flapping wings of an actual locust”, *Computational Mechanics*, **50** (2012) 743–760, doi:10.1007/s00466-012-0759-x.
- [17] K. Takizawa, N. Kostov, A. Puntel, B. Henicke, and T.E. Tezduyar, “Space–time computational analysis of bio-inspired flapping-wing aerodynamics of a micro aerial vehicle”, *Computational Mechanics*, **50** (2012) 761–778, doi:10.1007/s00466-012-0758-y.
- [18] K. Takizawa, T.E. Tezduyar, S. McIntyre, N. Kostov, R. Kolesar, and C. Habluetzel, “Space–time VMS computation of wind-turbine rotor and tower aerodynamics”, *Computational Mechanics*, **53** (2014) 1–15, doi:10.1007/s00466-013-0888-x.
- [19] T. Kuraishi, K. Takizawa, and T.E. Tezduyar, “Tire aerodynamics with actual tire geometry, road contact and tire deformation”, *Computational Mechanics*, **63** (2019) 1165–1185, doi:10.1007/s00466-018-1642-1.
- [20] Y. Bazilevs and T.J.R. Hughes, “Weak imposition of Dirichlet boundary conditions in fluid mechanics”, *Computers and Fluids*, **36** (2007) 12–26.
- [21] A.N. Brooks and T.J.R. Hughes, “Streamline upwind/Petrov-Galerkin formulations for convection dominated flows with particular emphasis on the incompressible Navier-Stokes equations”, *Computer Methods in Applied Mechanics and Engineering*, **32** (1982) 199–259.
- [22] T.E. Tezduyar, “Stabilized finite element formulations for incompressible flow computations”, *Advances in Applied Mechanics*, **28** (1992) 1–44, doi:10.1016/S0065-2156(08)70153-4.

- [23] T.E. Tezduyar, S. Mittal, S.E. Ray, and R. Shih, “Incompressible flow computations with stabilized bilinear and linear equal-order-interpolation velocity-pressure elements”, *Computer Methods in Applied Mechanics and Engineering*, **95** (1992) 221–242, doi:10.1016/0045-7825(92)90141-6.
- [24] T.J.R. Hughes, “Multiscale phenomena: Green’s functions, the Dirichlet-to-Neumann formulation, subgrid scale models, bubbles, and the origins of stabilized methods”, *Computer Methods in Applied Mechanics and Engineering*, **127** (1995) 387–401.
- [25] T.J.R. Hughes, W.K. Liu, and T.K. Zimmermann, “Lagrangian–Eulerian finite element formulation for incompressible viscous flows”, *Computer Methods in Applied Mechanics and Engineering*, **29** (1981) 329–349.
- [26] Y. Bazilevs, V.M. Calo, T.J.R. Hughes, and Y. Zhang, “Isogeometric fluid–structure interaction: theory, algorithms, and computations”, *Computational Mechanics*, **43** (2008) 3–37.
- [27] K. Takizawa, Y. Bazilevs, and T.E. Tezduyar, “Space–time and ALE-VMS techniques for patient-specific cardiovascular fluid–structure interaction modeling”, *Archives of Computational Methods in Engineering*, **19** (2012) 171–225, doi:10.1007/s11831-012-9071-3.
- [28] Y. Bazilevs, K. Takizawa, and T.E. Tezduyar, “New directions and challenging computations in fluid dynamics modeling with stabilized and multiscale methods”, *Mathematical Models and Methods in Applied Sciences*, **25** (2015) 2217–2226, doi:10.1142/S0218202515020029.
- [29] A. Korobenko, Y. Bazilevs, K. Takizawa, and T.E. Tezduyar, “Computer modeling of wind turbines: 1. ALE-VMS and ST-VMS aerodynamic and FSI analysis”, *Archives of Computational Methods in Engineering*, **26** (2019) 1059–1099,

doi:10.1007/s11831-018-9292-1.

- [30] K. Takizawa, T.E. Tezduyar, and N. Kostov, “Sequentially-coupled space–time FSI analysis of bio-inspired flapping-wing aerodynamics of an MAV”, *Computational Mechanics*, **54** (2014) 213–233, doi:10.1007/s00466-014-0980-x.
- [31] K. Takizawa, Y. Bazilevs, T.E. Tezduyar, M.-C. Hsu, O. Øiseth, K.M. Mathisen, N. Kostov, and S. McIntyre, “Engineering analysis and design with ALE-VMS and space–time methods”, *Archives of Computational Methods in Engineering*, **21** (2014) 481–508, doi:10.1007/s11831-014-9113-0.
- [32] K. Takizawa, D. Montes, S. McIntyre, and T.E. Tezduyar, “Space–time VMS methods for modeling of incompressible flows at high Reynolds numbers”, *Mathematical Models and Methods in Applied Sciences*, **23** (2013) 223–248, doi:10.1142/s0218202513400022.
- [33] K. Takizawa, B. Henicke, D. Montes, T.E. Tezduyar, M.-C. Hsu, and Y. Bazilevs, “Numerical-performance studies for the stabilized space–time computation of wind-turbine rotor aerodynamics”, *Computational Mechanics*, **48** (2011) 647–657, doi:10.1007/s00466-011-0614-5.
- [34] T.E. Tezduyar, M. Behr, S. Mittal, and J. Liou, “A new strategy for finite element computations involving moving boundaries and interfaces – the deforming-spatial-domain/space–time procedure: II. Computation of free-surface flows, two-liquid flows, and flows with drifting cylinders”, *Computer Methods in Applied Mechanics and Engineering*, **94** (3) (1992) 353–371, doi:10.1016/0045-7825(92)90060-W.
- [35] T.E. Tezduyar, “Computation of moving boundaries and interfaces and stabilization parameters”, *International Journal for Numerical Methods in Fluids*, **43** (2003) 555–575, doi:10.1002/flid.505.

- [36] T.E. Tezduyar and S. Sathe, “Modeling of fluid–structure interactions with the space–time finite elements: Solution techniques”, *International Journal for Numerical Methods in Fluids*, **54** (2007) 855–900, doi:10.1002/fld.1430.
- [37] Y. Bazilevs, M.-C. Hsu, I. Akkerman, S. Wright, K. Takizawa, B. Henicke, T. Spielman, and T.E. Tezduyar, “3D simulation of wind turbine rotors at full scale. Part I: Geometry modeling and aerodynamics”, *International Journal for Numerical Methods in Fluids*, **65** (2011) 207–235, doi:10.1002/fld.2400.
- [38] K. Takizawa, C. Moorman, S. Wright, T. Spielman, and T.E. Tezduyar, “Fluid–structure interaction modeling and performance analysis of the Orion spacecraft parachutes”, *International Journal for Numerical Methods in Fluids*, **65** (2011) 271–285, doi:10.1002/fld.2348.
- [39] K. Takizawa, S. Wright, C. Moorman, and T.E. Tezduyar, “Fluid–structure interaction modeling of parachute clusters”, *International Journal for Numerical Methods in Fluids*, **65** (2011) 286–307, doi:10.1002/fld.2359.
- [40] K. Takizawa, B. Henicke, T.E. Tezduyar, M.-C. Hsu, and Y. Bazilevs, “Stabilized space–time computation of wind-turbine rotor aerodynamics”, *Computational Mechanics*, **48** (2011) 333–344, doi:10.1007/s00466-011-0589-2.
- [41] K. Takizawa, T.E. Tezduyar, Y. Otoguro, T. Terahara, T. Kuraishi, and H. Hattori, “Turbocharger flow computations with the Space–Time Iso-geometric Analysis (ST-IGA)”, *Computers & Fluids*, **142** (2017) 15–20, doi:10.1016/j.compfluid.2016.02.021.
- [42] Y. Bazilevs, K. Takizawa, T.E. Tezduyar, M.-C. Hsu, N. Kostov, and S. McIntyre, “Aerodynamic and FSI analysis of wind turbines with the ALE-VMS and ST-VMS methods”, *Archives of Computational Methods in Engineering*, **21** (2014) 359–398, doi:10.1007/s11831-014-9119-7.

- [43] Y. Otoguro, K. Takizawa, and T.E. Tezduyar, “Space–time VMS computational flow analysis with isogeometric discretization and a general-purpose NURBS mesh generation method”, *Computers & Fluids*, **158** (2017) 189–200, doi:10.1016/j.compfluid.2017.04.017.
- [44] Y. Otoguro, K. Takizawa, T.E. Tezduyar, K. Nagaoka, and S. Mei, “Turbocharger turbine and exhaust manifold flow computation with the Space–Time Variational Multiscale Method and Isogeometric Analysis”, *Computers & Fluids*, **179** (2019) 764–776, doi:10.1016/j.compfluid.2018.05.019.
- [45] Y. Otoguro, K. Takizawa, T.E. Tezduyar, K. Nagaoka, R. Avsar, and Y. Zhang, “Space–time VMS flow analysis of a turbocharger turbine with isogeometric discretization: Computations with time-dependent and steady-inflow representations of the intake/exhaust cycle”, *Computational Mechanics*, **64** (2019) 1403–1419, doi:10.1007/s00466-019-01722-2.
- [46] Y. Otoguro, H. Mochizuki, K. Takizawa, and T.E. Tezduyar, “Space–time variational multiscale isogeometric analysis of a tsunami-shelter vertical-axis wind turbine”, *Computational Mechanics*, **66** (2020) 1443–1460, doi:10.1007/s00466-020-01910-5.
- [47] K. Takizawa, T.E. Tezduyar, and H. Hattori, “Computational analysis of flow-driven string dynamics in turbomachinery”, *Computers & Fluids*, **142** (2017) 109–117, doi:10.1016/j.compfluid.2016.02.019.
- [48] K. Komiya, T. Kanai, Y. Otoguro, M. Kaneko, K. Hirota, Y. Zhang, K. Takizawa, T.E. Tezduyar, M. Nohmi, T. Tsuneda, M. Kawai, and M. Isono, “Computational analysis of flow-driven string dynamics in a pump and residence time calculation”, *IOP conference series earth and environmental science*, **240** (2019) 062014, doi:10.1088/1755-1315/240/6/062014.

- [49] T. Kanai, K. Takizawa, T.E. Tezduyar, K. Komiya, M. Kaneko, K. Hirota, M. Nohmi, T. Tsuneda, M. Kawai, and M. Isono, “Methods for computation of flow-driven string dynamics in a pump and residence time”, *Mathematical Models and Methods in Applied Sciences*, **29** (2019) 839–870, doi:10.1142/S021820251941001X.
- [50] Y. Bazilevs, K. Takizawa, T.E. Tezduyar, M.-C. Hsu, Y. Otaguro, H. Mochizuki, and M.C.H. Wu, “ALE and space–time variational multiscale isogeometric analysis of wind turbines and turbomachinery”, in A. Grama and A. Sameh, editors, *Parallel Algorithms in Computational Science and Engineering*, Modeling and Simulation in Science, Engineering and Technology, 195–233, Springer, 2020, ISBN 978-3-030-43735-0, doi:10.1007/978-3-030-43736-7.7.
- [51] Y. Bazilevs, K. Takizawa, T.E. Tezduyar, M.-C. Hsu, Y. Otaguro, H. Mochizuki, and M.C.H. Wu, “Wind turbine and turbomachinery computational analysis with the ALE and space–time variational multiscale methods and isogeometric discretization”, *Journal of Advanced Engineering and Computation*, **4** (2020) 1–32, doi:10.25073/jaec.202041.278.
- [52] K. Takizawa, T.E. Tezduyar, and T. Kuraishi, “Multiscale ST methods for thermo-fluid analysis of a ground vehicle and its tires”, *Mathematical Models and Methods in Applied Sciences*, **25** (2015) 2227–2255, doi:10.1142/S0218202515400072.
- [53] K. Takizawa, T.E. Tezduyar, T. Kuraishi, S. Tabata, and H. Takagi, “Computational thermo-fluid analysis of a disk brake”, *Computational Mechanics*, **57** (2016) 965–977, doi:10.1007/s00466-016-1272-4.
- [54] T. Kuraishi, K. Takizawa, and T.E. Tezduyar, “Space–time computational analysis of tire aerodynamics with actual geometry, road contact, tire deformation,

- road roughness and fluid film”, *Computational Mechanics*, **64** (2019) 1699–1718, doi:10.1007/s00466-019-01746-8.
- [55] K. Takizawa, T.E. Tezduyar, A. Buscher, and S. Asada, “Space–time interface-tracking with topology change (ST-TC)”, *Computational Mechanics*, **54** (2014) 955–971, doi:10.1007/s00466-013-0935-7.
- [56] K. Takizawa, T.E. Tezduyar, A. Buscher, and S. Asada, “Space–time fluid mechanics computation of heart valve models”, *Computational Mechanics*, **54** (2014) 973–986, doi:10.1007/s00466-014-1046-9.
- [57] K. Takizawa, T.E. Tezduyar, T. Terahara, and T. Sasaki, “Heart valve flow computation with the integrated Space–Time VMS, Slip Interface, Topology Change and Isogeometric Discretization methods”, *Computers & Fluids*, **158** (2017) 176–188, doi:10.1016/j.compfluid.2016.11.012.
- [58] T. Terahara, K. Takizawa, T.E. Tezduyar, A. Tsushima, and K. Shiozaki, “Ventricle-valve-aorta flow analysis with the Space–Time Isogeometric Discretization and Topology Change”, *Computational Mechanics*, **65** (2020) 1343–1363, doi:10.1007/s00466-020-01822-4.
- [59] T. Terahara, K. Takizawa, T.E. Tezduyar, Y. Bazilevs, and M.-C. Hsu, “Heart valve isogeometric sequentially-coupled FSI analysis with the space–time topology change method”, *Computational Mechanics*, **65** (2020) 1167–1187, doi:10.1007/s00466-019-01813-0.
- [60] K. Takizawa, M. Fritze, D. Montes, T. Spielman, and T.E. Tezduyar, “Fluid–structure interaction modeling of ringsail parachutes with disreefing and modified geometric porosity”, *Computational Mechanics*, **50** (2012) 835–854, doi:10.1007/s00466-012-0761-3.

- [61] K. Takizawa, B. Henicke, A. Puntel, N. Kostov, and T.E. Tezduyar, “Computer modeling techniques for flapping-wing aerodynamics of a locust”, *Computers & Fluids*, **85** (2013) 125–134, doi:10.1016/j.compfluid.2012.11.008.
- [62] K. Takizawa, D. Montes, M. Fritze, S. McIntyre, J. Boben, and T.E. Tezduyar, “Methods for FSI modeling of spacecraft parachute dynamics and cover separation”, *Mathematical Models and Methods in Applied Sciences*, **23** (2013) 307–338, doi:10.1142/S0218202513400058.
- [63] K. Takizawa, T.E. Tezduyar, J. Boben, N. Kostov, C. Boswell, and A. Buscher, “Fluid–structure interaction modeling of clusters of spacecraft parachutes with modified geometric porosity”, *Computational Mechanics*, **52** (2013) 1351–1364, doi:10.1007/s00466-013-0880-5.
- [64] K. Takizawa, T.E. Tezduyar, C. Boswell, R. Kolesar, and K. Montel, “FSI modeling of the reefed stages and disreefing of the Orion spacecraft parachutes”, *Computational Mechanics*, **54** (2014) 1203–1220, doi:10.1007/s00466-014-1052-y.
- [65] K. Takizawa, T.E. Tezduyar, R. Kolesar, C. Boswell, T. Kanai, and K. Montel, “Multiscale methods for gore curvature calculations from FSI modeling of spacecraft parachutes”, *Computational Mechanics*, **54** (2014) 1461–1476, doi:10.1007/s00466-014-1069-2.
- [66] K. Takizawa, T.E. Tezduyar, C. Boswell, Y. Tsutsui, and K. Montel, “Special methods for aerodynamic-moment calculations from parachute FSI modeling”, *Computational Mechanics*, **55** (2015) 1059–1069, doi:10.1007/s00466-014-1074-5.
- [67] K. Takizawa, T.E. Tezduyar, and R. Kolesar, “FSI modeling of the Orion spacecraft drogue parachutes”, *Computational Mechanics*, **55** (2015) 1167–1179,

doi:10.1007/s00466-014-1108-z.

- [68] K. Takizawa, T.E. Tezduyar, and T. Kanai, “Porosity models and computational methods for compressible-flow aerodynamics of parachutes with geometric porosity”, *Mathematical Models and Methods in Applied Sciences*, **27** (2017) 771–806, doi:10.1142/S0218202517500166.
- [69] T. Kanai, K. Takizawa, T.E. Tezduyar, T. Tanaka, and A. Hartmann, “Compressible-flow geometric-porosity modeling and spacecraft parachute computation with isogeometric discretization”, *Computational Mechanics*, **63** (2019) 301–321, doi:10.1007/s00466-018-1595-4.
- [70] T. Meakhail and S.O. Park, “A study of impeller-diffuser-volute interaction in a centrifugal fan”, *Journal of Turbomachinery*, **127** (2005) 84–90.
- [71] M.H. Shojaeefard, M. Tahani, M.B. Ehghaghi, M.A. Fallahian, and M. Beglari, “Numerical study of the effects of some geometric characteristics of a centrifugal pump impeller that pumps a viscous fluid”, *Computers & Fluids*, **60** (2012) 61–70.
- [72] T.J.R. Hughes and G. Sangalli, “Variational multiscale analysis: the fine-scale Green’s function, projection, optimization, localization, and stabilized methods”, *SIAM Journal of Numerical Analysis*, **45** (2007) 539–557.
- [73] T.J.R. Hughes and A.A. Oberai, “Calculation of shear stress in Fourier–Galerkin formulations of turbulent channel flows: projection, the Dirichlet filter and conservation”, *Journal of Computational Physics*, **188** (2003) 281–295.
- [74] K. Takizawa, T.E. Tezduyar, and Y. Otoguro, “Stabilization and discontinuity-capturing parameters for space–time flow computations with finite element and isogeometric discretizations”, *Computational Mechanics*, **62** (2018) 1169–1186, doi:10.1007/s00466-018-1557-x.

- [75] Y. Ootoguro, K. Takizawa, and T.E. Tezduyar, “Element length calculation in B-spline meshes for complex geometries”, *Computational Mechanics*, **65** (2020) 1085–1103, doi:10.1007/s00466-019-01809-w.
- [76] Y. Bazilevs and T.J.R. Hughes, “NURBS-based isogeometric analysis for the computation of flows about rotating components”, *Computational Mechanics*, **43** (2008) 143–150.
- [77] M.-C. Hsu and Y. Bazilevs, “Fluid–structure interaction modeling of wind turbines: simulating the full machine”, *Computational Mechanics*, **50** (2012) 821–833.
- [78] K. Takizawa, T.E. Tezduyar, and T. Terahara, “Ram-air parachute structural and fluid mechanics computations with the space–time isogeometric analysis (ST-IGA)”, *Computers & Fluids*, **141** (2016) 191–200, doi:10.1016/j.compfluid.2016.05.027.
- [79] J.A. Evans and T.J.R. Hughes, “Isogeometric divergence-conforming b-splines for the unsteady navier–stokes equations”, *Journal of Computational Physics*, **241** (2013) 141–167.
- [80] Y. Bazilevs and I. Akkerman, “Large eddy simulation of turbulent Taylor–Couette flow using isogeometric analysis and the residual–based variational multiscale method”, *Journal of Computational Physics*, **229** (2010) 3402–3414.
- [81] M.F.P. ten Eikelder and I. Akkerman, “Correct energy evolution of stabilized formulations: The relation between VMS, SUPG and GLS via dynamic orthogonal small-scales and isogeometric analysis. II: The incompressible Navier–Stokes equations”, *Computer Methods in Applied Mechanics and Engineering*, **340** (2018) 1135–1154, doi:10.1016/j.cma.2018.02.030.

- [82] S.C. Cheah, H. Lacovides, D.C. Jackson, H. Ji, and B.E. Launder, “LDA investigation of the flow development through rotating U-ducts”, *Proceedings of the ASME Turbo Expo*, **5** (1994).
- [83] R.H. Sabersky and A.J. Acosta, *Fluid flow, a first course in fluid mechanics*. Collier-Macmillan, 1964.
- [84] S. Pirozzoli, D. Modesti, P. Orlandi, and F. Grasso, “Turbulence and secondary motions in square duct flow”, *Journal of Fluid Mechanics*, **840** (2018) 631–655, doi:10.1017/jfm.2018.66.
- [85] D. Modesti, S. Pirozzoli, P. Orlandi, and F. Grasso, “Analysis of secondary motions in square duct flow”, *IOP Conference Series: Journal of Physics*, **1001** (2018) 012009, doi:10.1088/1742-6596/1001/1/012009.
- [86] C.D. Andereck, S.S. Liu, and H.L. Swinney, “Flow regimes in a circular Couette system with independently rotating cylinders”, *Journal of Fluid Mechanics*, **164** (1986) 155–183.
- [87] K. Takizawa, Y. Ueda, and T.E. Tezduyar, “A node-numbering-invariant directional length scale for simplex elements”, *Mathematical Models and Methods in Applied Sciences*, **29** (2019) 2719–2753, doi:10.1142/S0218202519500581.

List of research achievements for application of Doctor of Engineering, Waseda University

Full Name : AYDINBAKAR LEVENT

seal or signature

Date Submitted (yyyy/mm/dd) :

2021/03/04

種類別 (By Type)	題名、 発表・発行掲載誌名、 発表・発行年月、 連名者 (申請者含む) (theme, journal name, date & year of publication, name of authors inc. yourself)
Journal Articles (peer-Reviewed)	<p>O 1. Levent Avdinbakar, Kenji Takizawa, Tayfun E. Tezduyar, Daisaku Matsuda, “U-duct turbulent-flow computation with the ST-VMS method and isogeometric discretization”, <i>Computational Mechanics</i>, published online, 2021.</p> <p>O 2. Levent Avdinbakar, Kenji Takizawa, Tayfun E. Tezduyar, Takashi Kuraishi, “Space-time VMS isogeometric analysis of the Taylor–Couette flow”, <i>Computational Mechanics</i>, to appear, 2021.</p>
International Lectures	<p>O Levent Avdinbakar, Kenji Takizawa, Tayfun E. Tezduyar, Daisaku Matsuda, “U-Duct Turbulent-Flow Computation with the ST-VMS Method and Isogeometric Discretization” in <i>Proceedings of the Asian Pacific Congress on Computational Mechanics (APCOM) 2019</i>, Taipei, Taiwan, 2019.</p>
Technical Report	<p>O Levent Avdinbakar, Kenji Takizawa, Tayfun E. Tezduyar, “Double-Suction Centrifugal Pump, Flow and Performance Analysis” <i>Technical Report, Waseda University</i>, 2018.</p>